Axion quasiparticles for axion dark matter detection

Schütte-Engel, Jan; Marsh, David J.E.; Millar, Alexander J.; Sekine, Akihiko; Chadha-Day, Francesca; Hoof, Sebastian; Ali, Mazhar N.; Fong, Kin Chung; Hardy, Edward; More Authors

DOI
10.1088/1475-7516/2021/08/066

Publication date
2021

Document Version
Final published version

Published in
Journal of Cosmology and Astroparticle Physics

PAPER

Axion quasiparticles for axion dark matter detection

Journal of Cosmology and Astroparticle Physics
An IOP and SISSA journal

Axion quasiparticles for axion dark matter detection

Jan Schütte-Engel,[a,b,c] **David J.E. Marsh,**[d] **Alexander J. Millar,**[e,f] **Akihiko Sekine,**[g] **Francesca Chadha-Day,**[h] **Sebastian Hoof,**[d] **Mazhar N. Ali,**[i,j] **Kin Chung Fong,**[k] **Edward Hardy**[l] **and Libor Šmejkal**[m,n]

[a]Department of Physics, University of Illinois at Urbana-Champaign, Urbana, IL 61801, U.S.A.
[b]Illinois Center for Advanced Studies of the Universe, University of Illinois at Urbana-Champaign, Urbana, IL 61801, U.S.A.
[c]Hamburg University, 22761 Hamburg, Germany
[d]Institut für Astrophysik, Georg-August-Universität Göttingen, Friedrich-Hund-Platz 1, 37077 Göttingen, Germany
[e]The Oskar Klein Centre for Cosmoparticle Physics, Department of Physics, Stockholm University, AlbaNova, 10691 Stockholm, Sweden
[f]Nordita, KTH Royal Institute of Technology and Stockholm University, Roslagstullsbacken 23, 10691 Stockholm, Sweden
[g]RIKEN Center for Emergent Matter Science, Wako, Saitama 351-0198, Japan
[h]Department of Physics, University of Durham, South Rd, Durham DH1 3LE, United Kingdom
[i]Max Planck Institute of Microstructure Physics, Weinberg 2, 06120 Halle, Germany
[j]Kavli Institute of Nanoscience, Delft University of Technology, Delft, Netherlands
[k]Raytheon BBN Technologies, Quantum Engineering and Computing, Cambridge, Massachusetts 02138, U.S.A.
[l]Mathematical Sciences, The University of Liverpool, Liverpool, L69 7ZL, United Kingdom
[m]Institut für Physik, Johannes Gutenberg Universität Mainz, 55128 Mainz, Germany
[n]Institute of Physics, Czech Academy of Sciences, Cukrovarnická 10, 162 00, Praha 6, Czech Republic
E-mail: jans@illinois.edu, david.j.marsh@kcl.ac.uk, alexander.millar@fysik.su.se, akihiko.sekine1@gmail.com, francesca.chadha-day@durham.ac.uk, hoof@uni-goettingen.de, maz@berkeley.edu, fongkc@gmail.com, edward.hardy@liverpool.ac.uk, lsmejkal@uni-mainz.de

Received March 12, 2021
Accepted July 8, 2021
Published August 31, 2021

 https://doi.org/10.1088/1475-7516/2021/08/066

JCAP08(2021)066

Abstract. It has been suggested that certain antiferromagnetic topological insulators contain axion quasiparticles (AQs), and that such materials could be used to detect axion dark matter (DM). The AQ is a longitudinal antiferromagnetic spin fluctuation coupled to the electromagnetic Chern-Simons term, which, in the presence of an applied magnetic field, leads to mass mixing between the AQ and the electric field. The electromagnetic boundary conditions and transmission and reflection coefficients are computed. A model for including losses into this system is presented, and the resulting linewidth is computed. It is shown how transmission spectroscopy can be used to measure the resonant frequencies and damping coefficients of the material, and demonstrate conclusively the existence of the AQ. The dispersion relation and boundary conditions permit resonant conversion of axion DM into THz photons in a material volume that is independent of the resonant frequency, which is tuneable via an applied magnetic field. A parameter study for axion DM detection is performed, computing boost amplitudes and bandwidths using realistic material properties including loss. The proposal could allow for detection of axion DM in the mass range between 1 and 10 meV using current and near future technology.

Keywords: axions, dark matter detectors, dark matter theory, dark matter experiments

ArXiv ePrint: 2102.05366

JCAP08(2021)066

Contents

JCAP08(2021)066

JCAP08(2021)066

1 Introduction

The quantum chromodynamics (QCD) axion [1–3] solves the charge-parity ($\mathcal{CP}$) problem of the strong nuclear force [4–6], and is a plausible candidate [7–9] to compose the dark matter (DM) in the cosmos [10]. The axion mass is bounded from above [11–13] and below [14, 15] by astrophysical constraints (for reviews, see refs. [16–19], and appendix B), placing it in the range

$$1\,\mathrm{peV} \lesssim m_a \lesssim 20\,\mathrm{meV}\,. \tag{1.1}$$

The local DM density is known from stellar motions in the Milky Way [20]. Assuming axions comprise all the (local) DM, the axion number density is given by $n_a = \rho_{\mathrm{loc}}/m_a$. Due to the very small axion mass, the number density is very large and axions can be modelled as a coherent classical field, ϕ. The field value is:

$$\phi = \Phi\cos(m_a t)\,, \tag{1.2}$$

where Φ is Rayleigh-distributed [21, 22] with mean $\sqrt{2\rho_{\mathrm{loc}}}/m_a$ and linewidth $\Delta\omega/\omega \sim 10^{-6}$ given by the Maxwell-Boltzmann distribution of axion velocities around the local galactic circular speed, $v_{\mathrm{loc}} \approx 200\,\mathrm{km/s}$ (see e.g. refs. [21, 23]).

Axions couple to electromagnetism via the interaction $\mathcal{L} = g_{a\gamma}\phi\boldsymbol{E}\cdot\boldsymbol{B}$. Thus, in the presence of an applied magnetic field, $\boldsymbol{B}_0$, the DM axion field in eq. (1.2) acts as a source for the electric field, $\boldsymbol{E}$. This is the inverse Primakoff process for axions, and leads to axion-photon conversion in a magnetic field. The rate of axion-photon conversion depends on the unknown value of the coupling $g_{a\gamma}$ and happens at an unknown frequency $\omega = m_a \pm \Delta\omega$. For the QCD axion (as opposed to a generic "axion like particle" [16]) the mass and coupling are linearly related, $g_{a\gamma} \propto m_a$, although different models for the Peccei-Quinn [1] charges of fundamental fermions predict different values for the constant of proportionality. The two historical reference models of Kim-Shifman-Vainshtein-Zhakarov (KSVZ) [24, 25] and Dine-Fischler-Srednicki-Zhitnitsky (DFSZ) [26, 27] span a narrow range, while more recent generalisations with non-minimal particle content allow for more variation [19, 28, 29].

The axion-photon coupling $g_{a\gamma}$ is constrained by a large number of null-results from experimental searches and astrophysical considerations [20]. For experimentally allowed values of $(m_a, g_{a\gamma})$, and accessible magnetic field strengths, the photon production rate in vacuum is unobservably small. The power can be increased in two basic ways. If the conversion happens along the surface of a magnetized mirror, then the produced photons can be focused onto a detector [30]. This approach is broadband, and does not depend on the axion mass. Reaching sensitivity to the QCD axion requires very large mirrors, very sensitive detectors,

and control over environmental noise. Alternatively, the signal can be resonantly or coherently enhanced (e.g. refs. [31–40]). These approaches are narrow band, and require tuning to the unknown DM axion frequency.

Depending on the model of early Universe cosmology, and the evolution of the axion field at high temperatures $T \gg 1\,\mathrm{MeV}$, the entire allowed mass range eq. (1.1) can plausibly explain the observed DM abundance. The mass range near 1 meV (corresponding to frequencies in the low THz) is favoured in some models of axion cosmology (see appendix B), but is challenging experimentally due to the lack of large volume, tuneable THz resonators, and efficient, low-noise, large bandwidth THz detectors.

In ref. [41] (Paper I) we proposed an experimental scheme to detect axion DM using axion-quasiparticle (AQ) materials based on topological magnetic insulators (TMIs) [42], a proposal we called "TOORAD" for "TOpolOgical Resonant Axion Detection". Since Li et al. [42] first proposed to realise axion quasiparticles in the antiferromagnetic topological insulator (AF-TI) Fe-doped Bismuth Selenide, $(Bi_{1-x}Fe_x)_2Se_3$, the quest to realise related materials in the lab has picked up incredible pace. A currently favoured candidate $Mn_2Bi_2Te_5$ [43], is, however, yet to be fabricated successfully. AQ materials allow the possibility to explore aspects of axion physics in the laboratory [44]. The AQ resonance hyrbidises with the electric field forming an axion-polariton [42]. The polariton frequency is of order the AF anisotropy field, with typical values $\mathcal{O}(1\,\mathrm{meV})$, and is tuneable with applied static field B [41]. This proposal opens the possibility for large volume THz resonance, easily tuneable with an applied magnetic field, thus overcoming the first hurdle to detection of meV axions. The proposal makes use of the current interest in manufacture of low noise, high efficiency single photon detectors (SPDs) in THz [45]. The development of such detectors has benefits for sub mm astronomy and cosmology, as well as application to other DM direct detection experiments [30].

The present paper expands on the ideas outlined in Paper I with more in depth modelling and calculations. A guide to the results is given below.

Axion quasiparticle materials

We begin with a detailed treatment of the materials science, and outline a scheme to prove the existence of AQs in TMIs, and measure their parameters.

- We introduce the basic model for the equations coupling the electric field and the AQ. There are two parameters that determine the model: the AQ mass, m_Θ, and the decay constant, f_Θ, as summarised in section 2.1.

- Next in section 2.2, we clarify the microscopic model for AQs in TMIs. We begin with the symmetry criteria, followed by a microscopic model based on the Dirac Hamiltonian. The AQ is the longitudinal fluctuataion of the antiferromagnetic order parameter in the Hubbard model. The appendix summarises the related phenomenon of antiferromagnetic resonance and transverse magnons in the effective field theory of the Heisenberg model.

- Both m_Θ and f_Θ can be estimated from known material properties. We consider $(Bi_{1-x}Fe_x)_2Se_3$, the candidate material from Paper I and ref. [42], and also the more recent candidate material $Mn_2Bi_2Te_5$ [43]. The results of this study are given in tables 4 and 5.

JCAP08(2021)066

- We next consider sources of loss. The largest sources of loss are identified to be conductive losses to the electric field, and crystal and magnetic domain induced line broadening for the AQ. The loss model is summarised in table 6.
- Using the model thus developed, we present a computation of the transmission spectrum of an AQ material. The spectrum shows two peaks due to the mixing of the electric field and the AQ, the locations of which can be used to measure the parameters m_Θ and f_Θ. The width of the resonances provides a measurement of the loss parameters on resonance, which cannot otherwise be identified from existing measurements. Such a measurement can be performed using THz time domain spectroscopy [46]. The procedure is shown schematically in figure 6

Axion dark matter detection

- Axion DM acts as a source to the AQ model developed in the previous sections. Axion-photon conversion in a magnetic field sources photons, which hybridize with the AQ forming polaritons, and thus acquire an effective mass. It is shown that this model can be treated in the same way as a dielectric haloscope [47]. The resonance in the polariton spectrum leads to an effective refractive index $n < 1$, and an enhancement of the axion-induced electric field, see figure 16.
- We compute the power boost amplitude, $\beta(\omega)$, for a range of plausible values for the model parameters, losses, and material thickness. See, for example, figure 17.
- The power enhancement is driven by the material thickness, d, which should *exceed* the wavelength of emitted photons. When losses are included, we identify a maximum thickness above which the power enhancement decreases due to the finite skin-depth. See figure 19.
- We perform forecasts for the limits on axion DM parameter space, $(m_a, g_{a\gamma})$, that can be obtained for a range of plausible material and THz detector parameters. We identify pessimistic and optimistic possibilities for the discovery reach, summarised in figure 23.

We use units $\hbar = c = k_B = 1$ throughout most of the text, in combination with SI where appropriate.

2 Axion quasiparticle materials

2.1 General remarks

Axion quasiparticles (AQs) are defined, for our purposes, as a degree of freedom, denoted by $\delta\Theta$, coupled to the electromagnetic Chern-Simons term:

$$S_{\rm topo} = \frac{\alpha}{\pi}\int \mathrm{d}^4x\, (\delta\Theta + \Theta^0)\, \boldsymbol{E}\cdot\boldsymbol{B}\,, \tag{2.1}$$

where Θ^0 is the constant electromagnetic Chern-Simons term, equal to zero in ordinary insulators and π in topological insulators (TIs). In these materials, surface currents are accounted for by inclusion of a non-zero value for Θ^0 (the topological magneto-electric effect due to the Hall conductivity [48, 49]). In the presence of a dynamical AQ field, $\delta\Theta$, the static vacuum value Θ^0 is allowed to take on a continuum of values between 0 and π. The total axion field is denoted by $\Theta = \delta\Theta + \Theta^0$. We review these concepts further below, for a detailed presentation see ref. [50].

JCAP08(2021)066

The dynamics of the AQs are described by [42, 51]

$$S_\Theta = \frac{f_\Theta^2}{2}\int d^4x \left[(\partial_t\delta\Theta)^2 - (v_i\partial_i\delta\Theta)^2 - m_\Theta^2\delta\Theta^2\right], \tag{2.2}$$

where f_Θ, v_i and m_Θ are the stiffness, velocity and mass of the AQ. The velocities v_i are of the order of the spin wave speed in typical antiferromagnets, $v_s \sim 10^{-4}c$, see for example ref. [52]. In the coupled equations of motion for the electric field and the AQ (see section 3.2), f_Θ enters in the combination[1]

$$b = \frac{\alpha}{\pi\sqrt{2}}\frac{B_\mathrm{e}}{\sqrt{\epsilon}f_\Theta} = 1.6\,\mathrm{meV}\left(\frac{25}{\epsilon_1}\right)^{1/2}\left(\frac{B_\mathrm{e}}{2\,\mathrm{T}}\right)\left(\frac{70\,\mathrm{eV}}{f_\Theta}\right). \tag{2.3}$$

In addition to the action for the AQ we consider electromagnetic fields governed by Maxwell's equations in media, which depend on the complex valued dielectric function, $\tilde{\epsilon} = \epsilon_1 + i\epsilon_2 = \epsilon_1 + i\sigma/\omega$ (where σ is the conductivity), and magnetic susceptibility, χ_m. Where there is no room for confusion we use $\epsilon_1 = \epsilon$ in some of the following. The phenomenological model also requires the specification of a loss matrix, $\mathbf{\Gamma}$.

2.2 Realisation in Dirac quasiparticle antiferromagnets

The idea to realise axion electrodynamics in solids was originally developed by Wilczek [44] who, however, could not identify a magnetic solid that breaks parity and time-reversal while preserving its combination: as we will see, necessary conditions for AQs. Recent developments in nonmagnetic and magnetic electronic topological phases of matter, and study of the topological magnetoelectric effect associated with the Chern-Simons term in magnetoelectrics [53, 54] have led to the identification of several routes to realise axion electrodynamics in energy bands of magnetic topological insulators and Dirac quasiparticle antiferromagnets. The electronic, magnetic, topological energy bands can couple to spin fluctuations, and thus generate a dynamical axion phase on the electromagnetic Chern-Simons term.

In this section we discuss the Dirac quasiparticle model of AQs in electronic energy bands. We compare the symmetry criteria for static and dynamical axion topological antiferromagnets, and discuss the most prominent material candidates.

2.2.1 Symmetry criteria for static and dynamical magnetic axion insulators

The topological Θ term is called also an *axion angle* as it can take any value between 0 and 2π. The operations of charge conjugation $\mathcal{C}$, parity $\mathcal{P}$ (known as inversion symmetry in condensed matter, a terminology we adopt throughout this section to distinguish it from other types of parity operation in solids), and time-reversal $\mathcal{T}$ are the discrete symmetries constraining the values of Θ, and which define the properties of fundamental forces in nature via the $\mathcal{CPT}$ theorem. $\mathcal{CP}$ breaking means that the physical laws are not invariant under combination of interchanging particle with its antiparticle with inverting the spatial coordinates. If $\Theta \neq 0, \pi$, then $\mathcal{CP}$ is violated. The combined $\mathcal{CPT}$ symmetry is believed to be preserved (i.e. the so called $\mathcal{CPT}$ theorem) and thus the violation of $\mathcal{CP}$ implies the violation of $\mathcal{T}$ symmetry, i.e. the reversal of the time coordinate, and thus particle motion. Realisation of $\mathcal{CP}$-broken theory and axion electrodynamics with non-quantized axion angle can be achieved in materials with broken $\mathcal{T}$ symmetry [44, 55, 56]. In materials, magnetic ordering can break the $\mathcal{T}$ symmetry. In this section we will discuss the symmetries of magnetic axion insulators which exhibit

[1] Note that we use the Lorentz-Heaviside convention, where $1\,\mathrm{T} \approx 195\,\mathrm{eV}^2$.

JCAP08(2021)066

nonzero pseudoscalar axion quasiparticle Θ (we use capital letter to label the solid state quasiparticle axion to distinguish it from the DM axion).

The nonzero axion response can be find in subgroup of conventional and topological magnetoelectric materials. The conventional magneto-electric polarizability tensor is defined as [48, 57]:

$$\alpha_{ij} = (\partial P_i/\partial B_j)_{\mathbf{E}} = (\partial M_j/\partial E_i)_{\mathbf{B}}\,. \tag{2.4}$$

Here P_i, B_j, M_j, and E_i are electric polarisation, magnetic field, magnetization, and electric field. The magnetoelectric polarizability tensor can be decomposed as [48]:

$$\alpha_{ij} = \tilde{\alpha}_{ij} + \frac{\Theta e^2}{2\pi h}\delta_{ij}, \tag{2.5}$$

where the first term is the non-diagonal part of the tensor arising from spin, orbital and ionic contribution [58]. The second term is the diagonal pseudoscalar part of the coupling related to the axion angle Θ.

We will now review symmetry criteria for nonzero axion quasiparticle Θ. In solid state potentials, discrete symmetries impose severe constraint on the existence and form of the topological axion angle [59], and provide robust insight into the topological characterisation of the energy bands [60–63]. The topological classification assigns two insulators into the same category as long as it is possible to connect the two corresponding Hamiltonians by a continuous deformation without closing an energy gap and while preserving all symmetries [53, 54].

Three symmetry based strategies attracted great interest in recent decades. First, solid state quantum field theory considers parity, chiral, and particle-hole symmetries, which are relevant for rather strongly correlated states of matter such as superconductors and lead to abstract multidimensional classification [64]. Second, more numerically feasible symmetry analysis of Wannnier band structure. The Wannier band structure refers to mixes of real and momentum space band structure, with hybrid Wannier charge centres, which encodes the topological character of given states [56, 59, 65]. The formulation is particularly useful for first-principle calculations of the axion angle. Third, we can use space group or magnetic space group symmetries to derive symmetry indicators of single particle energy bands [59, 62, 63, 66, 67].

The $\boldsymbol{E}.\boldsymbol{B}$ term is odd under time-reversal symmetry, inversion symmetry and any improper rotations, e.g. mirror symmetries [59, 61]. If the crystal has such a symmetry:

$$\Theta = -\Theta. \tag{2.6}$$

The symmetry constraint would force any periodic function to vanish. However, Θ is periodic angle defined only modulo 2π and thus these symmetries enforce only

$$\Theta = 0, \text{ or } \pi. \tag{2.7}$$

When none of these symmetries is present Θ can be still non-quantized.

Based on the *magnetic* symmetry classification, we can distinguish four classes of pseudoscalar magneto-electric axion response materials shown in figure 1. First two classes are conventional magnetoelectrics [68] and dynamical axion insulators [42] with nonzero pseudoscalar part of the magnetoelectric polarisability tensor (and combined $\mathcal{PT}$ symmetry [66, 67] such as $Mn_2Bi_2Te_5$ [43]). Second two classes are the topological insulators and axion insulators with quantized magnetoelectric response such as doped Bi_2Se_3 or $MnBi_2Te_4$ [42, 50, 53, 54, 57].

JCAP08(2021)066

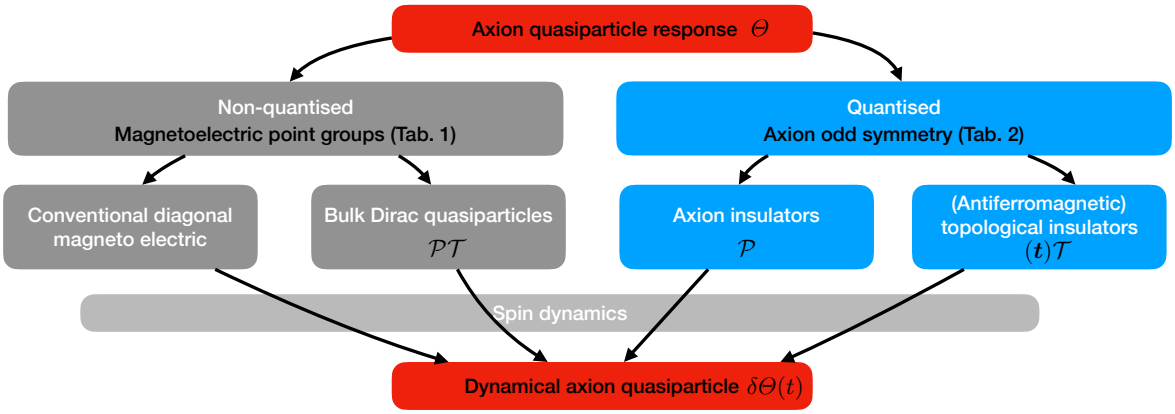

Figure 1. Flowchart of generating dynamical axion quasiparticles with four building bock systems.

Components	FM MPG	AF MPG	Material
$\begin{pmatrix} \alpha_{xx} & \alpha_{yy} & \alpha_{zz} \end{pmatrix}$	1 2 m' $m'm'2$	$(\bar{1}')$ $(\mathbf{2}/\boldsymbol{m}')$ 222 $(m'm'm')$	$(Fe,Bi)_2Se_3$
$\begin{pmatrix} \alpha_{xx} & \alpha_{xx} & \alpha_{zz} \end{pmatrix}$	3 4 6 $3m'$ $4m'm'$ $6m'm'$	$(\bar{3}')$ $\bar{4}'$ $4/m'$ $\bar{6}'$ $6/m'$ 32 $(\bar{\mathbf{3}}'\boldsymbol{m}')$ 422 $\bar{4}'2m'$ $(4/m'm'm')$ 622 $\bar{6}'m'2$ $(6/m'm'm')$	Cr_2O_3[69]
$\begin{pmatrix} \alpha_{xx} & -\alpha_{xx} & 0 \end{pmatrix}$	$\bar{4}$, $\bar{4}2'm'$	$4'$ $(4'/m')$, $4'22'$ $4'mm'$ $\bar{4}m2$ $(4'/m'mm')$	
$\begin{pmatrix} \alpha_{xx} & \alpha_{xx} & \alpha_{xx} \end{pmatrix}$		23, $(m'\bar{3}')$, 432, $\bar{4}'3m'$ $(m'\bar{3}'m')$	

Table 1. Table of antiferromagnetic and ferromagnetic nonquantized axion magnetoelectric symmetry groups and candidate material. In the first column we show only the diagonal part of magnetoelectric polarizability tensor α_{ij}. The symbols $\bar{1}$ and $1'$ mark spatial inversion and time-reversal symmetry, respectively. FM and AF MPG refers to ferromagnetic and antiferromagnetic magnetic point group [71].

The nonquantized value of Θ can be find in subset of 58 magnetic point groups allowing for general magnetoelectric response. We summarise in table 1 only the 40 mangetic point groups which allow for the nonzero diagonal magnetoelectric response elements [69, 70]. We also list whether the material has allowed ferromagnetism (FM, 12 magnetic point groups) or is enforced by the point group symmetry to be antiferromagnetic (AF, 28 point groups) [71] together with several material examples. We see that the magnetoelectric response can be anisotropic what was confirmed experimentally [72]. Note that the third row of the table 1 gives zero trace. This analysis excludes from pseudoscalar magnetoelectric coupling materials which do exhibit only traceless magnetoelectric coupling. When the system breaks $\mathcal{P}$ and $\mathcal{T}$ but preserves its combination, it can host also bulk Dirac quasiparticles [66]. We mark the $\mathcal{PT}$ symmetric magnetoelectric pseudoscalar point groups by brackets in table 1.

In topological insulators, such as Bi_2Se_3 (the nonmagnetic phase of crystal shown in figure 2(a)) and Bi_2Te_3, the presence of $\mathcal{T}$ symmetry in combination with nontriivial band inversion ensures the axion angle Θ to be π [73], requires zero surface Hall conductivity, and the topological magneto-electric effect [74]. The topological magneto-electric effect in topological insulators refers to a quantized magneto-electric response, and has been observed also

JCAP08(2021)066

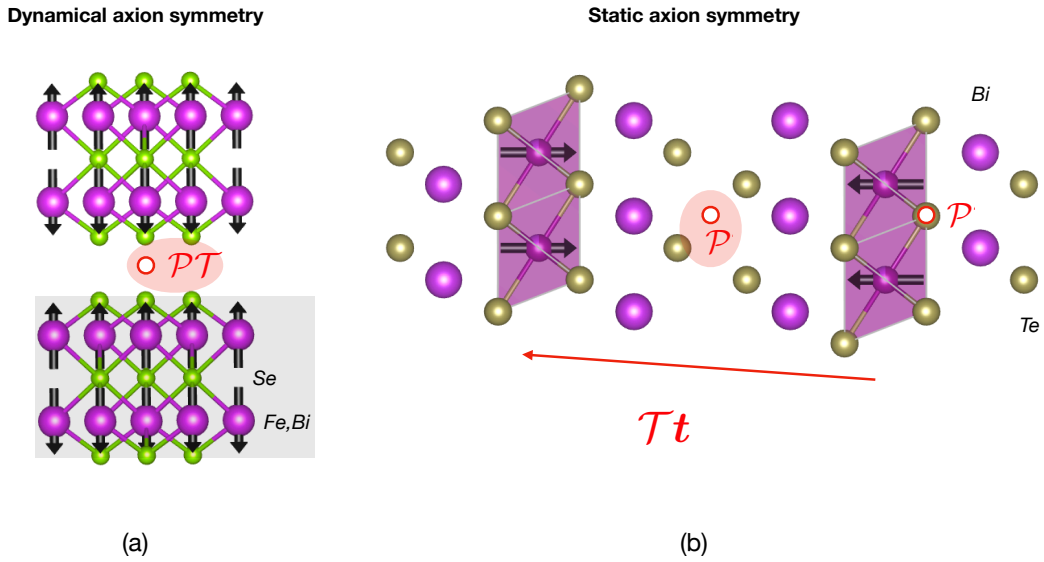

Figure 2. (a) Crystal structure of topological insulator Bi_2Se_3 consist from quintuple layers forming rhombohedral unit cell. Antiferromagnetism of the magnetically doped $(Fe,Bi)_2Se_3$ breaks spatial inversion $\mathcal{P}$ and time-reversal $\mathcal{T}$ symmetry, but preserve combined $\mathcal{PT}$ symmetry. (b) Crystal structure of intrinsic antiferromagnetic axion insulator $MnBi_2Te_4$. The quantized value of axion angle is protected by the inversion symmetry $\mathcal{P}$ (we maek two inversion symmetry points in the lattice). The system exhibits also partial unit cell translation $\boldsymbol{t}$ combined with time-reversal symmetry $\mathcal{T}$.

by magneto-optical measurements [73]. In fact, the quantization of Θ in non-magnetic topological insulators can be taken as defining property of topological insulators [74]. Recently, also antiferromagnetic topological insulator [75] was found in $MnBi_2Te_4$ [76]. Antiferromagnetic topological insulator state is protected by time-reversal symmetry coupled with partial unit cell translation $\boldsymbol{t}$ as we show in figure 2(b).

The *static* axion insulators are magnetic topological insulators, such as $MnBi_2Te_4$ [77, 78], which break $\mathcal{T}$ symmetry via the presence of a magnetic ion (in this case, Mn). However, they exhibit axion response with $\Theta = \pi$, protected by the presence of axion odd symmetries such as inversions, see inversion centre in figure 2(b), or crystalline symmetries. The axion-odd symmetries are the symmetries which reverse the sign of Θ and support the so called $\mathbb{Z}_2$ classification [60, 61, 79]. Among the additional axion-odd symmetries are improper rotations, and antiunitary proper rotations (for instance rotation combined with time-reversal). In the table 2, we list axion angle quantizing symmetry operations, g. We decompose the symmetry operation $g = g_{\parallel} \circ g_{\perp}$ into the parts $g_{\parallel}$ and $g_{\perp}$ which are parallel and perpendicular (in the surface plane) to the given surface normal $\hat{z}$ [59]. We remark that we list the point group operation, but in general we need to pay attention to the nonsymmoprhic partial translations of the group, for details see [59].

Finally, the *dynamical* axion insulator allows for nonquantized dynamical axion angle. The dynamics of the axion angle was suggested to be induced by chiral magnetic effect, antiferromangetic resonance [43], longitudinal spin fluctuations [42] in an antiferromagnet or spin fluctuations in paramagnetic state [80]. In figure 2(a), we show an example of lattice with dynamical axion insulator state — Fe-doped $(Bi_{1-x}Fe_x)_2Se_3$ with $\mathcal{PT}$ symmetric crystal. Here, the antiferromagnetism breaks the inversion and time-reversal symmetries of the Bi_2Se_3 crystal. The symmetry breaking is desribed by mass term M_5 which corresponds to the band-

JCAP08(2021)066

g	$g_\parallel$	$g_\perp$
Operations reversing $\hat{\mathbf{z}}$		
$\mathcal{M}_z$	$\mathcal{M}_z$	$\mathcal{E}$
$\mathcal{P}$		$\mathcal{C}_2$
$\mathcal{S}_{3,4,6}$		$\mathcal{C}_{3,4,6}$
$\bar{\mathcal{C}}_2\mathcal{T}$		$\mathcal{M}_d\mathcal{T}$
Operations preserving $\hat{\mathbf{z}}$		
$\mathcal{E}\mathcal{T}$	$\mathcal{E}$	$\mathcal{E}\mathcal{T}$
$\mathcal{C}_{2,3,4,6}\mathcal{T}$		$\mathcal{C}_{2,3,4}\mathcal{T}$
$\mathcal{M}_d$		$\mathcal{M}_d$

Table 2. Axion angle quantizing symmetries. $\mathcal{E}$, $\mathcal{P}$, $\mathcal{M}_z$, $\mathcal{M}_d$, $\mathcal{C}_{2,3,4,6}$, $\mathcal{S}_{3,4,6}$, and $\mathcal{T}$ mark unitary symmmetry operations of identity, inversion, mirror parallel and perpendicular to surface normal $\hat{\boldsymbol{z}}$, rotational axis, improper rotations, and time-reversal, respectively. Overbar marks inversion. Adapted after [59].

gap in surface state. The combined $\mathcal{PT}$ symmetry is in the $(Bi_{1-x}Fe_x)_2Se_3$ crystal preseved and enforces Kramers degenerate bands. This can be seen by acting $\mathcal{PT}$ symmetry on the Bloch state to show that these two states have the same energy and are orthoghonal [66, 67, 81–83]. The presence of $\mathcal{PT}$ allows for antiferromagnetic Dirac quasipaticles [66, 67] with plethora of unconventional and practically useful response such as large anisotropic magnetoresistance [66, 84]. We discuss the material physics requirements for dynamical axion insulator in the section followed by section on minimal effective model of a dynamical axion insulator.

2.2.2 Material candidates

In this section we list requirements for a dynamical axion insulator which is also suitable for dark axion detection [85]. In addition to constraints comming from requiring dynamical axion quasiparticles, we need to ensure strong coupling of the Θ magneto-electric response to the fluctuations of the magnetic order parameter. The concept was originally developed for the longitudinal fluctuations in the Néel order parameter in magnetically doped topological insulators ($(Bi_{1-x}Fe_x)_2Se_3$ in ref. [42]) and recently extended into the instrinsic antiferromagnet $Mn_2Bi_2Te_5$ [43]. This dynamical axion field is quite weak due to the low magnetoelectric coupling and trivial electronic structure in conventional materials such as Cr_2O_3 [86] and $BiFeO_3$ [87] with $\Theta = 10^{-3}$ and 10^{-4}, respectively, see table 3. The dynamical axion effect (i.e. a large Θ response to external perturbations) can be enhanced in the proximity of the topological phase transitions [43]. We now summarise the material criteria for a dynamical axion quasiparticles for detecting dark matter axion:

- Nonzero dynamical axion angle. The material symmetry allows for dynamical axion insulator state and axion spin density wave [42, 43, 80] with mass in the range of meV. This is one of the main advantage of using axion quasiparticles in antiferromagnets for detecting light and weakly interacting DM axions [41].

- Large bulk band-gap [55]. The material is in bulk semicondcuting or insulating with a large bulk band-gap, without disturbing bulk metallic states. In turn its low energy physics is governed solely by the axion coupling.

JCAP08(2021)066

- Topological mass term M_5 should be of order of dynamical axion fluctuation mass m_a to ensure resonance with DM axion [41, 42].

- Large fluctiation in axion angle. This can be achieved close to the magnetic and topological phase transition as $\delta\Theta(\boldsymbol{r}, t) = \delta M_5/g$, and $1/g \sim 1/\mathcal{M}(0)$ [43]. The topological phase transition should be approached from the topological side. Practically, one can tune this mass term by alloying. The alloying can effectively tune the strength of the spin orbit interaction. However, the proximity close to the magnetic transition can compromise narrow linewidth, see next point.

- Trade-off among narrow linewidth and sensitivity. Narrow linewidth of the axion respones where the thermal fluction and scattering are supressed. This imposis tmeperature constraints (i.e. $T \ll T_N$, $T \ll m_5$). In contrast, enhanced response close the mangetic phase transition could enhance sensitivity.

- Robust magnetic ordering with elevated critical (Néel) temperature.

- As we will see in chapter about power output we need large spin-flop fields ($> 1\,\mathrm{T}$) again favouring antiferromagnetic ordering.

- Linear coupling of magnetic fluctuations to generate measurable axion polariton which is used for the detection of the dark matter axion. Li et al. [42] has used linear coupling of the longitudinal spin wave mode. From this perspective, the relatively streightforward generations of dynamical axion by chiral magnetic effect or (anti)ferromagnetic resonance are not suitable. For the conventional transeversal spin waves would produce rahter quadratic coupling. This point is an open problem, however, the antiferromangetic spin density wave states [88] with longitudinal component are also possible candidates at the moment.

- Magnetic and relativistic chemistry of low energy state manifold [55]: 3d states ensuring magnetism and time-reversal symmetry breaking and heavy elements with strong atomic spin-orbit interaction. Low energy states of common topological insulators are often heavy p-states which have low correlations and do not support magnetism.

The last point can be justified by considering limitation of existing axion insulators proposals. 3d and 4d elements do have large electronic correlations but rather small spin-orbit interaction and thus it is difficult to tune the system into/close to the topological state. 4f and 5f elements pose heavy masses and narrow bands with excpetion of rate Kondo topological insulators [89]. 5d pyrochlore [90] and spinel [55] elements are computationally predicted to host axion states within relatively small window of correlations strength complicating manufacturing the material.

To summarize, the most promissing material systems are intrinsic antriferomagnetic axion insulators [77], magnetically doped topological insulators [42], certain conventional magnetoelectrics [91] and heterostructures of topological insulators [92]. The $\mathcal{PT}$ symmetric antiferromagnetism seems to be favourable over ferromagnetism as it naturaly provides for Dirac quasiparticles with tunable axion quasiparticles masses, longitudinal spin waves, larger spin-flop fields, elevated Néel temperatures, possibility to combine chemistry required for magnetism and spin-orbit coupling in single material platform. We list some of the promissing building block materials and systems for dynamical axion quasiparticles in the table 3.

JCAP08(2021)066

Phase	Material class	T_C (K)	Δ [meV]	Θ
Magnetoelectric	$BiFeO_3$	643	950	0.9×10^{-4} [87]
	Cr_2O_3	343	1300	1.3×10^{-3} [86]
Magnet/TIs	$CrI_3/Bi_2Se_3/MnBi_2Se_4$	>10	5.6	π [92]
Intrinsic $\mathcal{P}$ AFs	$MnBi_2Te_4$	<25	<220	π
	$EuIn(Sn)_2As(P)_2$	16	<100	π
Doped TIs	$Cr(Fe)$-Bi_2Se_3	∼10 [93]	∼30	nonquantized
Intrinsic $\mathcal{PT}$ AFs	$Mn(Eu)_2Bi_2Te_5$	6	∼50	$0.83\,\pi$ [92]

Table 3. Table of magneto-electric insulating material classes and candidates. FM (AF) marks (anti)ferromagnetism, T_C the critical temperature, and Δ the bulk band gap.

Besides listing materials which are directly dynamical axion insulators we added also materials which can be used as starting configurations to build the dynamical axion insulator, for instance, by alloying of the static axion insulators.

We emphasize that the bulk energy bands encode the information about the dynamical axion insulator response, and its surface states [42]. We can see this on expression for the intrinsic magnetoelectric susceptibility, axion coupling, can be calculated in the Bloch representation as [42]:

$$\Theta = -\frac{1}{4\pi}\int_{\mathrm{BZ}} d^3k\epsilon^{\alpha\beta\gamma}\,\mathrm{Tr}\left[\mathcal{A}_\alpha\partial_\beta\mathcal{A}_\gamma - i\frac{2}{3}\mathcal{A}_\alpha\mathcal{A}_\beta\mathcal{A}_\gamma\right]. \tag{2.8}$$

Here we explictily see the axion angle relation to the non-abelian Berry connection $\mathcal{A}_{\alpha,nm}(\mathbf{k}) = \langle u_{n\mathbf{k}}\,|i\partial_{k_\alpha}|\,u_m\rangle$ constructed from the Bloch functions $|u_{n\mathbf{k}}\rangle$. The trace is over occupied valence bands.

The first-principle calculations of the axion angle is reserch topic on its own [56, 59]. For the sake of brevity we will adopt here simpler approach. We can use first-prinicple calculations and symmetry analysis to identify and parametrize low energy effective Hamiltonian for which the calculation of axion angle and its dynamical response is numerically less demanding. We will now describe dynamical axion quasiparticle model which is applicable to Fe-doped Bi_2Se_3 [42] and intrinsic antiferromagnet $Mn_2Bi_2Te_5$ [43] and also heterostructures [92].

2.2.3 Dirac model of axion quasiparticles

We can derive the minimal model of dynamical axion insulator starting from the Dirac quasiparticle model for the bulk states of topological insulator Bi_2Se_3 [94]. The low energy physics can be captured by four-band Hamiltonian in the basis of bonding and antibonding Bi p_z states $|P2_z^-,\uparrow(\downarrow)\rangle$ and $|P1_z^+,\uparrow(\downarrow)\rangle$ [42, 43, 94]:

$$\mathcal{H}_{\mathrm{Dirac}} = \epsilon_0(\boldsymbol{k}) + \sum_{a=1}^{5} d_a(\boldsymbol{k})\Gamma_a. \tag{2.9}$$

Here Γ_a refer to the Dirac matrices representation:

$$\Gamma_{(1,2,3,4,5)} = (\sigma_x \otimes s_x\,, \sigma_x, \otimes s_y, \sigma_y \otimes I_{2\times2}, \sigma_z \otimes I_{2\times2}\,, \sigma_x \otimes s_z) \tag{2.10}$$

in the basis $(|P1_z^+,\uparrow\rangle, |P1_z^+,\downarrow\rangle, |P2_z^-,\uparrow\rangle, |P2_z^-,\downarrow\rangle)$. σ and s are orbital and spin Pauli matrices. The 4×4 matrices Γ_a satisfy the Clifford algebra $\{\Gamma_a,\Gamma_b\} = 2\delta_{ab}$ with $\Gamma_5 = \Gamma_1\Gamma_2\Gamma_3\Gamma_4$.

JCAP08(2021)066

This model can be tuned to the trivial ($\Theta = 0$) or topological insulator state ($\Theta = \pi$). To induce nonzero $\delta\Theta$ and dynamical axion state we need to add $\mathcal{P}$ and $\mathcal{T}$ symmetry breaking terms due to the antiferromagnetism.

The crystal momentum dependent coefficients take the form:

$$d_{1,2,3}(\boldsymbol{k}) = A_{1,2,3}(\boldsymbol{k}) + m_{x,y,z}, \tag{2.11}$$

$$\epsilon_0(\boldsymbol{k}) = C + 2D_1 + 4D_2 - 2D_1 \cos k_z - 2D_2 \left(\cos k_x + \cos k_y\right) \tag{2.12}$$

$$d_4(\boldsymbol{k}) = \mathcal{M}(\mathbf{k}) = M_0 - 2B_1 - 4B_2 + 2B_1 \cos k_z + 2B_2 \left(\cos k_x + \cos k_y\right) \tag{2.13}$$

$$d_5(\boldsymbol{k}) = M_5. \tag{2.14}$$

Here the fourth term $\mathcal{M}(\boldsymbol{k})$ controls the topological phase transition from the trivial to topological insulator, is invariant under $\mathcal{T}$, and we denote $\mathcal{M}(\boldsymbol{k} = 0) = M_0$. The topological insulating phase is achieved when $M, B_1, B_2 > 0$ [94]. The symmetry breaking terms are the masses $m_{x,y,z}$ and M_5 (a $\mathcal{CP}$-odd chiral mass term). We see that the spatial inversion $\mathcal{P} = \sigma_z \otimes I_{2x2}$ and time-reversal operators $\mathcal{T} = iI_{2x2} \otimes s_y\mathcal{K}$ do not commute with the Hamiltonian, while their combination does. Here $\mathcal{K}$ is complex conjugation.

Only the last mass term M_5 induces linear perturbations to Θ as we will show further, and without loss of generality one can set $m_{x,y,z} = 0$. In turn, the M_5 term opens a surface band gap in the surface states Dirac Hamiltonian as we show in figure 3. The A, B, C, D, and masses M, M_5 constants are material dependent and can be determined by fitting the electronic structure calculated from the first-principles [42, 92, 94, 95]. We also remark, that for calculating the complete response of the material we need to know the full periodic Hamiltonian eq. (2.14).

When its sufficient to study small wavector excitations we can use continuum variant, $\boldsymbol{k}, \boldsymbol{p}$-expansion, around momentum points X_f, where $\boldsymbol{q} = \boldsymbol{k} - X_f$:

$$\mathcal{H}_f(\boldsymbol{q}) = q_x\alpha_1 + q_y\alpha_2 + q_z\alpha_3 + M_0\alpha_4 + M_{5f}\alpha_5. \tag{2.15}$$

Here we use the standard Dirac equation basis:

$$\beta = \alpha_4 = \begin{pmatrix} I & 0 \\ 0 & -I \end{pmatrix}, \alpha^{i=1,2,3} = \begin{pmatrix} 0 & \sigma_i \\ -\sigma_i & 0 \end{pmatrix} \Rightarrow \alpha_5 = \begin{pmatrix} 0 & I \\ I & 0 \end{pmatrix}. \tag{2.16}$$

Furthermore, the subscript f denotes the valley degree of freedom in the low-energy electronic band of the system, and can be understood as the Dirac quasiparticle *flavour*. In the AFI phase of the Bi_2Se_3 family doped with magnetic impurities such as Fe [42], there is a single Dirac fermion and $M_{5,1} = M_{5,2} = 0$, $M_{5,3} = -(2/3)Un_z$. (In the AFI phase of the Fu-Kane-Mele-Hubbard (FKMH) model [51], there are three Dirac fermions and $M_{5,a} = Un_a$ $(a = x, y, z)$.) Here, $\boldsymbol{n} = (\langle \boldsymbol{S}_A - \boldsymbol{S}_B)/2 = n_x\boldsymbol{e}_x + n_y\boldsymbol{e}_y + n_z\boldsymbol{e}_z$ denotes the mean-field AF order parameter (i.e., the Néel field, with $\boldsymbol{S}_{A,B}$ the spin of ions on A and B-type lattice sites) and U is the on-site electron-electron interaction strength (i.e. the Hubbard term, see below). The kinetic term $\sum_{\mu=1}^{3} q_\mu\alpha_\mu$ is spin-dependent as a consequence of spin-orbit coupling.

We derive the effective action consisting of the Néel field $\boldsymbol{n} = \boldsymbol{n}_0 + \delta\boldsymbol{n}$ and an external electromagnetic potential A_μ, where $\boldsymbol{n}_0$ denotes the ground state of the Néel field and $\delta\boldsymbol{n}$ denotes the fluctuation due to excitations. For this purpose, it is convenient to adopt a perturbative method. We start with the total action of an AF insulator described by eq. (2.15) with an external electromagnetic potential A_μ:

$$S_{\text{eff}}[\psi, \bar{\psi}, \boldsymbol{n}, A_\mu] = \int dt d^3r \sum_f \bar{\psi}_f(\boldsymbol{r}, t) \left[i\gamma^\mu D_\mu - M_0 + i\gamma^5 M_{5f}\right] \psi_f(\boldsymbol{r}, t), \tag{2.17}$$

JCAP08(2021)066

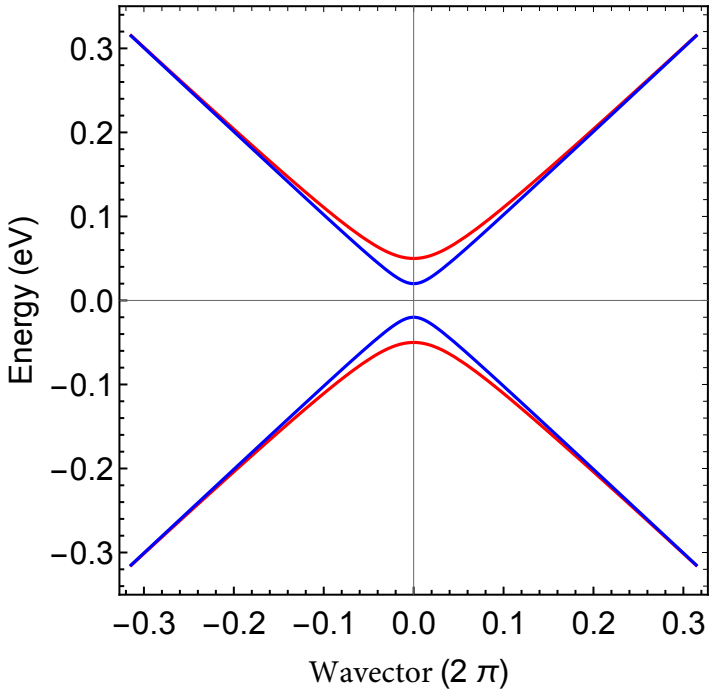

Figure 3. (a) Minimal model energy bands of edge states (red) of dynamical axion insulator with parity and time-reversal breaking antiferromangetic term $M_5 = 0.5M_0$, where M_0 is bulk (blue) Dirac band-gap. The wavector corresponds to given valley index f in the text.

where t is real time, $\psi_f(\boldsymbol{r}, t)$ is a four-component spinor, $\bar{\psi}_f = \psi_f^\dagger \gamma^0$, $D_\mu = \partial_\mu + ieA_\mu$, and we have used the fact that $\alpha_4 = \gamma^0$, $\alpha_5 = -i\gamma^0\gamma^5$ and $\alpha_j = \gamma^0\gamma^j$ $(j = 1, 2, 3)$. Here, the gamma matrices satisfy the identities $\{\gamma^\mu, \gamma^5\} = 0$ and $\{\gamma^\mu, \gamma^\nu\} = 2g^{\mu\nu}$ with $g^{\mu\nu} = \mathrm{diag}(1, -1, -1, -1)$. By integrating out the fermionic field ψ_f, we obtain the effective action W_{eff} for $\boldsymbol{n}$ and A_μ as

$$\begin{aligned} Z[\boldsymbol{n}, A_\mu] &= \int \mathcal{D}[\psi, \bar{\psi}] e^{iS_{\mathrm{eff}}} = \exp\left\{ \sum_f \mathrm{Tr} \ln \left[G_{0f}^{-1}(1 + G_{0f}V_f) \right] \right\} \\ &= \exp\left[\sum_f \mathrm{Tr}\left(\ln G_{0f}^{-1} \right) - \sum_f \sum_{n=1}^{\infty} \frac{1}{n} \mathrm{Tr}\left(-G_{0f}V_f \right)^n \right] \\ &\equiv e^{iW_{\mathrm{eff}}[\boldsymbol{n}, A_\mu]}. \end{aligned} \tag{2.18}$$

In order to obtain the action of the low-energy spin-wave excitation, i.e., the AF magnon, we set the Green's function of the unperturbed part as $G_{0f} = (i\gamma^\mu\partial_\mu - M_0 + i\gamma^5 M_{5f})^{-1}$, and the perturbation term as $V_f = -e\gamma^\mu A_\mu + i\gamma^5 \delta M_{5f}$. Note that we have used $i\gamma^\mu D_\mu - M_0 + i\gamma^5(M_{5f} + \delta M_{5f}) = G_{0f}^{-1} + V_f$. In the random phase approximation, the leading-order terms read

$$iW_{\mathrm{eff}}[\boldsymbol{n}, A_\mu] = -\frac{1}{2} \sum_f \mathrm{Tr}\left(G_{0f} i\gamma^5 \delta M_{5f} \right)^2 + \sum_f \mathrm{Tr}\left[(G_{0f} e\gamma^\mu A_\mu)^2 \left(G_{0f} i\gamma^5 \delta M_{5f} \right) \right], \tag{2.19}$$

where the first and second terms on the right-hand side correspond to a bubble-type diagram and a triangle-type digram, respectively.

To compute the traces of the gamma matrices we use the following identities:

$$\mathrm{tr}(\gamma^\mu) = \mathrm{tr}(\gamma^5) = 0, \quad \mathrm{tr}(\gamma^\mu\gamma^\nu) = 4g^{\mu\nu}, \quad \mathrm{tr}(\gamma^\mu\gamma^\nu\gamma^5) = 0, \quad \mathrm{tr}(\gamma^\mu\gamma^\nu\gamma^\rho\gamma^\sigma\gamma^5) = -4i\epsilon^{\mu\nu\rho\sigma}. \tag{2.20}$$

The first term in eq. (2.19) is given explicitly by

$$\begin{aligned}
\mathrm{Tr}\left(G_{0f}i\gamma^5\delta M_{5f}\right)^2 &= \int \frac{d^4q}{(2\pi)^4}\int \frac{d^4k}{(2\pi)^4}\mathrm{tr}\left[G_{0f}(k)i\gamma^5\delta M_{5f}(q)G_{0f}(k+q)i\gamma^5\delta M_{5f}(-q)\right] \\
&= 4\int \frac{d^4q}{(2\pi)^4}\int \frac{d^4k}{(2\pi)^4}\frac{[k_\mu(k+q)^\mu - M_0^2 + M_{5f}^2]\delta M_{5f}(q)\delta M_{5f}(-q)}{(k^2 - M_0^2 - M_{5f}^2)[(k+q)^2 - M_0^2 - M_{5f}^2]} \\
&\equiv \int \frac{d^4q}{(2\pi)^4}\Pi_f(q)\delta M_{5f}(q)\delta M_{5f}(-q),
\end{aligned} \tag{2.21}$$

where $k^2 = g^{\mu\nu}k_\mu k_\nu = k_\mu k^\mu = k_0^2 - \boldsymbol{k}^2$. We have used $G_{0f}(k) = (\gamma^\mu k_\mu + M_0 + i\gamma^5 M_{5f})/(k^2 - M_0^2 - M_{5f}^2)$, $\{\gamma^\mu, \gamma^5\} = 0$, and $\{\gamma^\mu, \gamma^\nu\} = 2g^{\mu\nu}$. After performing a contour integration, we arrive at the action of the form

$$\sum_f \mathrm{Tr}\left(G_{0f}i\gamma^5\delta M_{5f}\right)^2 = i\sum_f J_f \int dtd^3r\left[(\partial_\mu\delta M_{5f})(\partial^\mu\delta M_{5f}) - m_f^2(\delta M_{5f})^2\right], \tag{2.22}$$

where J_f and m_f are the stiffness and mass of the spin-wave excitation mode, which are given respectively by [42]

$$J_f = \left.\frac{\partial^2\Pi_f(q)}{\partial q_0^2}\right|_{q\to 0} = \int_{\mathrm{BZ}}\frac{d^3k}{(2\pi)^3}\frac{\sum_{i=1}^4 d_i^2}{16|d|^5}, \tag{2.23}$$

$$J_f m_f^2 = \Pi_f(q)|_{q\to 0} = M_{5f}^2\int_{\mathrm{BZ}}\frac{d^3k}{(2\pi)^3}\frac{1}{4|d|^3}, \tag{2.24}$$

where $|d| = \sqrt{\sum_{a=1}^5 d_a^2}$, $q \to 0$ indicates the limit of both $q_0 \to 0$ and $\boldsymbol{q} \to \boldsymbol{0}$, and here f denotes the flavour. Equation (2.22) is nothing but the action of the Néel field described by the non-linear sigma model [96]. In the present low-energy effective model [eq. (2.17)], the information on the anisotropy of the Néel field is not included. On the other hand, many (actual) AF insulators have the easy-axis anisotropy. Hence the term $\sum_f m_f^2\delta n_f^2$ will be replaced by a term like $m^2(\delta\boldsymbol{n}\cdot\boldsymbol{e}_A)^2$ with $\boldsymbol{e}_A$ denoting the easy axis. The second term in eq. (2.19) is the triangle anomaly, which gives the Chern-Simons term. The final result is [97, 98]

$$\begin{aligned}
\sum_f \mathrm{Tr}\left[\left(G_{0f}e\gamma^\mu A_\mu\right)^2\left(G_{0f}i\gamma^5\delta M_{5f}\right)\right] &= i\frac{\alpha}{2\pi}\int dtd^3r\delta\Theta(\boldsymbol{r},t)\epsilon^{\mu\nu\rho\lambda}\partial_\mu A_\nu\partial_\rho A_\lambda \\
&= i\frac{\alpha}{\pi}\int dtd^3r\delta\Theta(\boldsymbol{r},t)\boldsymbol{E}\cdot\boldsymbol{B},
\end{aligned} \tag{2.25}$$

where [51]

$$\delta\Theta(\boldsymbol{r},t) = \sum_f \tan^{-1}\left[\frac{M_f + \delta M_{5f}(\boldsymbol{r},t)}{M_0}\right] - \sum_f \tan^{-1}\left[\frac{M_f}{M_0}\right] \approx -\sum_f \frac{\delta M_{5f}(\boldsymbol{r},t)}{M_0}. \tag{2.26}$$

JCAP08(2021)066

From eq. (2.25) we find that the fluctuation of the γ^5 mass M_{5f} behaves just as a dynamical axion field. From eqs. (2.22) and (2.25), we finally arrive at the action of the AQ [42, 99]:

$$S_{\mathrm{AQ}} = M_0^2 J \int dt d^3r \left[(\partial_\mu \delta\Theta)(\partial^\mu \delta\Theta) - m_\Theta^2 \delta\Theta^2 \right] + \frac{\alpha}{\pi} \int dt d^3r \delta\Theta(\boldsymbol{r}, t) \boldsymbol{E} \cdot \boldsymbol{B} \,, \tag{2.27}$$

where have used that for systems described by the Dirac Hamiltonian (eq. (2.15)) the quantity labelled g in the action given in ref. [42] can be set equal to the bulk band gap M_0. We identify the decay constant as $M_0^2 J = {f_\Theta}^2/2$, and note that the spin wave speed appears in the spatial derivatives by choice of units.

2.3 AQ as longitudinal magnon

For concreteness, let us consider the AF insulator phase of $(\mathrm{Bi}_{1-x}\mathrm{Fe}_x)_2\mathrm{Se}_3$ and $\mathrm{Mn_2Bi_2Te_5}$ such that there is a single degree of freedom with $M_{5,1} = M_{5,2} = 0$, and $M_{5,3} = -(2/3)Un_\parallel$, where $n_\parallel$ is parallel to the easy-axis anisotropy. In terms of the AF order parameters the AQ is given by expanding eq. (2.26), leading to

$$\delta\Theta \approx \frac{2U}{3M_0} \delta n_\parallel \,. \tag{2.28}$$

Thus, we see that the AQ $\delta\Theta$ is the longitudinal fluctuation in the AF order.

The EFT of *transverse* magnons is presented in appendix A.1, and is based on the Heisenberg model. The Heisenberg model is the strong coupling limit of the Hubbard model used to describe the AQ, but nonetheless it provides some insight into the physics, which we discuss briefly. The EFT describes the AF order parameter, $\boldsymbol{n}$. Let us denote the components of $\boldsymbol{n}$ as $n_\parallel$ along the easy-axis and $n_{\perp,1,2}$ orthogonal to it. In the EFT we have that:

$$\delta n_\parallel \approx -\frac{\delta n_{\perp,1}^2}{2} - \frac{\delta n_{\perp,2}^2}{2} \,. \tag{2.29}$$

Thus the AQ is related *non-linearly* to the transverse magnons of the Heisenberg EFT.

In the Dirac model for the AQ, the interaction between $\delta\Theta$ and electromagnetism is given entirely by the chiral anomaly, i.e. the interaction $\delta\Theta \boldsymbol{E} \cdot \boldsymbol{B}$. On the other hand the Heisenberg EFT contains the spin interaction $\mathcal{L}_{\mathrm{em}} = \mu_B \boldsymbol{s} \cdot \boldsymbol{H}$, with $\boldsymbol{s} = \dot{\boldsymbol{n}} \times \boldsymbol{n}$ at leading order. As we have just established, however, the Heisenberg model fields are not linearly related to the AQ in the Hubbard model with $t/U \ll 1$. We therefore neglect the interaction $\mathcal{L}_{\mathrm{em}}$ in our subsequent calculations based on the effective action eq. (2.27). If only the axion, $\delta\Theta \propto \delta n_\parallel$, is present, then indeed $\dot{\boldsymbol{n}} \times \boldsymbol{n} = 0$.

However, if the AFMR fields $\delta n_\perp$ are also excited, then $\mathcal{L}_{\mathrm{em}}$ mixes the fields and leads to the Kittel shift in the frequencies of these fields $\omega = \mu_B H_0 + \sqrt{m_s^2 + v^2 k^2}$ (see appendix A.1). The Kittel shift would also mix the AFMR fields with the axion. It is not clear to us how to model these two effects, the AQ and AFMR with an applied field, at the same time because the two descriptions are valid in opposite regimes of the Hubbard model parameters. The splitting $\mu_B H_0 \ll m_s$ for fields $H_0 \sim 1$ T, and so our subsequent results would not be changed drastically by such an effect. Nevertheless, the splitting may be possible to observe experimentally if it is present. This remains an open question.

We have not been able to derive an EFT for the AQ longitudinal magnon along the same lines as the EFT of AFMR given in the appendix. One possibility for such a theory generalises the AF-ordering to a general spin density wave ordering vector $\boldsymbol{Q}$. In this case,

JCAP08(2021)066

Symbol	Name	$(Bi_{1-x}Fe_x)_2Se_3$		$Mn_2Bi_2Te_5$	
$\mu_B H_E$	Exchange	1 meV	[105]	0.8 meV	[92]
$\mu_B H_A$	Anisotropy	16 meV	[102]	0.1 meV	[92]
$V_{\text{u.c.}}$	Unit cell volume	440 Å^3		270 Å^3	
U	Hubbard term	3 eV	[102]	3 eV	[92]
M_0	Bulk band gap	0.03 eV (0.2 eV)	[102]	0.05 eV	[92]
t	Nearest neighbour hopping[a]	0.04 eV		0.04 eV	
S	Magnetic moment	4.99	[102]	4.59	[92]
T_N	Néel temperature	10 K	[93]	6 K[b]	
ϵ_1	Dielectric constant	25 (100)		25	

[a] The hopping parameters t are derived from H_E assuming half-filling.
[b] Estimated from the Liechtenstein magnetic force theorem, $T_N = 3\mu_B H_E/2k_B$ [106].

Table 4. Material parameters for AQ materials. $Mn_2Bi_2Te_5$ has not been experimentally realised, and parameters in the references are calculated *ab initio*, rather than measured. Values in parentheses were assumed in ref. [42]. We assume the dielectric constants for both materials are equal to the undoped Bi_2Se_3 extrapolated to low energy [103, 104].

one arrives at a quadratic Lagrangian for the transverse and longitudinal magnons[2] with coupling to external sources [88]. However, in addition to these desired ingredients there are also spinor degrees of freedom, the "holons" describing the spin-charge separation. Another possibility, which we suggest, is to generalise the Néel order parameter to an SU(2) doublet with the AQ a Goldstone boson associated to a Chiral U(1) subgroup under which the Dirac quasiparticles are charged.

2.4 Parameter estimation

Three unknown quantities determine the AQ model: the mass m_Θ, decay constant f_Θ, and speed v_s (from the spatial derivatives, giving the wave speed). We generally work in the limit $v_s \ll c$ and ignore the magnon dispersion relative to the E-field. This leaves two parameters, m_Θ and f_Θ. We show in detail in section 3.1 how both m_Θ and f_Θ can be determined experimentally from the polariton resonances and gap via transmission spectroscopy (related to the total reflectance measurement proposed by ref. [42]). In this section, however, we wish to estimate these parameters from known material properties.

We consider two candidate materials, firstly the magnetically doped TI $(Bi_{1-x}Fe_x)_2Se_3$ of ref. [42]. Reference [102] considered a number of different TIs doped with different magnetic ions, and found that only $(Bi_{1-x}Fe_x)_2Se_3$ is both antiferromagnetic and insulating. $(Bi_{1-x}Fe_x)_2Se_3$ has been successfully fabricated. However, the magentism is fragile due to the doping (required around 3.5%), and the region of the phase diagram exhibiting the AQ is small. Therefore, we also consider the new class of intrinsically magnetic TIs, $Mn_xBi_yTe_z$, of which only $Mn_2Bi_2Te_5$ is thought to contain an AQ, but has yet to be fabricated. Material properties for both cases are listed in table 4, while the derived parameters are given in table 5. Our estimates for the derived parameters are discussed in the following.

The microscopic model for the AQ is derived from the Hubbard model in the weak coupling limit. In the Hubbard model, one allows hopping of spins between lattice sites. The

[2]Other approaches to the longitudinal mode include refs. [100, 101].

JCAP08(2021)066

Symbol	Name	Equations	"Material 1"	"Material 2"
m_Θ	AQ mass	(2.35), (2.38)	2 meV	1.8 meV
f_Θ	AQ decay constant	(2.34), (2.37)	30 eV	70 eV

Table 5. Derived AQ parameters. "Material 1" is our best approximation to $(Bi_{1-x}Fe_x)_2Se_3$. We report the results of ref. [42], who assumed a cubic lattice to evaluate the band integrals, but rescaled by our values of M_0. We use a combination of normalisation to the cubic lattice result, and the material properties in table 4 to estimate the parameters for "Material 2", our best approximation to $Mn_2Bi_2Te_5$.

Hubbard Hamiltonian is:

$$H = -t \sum_{\langle ij \rangle, \sigma} a^\dagger_{i\sigma} a_{j\sigma} + U \sum_i n_{i\uparrow} n_{i\downarrow}, \tag{2.30}$$

where $a^\dagger_{i\sigma}$ and $a_{i\sigma}$ are the creation and annihilation operators for a spin σ at lattice site i and the first sum is over nearest neighbour sites. $n_{i\uparrow}$ and $n_{i\downarrow}$ are the spin up and spin down density operators for the ith lattice site. The first term describes the kinetic energy of the system, whose scale is given by the hopping parameter t. The second term describes the interaction between spins on the same site, with scale given by the Hubbard term U. In the limit of half filling and $U \gg t$, the Hubbard model is equivalent to a Heisenberg model with $J_H \sim t^2/U$ [107]. The exchange field is related to the Heisenberg Hamiltonian via eq. (A.15) as

$$H_E = \frac{2SJ_H}{g\mu_B}, \tag{2.31}$$

where S is the ion spin and g is the spectroscopic splitting factor [108] (see appendix A for more details). This relation was used in table 4 to set the hopping parameter t given U, S and $\mu_B H_E$ and taking $g = 2$.

The electron band energies d_i, eqs. (2.23), (2.24), appearing in the microscopic model are normalized with respect to t. The Brillouin zone (BZ) momentum, k, on the other hand, is normalised with respect to the unit cell. This suggests normalizing the integrals eqs. (2.23), (2.24) as (we consider only the case with a single Dirac fermion from now on and drop the subscript f):

$$J = \int_{\mathrm{BZ}} \frac{\mathrm{d}^3k}{(2\pi)^3} \frac{\sum_i d_i^2}{16|d|^3} = \frac{\mathcal{I}_1}{V_{\mathrm{u.c.}} t^3}, \tag{2.32}$$

(note that this J is not Heisenberg J_H, in fact $J_H \propto 1/J$) and

$$m_\Theta^2 J = M_5^2 \int_{\mathrm{BZ}} \frac{\mathrm{d}^3k}{(2\pi)^3} \frac{1}{4|d|^3} = M_5^2 \frac{\mathcal{I}_2}{V_{\mathrm{u.c.}} t^3}, \tag{2.33}$$

where $V_{\mathrm{u.c.}}$ is the volume of the unit cell. It then follows that the AQ mass is:

$$m_\Theta = M_5 \sqrt{\frac{\mathcal{I}_2}{\mathcal{I}_1}} = \frac{2SU}{3} \sqrt{\frac{\mathcal{I}_2}{\mathcal{I}_1}}. \tag{2.34}$$

Notice that for an exact Dirac dispersion for d, the integrals over the BZ vanish if the Dirac mass, M_0, vanishes, as we expect from the Gell-Mann-Oakes-Renner relation [109]. However, these integrals should be evaluated for d's computed in the full theory, i.e. *ab initio* density functional theory for the Hubbard model.

JCAP08(2021)066

In the full theory, the normalized integrals $\mathcal{I}$ depend on the ratio t/U. In terms of the Hubbard model parameters we have $M_5 = (2/3)Un_z$, where $n_z = S$ is the normalised AF order. The decay constant is:

$$f_\Theta{}^2 = 2M_0^2 \frac{\mathcal{I}_1}{V_{\text{u.c.}} t^3} \,. \tag{2.35}$$

Using a cubic lattice model, ref. [42] computed the BZ integrals for $(Bi_{1-x}Fe_x)_2Se_3$. The integrals depend on the ratio t/U, so we can also use this result for $Mn_2Bi_2Te_5$ if we extract the values of the normalised integrals.

Reference [42] report $b = 0.2\,\text{meV}$ at 2 T and $m_\Theta = 2\,\text{meV}$. Ref. [42] assumed values for the dielectric constant (taken at the gap instead of near the spin wave resonance) and bulk band gap (taken from the model without doping [94]) of $(Bi_{1-x}Fe_x)_2Se_3$, which we wish to update (in table 4, the values assumed by ref. [42] are given in parentheses). Fortunately, both of these quantities can be factored out of the relevant expressions to arrive simply with the normalised integrals. We find:

$$\mathcal{I}_1 = 4 \times 10^{-7} \,, \quad \mathcal{I}_2 = 4\mathcal{I}_1 \times 10^{-8} \,. \tag{2.36}$$

Leading to the derived model parameters:

$$f_\Theta = 30\,\text{eV} \left(\frac{M_0}{0.03\,\text{eV}}\right)^{0.5} \left(\frac{V_{\text{u.c.}}}{440\text{Å}^3}\right)^{-0.5} \left(\frac{t}{0.04\,\text{eV}}\right)^{-1.5} \left(\frac{\mathcal{I}_1}{4\times10^{-7}}\right)^{0.5} \tag{2.37}$$

$$m_\Theta = 2\,\text{meV} \left(\frac{S}{4.99}\right) \left(\frac{U}{3\,\text{eV}}\right) \left(\frac{\mathcal{I}_2/\mathcal{I}_1}{4\times10^{-8}}\right)^{0.5} \,. \tag{2.38}$$

The derived parameters are presented in table 5, where we adopt the less committal names "Material 1" and "Material 2" for $(Bi_{1-x}Fe_x)_2Se_3$ and $Mn_2Bi_2Te_5$ respectively, to acknowledge the limitations of our estimates.

Note that in table 4 we quote the anisotropy field μH_A, but that this plays no role in our estimation of the AQ parameters. The anisotropy field in fact determines the *transverse* magnon masses (see appendix A.1), and not the mass of the longituninal AQ. In Paper I we mistakenly assumed to use the transverse magnon mass for the AQ (along with a doping fudge factor). The transverse and longitudinal modes turn out to have similar masses. While we do not know of a fundamental reason for this coincidence, they are both clearly governed by the same $\mathcal{O}(\text{meV})$ magnetic energy scales.

Finally, we mention the important *spin flop transition* (for a detailed description and bibliography, see ref. [110]). Large magnetic fields cause spins to align and induce net magnetization. The magnetization increases linearly for fields larger than the spin-flop field, H_{SF}, eventually destroying the AF order. The spin flop field for $MnBi_2Te_4$ is 3.5 T [76]. In easy axis systems, the AF order is destroyed completely when the magnetization saturates. This occurs at the *spin flip transition* for fields larger than the exchange field, H_E. Large applied fields that destroy AF order will also destroy the AQ. For the exchange fields given in table 4 we expect these transitions to happen in the many Tesla regime. In the following we consider fields up to 10 T for illustration.

2.5 Damping and losses

As discussed below, the magnon and photon losses are crucial in determining how effective an AQ material is for detection of DM. In order to detect the AQ and measure its properties, it is essential that any experiment is carried out at temperatures below the Néel temperature.

JCAP08(2021)066

Type of losses	Symbol	Parameterisation	Reference values	Comments
Conductance	Γ_ρ	$\epsilon_2\,\omega$	$10^{-4}\,\omega$	Extrapolated from optical wavelengths
Gilbert damping	$\Gamma_{\rm lin}$	$\alpha_{\rm G}\,(1+\chi_m^{-1})\,\omega$	$10^{-9}\,\omega$	χ_m given in ref. [111]†
Magnon scattering	Γ_{4m}	n/a		Boltzmann-suppressed for $T < m$
Impurities & domains	$\Gamma_{\rm cryst.}$	$(\delta L/L)\,\omega$	$[10^{-4}, 10^{-3}]\,\omega$	Typical impurity scale $L \sim 1\,\mu$m [111]

† We thank Chang Liu for providing this result.

Table 6. Summary of the loss model. Elements of $\mathbf{\Gamma}$ are specified before diagonalising the kinetic term (see eq. (3.28)). The only E-field loss is the conductance. The total AQ loss is given by the sum of the remaining terms. Loss channels deemed negligible include AQ decay to photons, AQ-photon scattering, and off-diagonal losses.

Fortunately both candidate materials have $T_N > 4\,$K, and so initial measurements can be made at more accessible liquid Helium temperatures. As we discuss below, there are at least two sources of loss (conductance, and magnon scattering) that become less important at low temperatures. When using AQ materials to search for DM, it could therefore be advantageous to operate at $T \ll \omega_a$ dilution refrigerator temperatures.

2.5.1 Resistivity and the dielectric function

Material conductance (inverse resistivity) appears in the E-field equations of motion as a damping term $\Gamma_\rho = 1/\rho = 0.6\,{\rm meV}\,[\rho/\Omega\,{\rm cm})]^{-1}$, from which we see that a resonance near 1 meV requires $\rho \gg 1\,\Omega\,$cm) for $Q = \omega/\Gamma \gg 1$. For a resonance involving the electric field, one requires large resistance, i.e. low conductance.

Ref. [112] measure ρ in the optical ($\omega \sim 1\,$eV) at $T \approx 1\,$K of $\rho = 2\times10^{-3}\,\Omega\,$cm for undoped Bi_2Se_3, lowering to $\rho = 5\times10^{-4}\,\Omega\,$cm with doping. However, it is shown that annealing the TI at high T can increase ρ to be as large as $1\,\Omega\,$cm. For $MnBi_2Te_4$ the situation is similar, with two different measurements giving a longitudinal $\rho \approx 10^{-3}\,\Omega\,$cm at $T \sim \mathcal{O}(\text{few K})$ [113]. In the case of $MnBi_2Te_4$, resistivity can be raised by doping with antimony (Sb) [114]. Even so, topological insulators are actually very poor insulators at typical electronic frequencies.

The measurements of bulk ρ for both Bi_2Se_3 and $MnBi_2Te_4$ are taken at high energy near the band gap around 1 eV, and far from the spin wave resonance frequency at low energies. References [103, 104] studied the dielectric function of Bi_2Se_3 as a function of probe wavelength for the trigonal and orthorhombic phases. The complex dielectric function is $\tilde\epsilon(\omega) = \epsilon_1 - i\epsilon_2$. For energies below the gap, $E \lesssim 1\,$eV, ϵ_1 has value around 25 at the longest wavelenths measured and is only slowly decreasing, while ϵ_2 tends to zero rapidly at large wavelengths in the trigonal case (which is thus more favourable for our purposes). The value of ϵ_1 is considerably smaller than the $\epsilon_1 = 100$ estimate used in Paper I and assumed in ref. [42]. As we show below, smaller values of ϵ_1 are highly desirable for DM detection.

The resistivity is given by $\rho(\omega) = 1/[\omega\epsilon_2(\omega)]$. A narrow linewidth on resonance requires to $\epsilon_2(\omega_+) \ll 1$. Measurements in ref. [104] extend to a maximum wavelength 2800 nm where $\epsilon_2 \sim 1$. A simple power law extrapolation to THz wavelengths gives $\epsilon_2(1\,{\rm meV}) = 9.5\times10^{-5}$ (see figure 4). Thus, the resistivity on the polariton resonance at wavelengths of order 1 mm is significantly higher than the bulk measurements in the optical. The value of ϵ_2 is different for different crystal structures of Bi_2Se_3, and we consider only the most favourable case with

JCAP08(2021)066

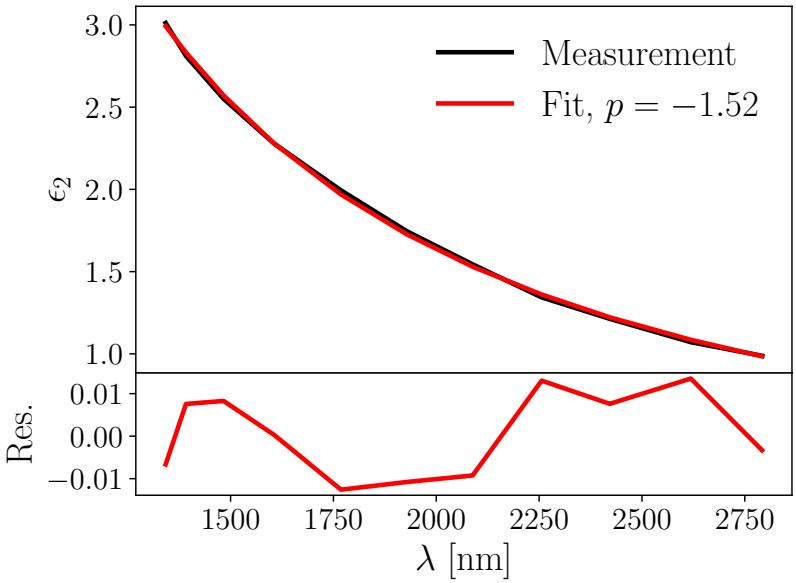

Figure 4. Bi_2Se_3 dielectric function, ϵ_2, as a function of wavelength λ in the optical regime ($\omega \approx 1\,\text{eV}$). Measurements are from refs. [103, 104] for the more favourable trigonal case. The results are well fit by a powerlaw, $\epsilon_2 \propto \lambda^p$ with $p = -1.52$.

the highest resistivity. We take the value $\epsilon_2 = 10^{-4}$ as a reference scale, however, we do not include any further frequency dependence, which would certainly be different for different materials, such as $Mn_2Bi_2Te_5$. The resistivity on resonance can be determined from the linewidth as measured by THz transmission spectroscopy, as we demonstrate in section 3.2.

2.5.2 Magnon losses

As we have discussed, the AQ is not described by the same EFT as ordinary AF-magnons. However, due to the relation between the AQ and the magnon fluctuation, we use the well-studied magnon case as a means to assess the possible magnitude of the axion linewidth, and the qualitative possibilities. Furthermore, as we will see, the dominant contribution is estimated to be due to material impurities, which do not depend on the microscopic model for the AQ. We split the magnon losses into different contributions:

$$\Gamma_m = \sum_i \Gamma_i, \tag{2.39}$$

where the index i sums over terms defined in the following subsections.

Ref. [115] gives a comprehensive account of non-linear wave dynamics relevant to the magnon linewidth. Early works on magnon scattering and linewidth include ref. [116]. The recent pioneering work of refs. [117, 118] showed how neutron diffraction with energy resolution down to 1 μeV can be used to confirm the theoretical predictions for the AF-magnon linewidth, and the dependence on temperature and momentum across the whole Brillouin zone, including many of the contributions discussed in the following. We focus on a few channels for losses, by means of example, closely following ref. [118]. Scattering channels that we have not considered include AF-magnon-ferromagnetic magnon scattering, and magnon-phonon scattering: these are discussed in e.g. ref. [115].

JCAP08(2021)066

In the present work, we are only concerned with the $q \approx 0$ mode at $T \ll T_N$, where many contributions can be neglected. In this regime, as we show in section 3.2, the total AQ contribution to the linewidth can be measured using THz transmission spectroscopy.

"Linear" losses and Gilbert damping, Γ_{lin}

Losses are historically incorporated for spin waves by the introduction of the phenomenological Gilbert damping term into the Landau-Lifshitz equation, making the Landau-Lifshitz-Gilbert (LLG) equation. Gilbert damping is a linear loss, since it simply represents decay of spin waves due to torque. There is not a universally accepted first principles model of Gilbert damping. One possible model is presented in ref. [119], where Gilbert damping is shown to arise due to spin orbit coupling in the Dirac equation (other models include refs. [120, 121]). In this case, the damping term is written as:

$$\Gamma_{\text{lin}} = \alpha_{\text{G}}(1 + \chi_m^{-1})\omega\,. \quad \alpha_{\text{G}} = \frac{e\mu\Sigma_s}{8m_e^2}\,, \tag{2.40}$$

where m_e is the electron mass and χ_m is the dimensionless magnetic susceptibility (volume susceptibility in SI units), and $\Sigma_s = S/V_{\text{u.c.}}$. The dimensionless prefactor α_{G} is of order 10^{-12} for $(Bi_{1-x}Fe_x)_2Se_3$ and $Mn_2Bi_2Te_5$. The value of χ_m was measured for $MnBi_2Te_4$ in ref. [111] and found to be of order $\chi_m \approx 10^{-3}$ for $T < T_N$ (see table 6). Thus the relative width, Γ/ω, is of order 10^{-9}, which is negligible compared to the other sources of loss in the following. Furthermore, χ_m is small enough to be neglected in the magnetic permeability (with $c = 1$), $\mu_m = 1 + \chi_m$, which we fix to unity.

Magnon-magnon scattering, Γ_{4m}

Reference [118] showed that two-to-two magnon scattering is the dominant contribution to the linewidth above ~ 10 K in the antiferromagnets Rb_2MnF_4 and MnF_2 as measured by neutron scattering. The linewidth at 10 K due to this process is $\Gamma_m \approx 10\,\mu$eV, falling rapidly at lower temperatures. We will show how this behaviour arises below. Indeed, as noted in [117], for $q \to 0$ and $T \to 0$, all scattering contributions to the magnon linewidth vanish. Ref. [117] also find that this is true for scattering between the magnon and longitudinal spin fluctuations such as the axion. We find it useful to derive in some detail the scattering contribution to the linewidth, and demonstrate why it vanishes at low temperature, since this is the most well understood part of our loss model.

The magnon modes obey a Boltzmann equation. Mode coupling via non-linearities induces an effective lifetime for any initial configuration. Mode coupling arises from the four-magnon amplitude:

$$\delta\theta(k_1) + \delta\theta(k_2) \longleftrightarrow \delta\theta(k_3) + \delta\theta(k_4)\,, \tag{2.41}$$

which has matrix element $\mathcal{M}(k_1, k_2, k_3, k_4)$, and is shown in figure 5. The state with momentum k_1 is the mode in the condensate of interest, k_2 is a thermal magnon. Magnons k_3 and k_4 are modes scattered out of the condensate, and thus losses. This matrix element appears in the collisional Boltzmann equation for the magnon distribution function $f_1 \equiv f(k_1)$ as

JCAP08(2021)066

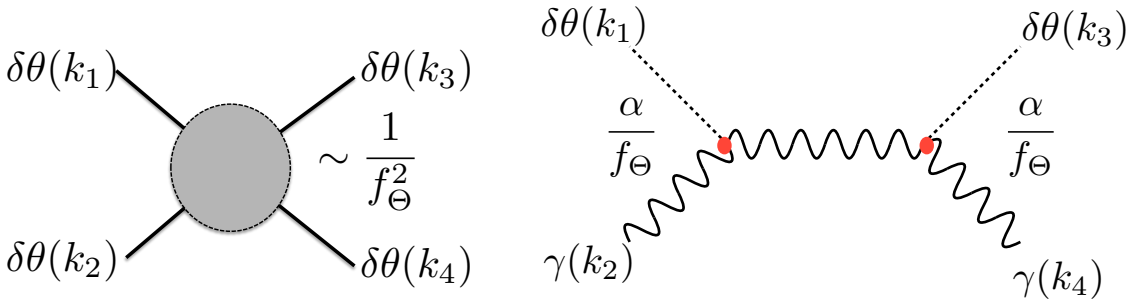

Figure 5. *Left*: four magnon scattering. In EFT, the amplitude can be calculated as shown in ref. [122]. As shown in ref. [118], it is the leading contribution to the magnon linewidth for $T \sim T_N$. For temperatures far below the spin wave mass, this term is Boltzmann suppressed. *Right*: feynman diagram for the s-channel of the process eq. (2.49) mediated by the axion term in the Lagrangian. The parametric dependence of the vertex factors is shown in red. This process is suppressed by two powers of α compared to the four magnon amplitude, eq. (2.45).

(see e.g. ref. [123]):

$$\frac{\mathrm{d}f_1}{\mathrm{d}t} = \int \prod_{i=2}^{4} \mathrm{d}\Phi_i (2\pi)^4 \delta^{(3)}(k_1 + k_2 - k_3 - k_4)\delta(\omega_1 + \omega_2 - \omega_3 - \omega_4)$$
$$|\mathcal{M}|^2 [f_3 f_4 (1+f_1)(1+f_2) - f_1 f_2 (1+f_3)(1+f_4)]\,, \tag{2.42}$$
$$= -\int \frac{\mathrm{d}^3 k_2}{(2\pi)^3} f_1 f_2 |v_1 - v_2| \sigma\,, \tag{2.43}$$

where $\mathrm{d}\Phi_i = \frac{d^3 k_i}{(2\pi)^3}$ is the *non-relativistic* phase space element for state with momentum k_i, the Dirac delta's enforce energy-momentum conservation, k_i represents the 3-momentum of the ith particle, and the f_i factors assume the particles are bosons. Ref. [118] caution that when such integrals are evaluated numerically, one should be careful to include the Umklapp processes, related to conservation of crystal momentum.v

We formulate the integral non-relativistically as the material picks out a preferred frame for the magnons. In the second line, the first term in the square brackets represents production of states k_1, k_2 (the inverse process in eq. (2.41)), while the second term represents losses. In the last line we have assumed $f_3 = f_4 = 0$ for unoccupied final states, and used the definition of the differential cross section (this structure is familiar from particle physics scattering theory [124]). Ref. [115] derives an equivalent equation beginning from the LLG equation, which also shows this non-linear loss term explicitly in terms of the four-magnon amplitude.

Eq. (2.43) is the collisional Boltzmann equation, $\partial_t f_1 = C[f_1]$, where $C[f_1]$ is the scattering integral. Factoring out f_1 for the condensate, the scattering integral takes the form $C[f_1] \sim 1/\tau$ and we identify the relaxation time τ for the distribution function to change significantly from its initial state. This gives the result that:

$$\Gamma_{4m} = 1/\tau \sim \langle \sigma v \rangle\,, \tag{2.44}$$

where the angle brackets denote the thermal average, i.e. phase space integral with the thermal distribution f_2.

JCAP08(2021)066

Magnons can be described by EFT, as discussed in appendix A.1. The four magnon amplitude is given by the equivalent of the QCD pion amplitude evaluated around non-zero quark masses [122].

$$\mathcal{M} = \frac{1}{4\sqrt{\omega_1\omega_2\omega_3\omega_4}}\frac{v_m^4}{F_2^2}\Bigg\{\delta^{ab}\delta^{cd}\left(\frac{2}{v_m^2}\omega_1\omega_2 - 2k_1\cdot k_2 + m_m^2\right) + \delta^{ac}\delta^{bd}\left(-\frac{2}{v_m^2}\omega_1\omega_3 + 2k_1\cdot k_3 + m_m^2\right) + \delta^{ad}\delta^{bc}\left(-\frac{2}{v_m^2}\omega_1\omega_4 + 2k_1\cdot k_4 + m_m^2\right)\Bigg\}, \tag{2.45}$$

where $a, b, c, d = 1, 2$ denote the magnon polarizations, v_m is the magnon velocity and m_m is the magnon mass.

This is the amplitude appropriate to a non-relativistic normalization, with 1 particle per unit volume rather than the usual 2ω particles per unit volume in relativistic quantum mechanics.

In this case, the cross section is related to the T-matrix above as [122]:

$$d\sigma = \frac{|\mathcal{M}|^2}{v}(2\pi)^4\delta^4(k_1 + k_2 - k_3 - k_4)\frac{d^3k_3}{(2\pi)^3}\frac{d^3k_4}{(2\pi)^3}, \tag{2.46}$$

where $v = |v_1 - v_2|$ is the relative velocity of the incoming particles.

We integrate over k_3 and k_4 to obtain the total cross section for given incoming momenta k_1 and k_2:

$$\sigma(k_1, k_2) = \int \frac{d^3k_3}{(2\pi)^3}\frac{d^3k_4}{(2\pi)^3}d\sigma = \int \frac{dk_4}{(2\pi)^3}d\Omega k_4^2\frac{|\mathcal{M}|^2}{v}(2\pi)\delta(\omega_1 + \omega_2 - \omega_3 - \omega_4))\Big|_{(k_1+k_2-k_3-k_4=0)}, \tag{2.47}$$

where $\omega_4 = \sqrt{k_4^2v_m^2 + m_m^2}$ and $\omega_4 = \sqrt{(k_1 + k_2 - k_4)^2v_m^2 + m_m^2}$. At this point in the calculation, we might be tempted to move to the centre of mass frame. However, this would change the magnon velocity v_m, with the new magnon velocity depending on Ω, leading to a magnon dispersion relation that depends on Ω. Therefore, it is in our best interests to remain in the rest frame of the material. We thus obtain the differential cross section:

$$\frac{d\sigma}{d\Omega} = \frac{1}{(2\pi)^2}\frac{1}{v}\frac{|\mathcal{M}|^2k_4^2}{\frac{k_3}{\omega_3} + \frac{k_4}{\omega_4}}, \tag{2.48}$$

where $k_3, \omega_3, k_4, \omega_4$ are defined by conservation of energy and momentum for a given Ω.

Now let us consider the scaling of Γ_{4m} with temperature T. We note first that the factor of v in Γ_{4m} is cancelled by the factor of $\frac{1}{v}$ in $\frac{d\sigma}{d\Omega}$. We will focus first on the scaling of the line widths measured in [118] at temperatures from 3 K to $0.8T_N$ for magnons with momentum $k_1 = 0$ to $k_1 = q_ZB$ at the edge of the zone boundary. The contributions of T to Γ_{4m} are as follows:

- Thermal magnons have an energy set by T. We assume that $T \gtrsim m_m$, such that thermal magnons can be excited. We therefore take $\omega_2 \sim k_2 \sim T$.
- The scaling of the outgoing momenta with T depends on the relative sizes of T and ω_1. The energy at the zone boundary in [118] is 6.6 meV for Rb_2MnF_4 and 6.3 meV for MnF_2, while the temperature ranges from 3 K = 0.26 meV to $0.8\,T_N$, corresponding to

JCAP08(2021)066

2.6 meV and 4.6 meV respectively. Therefore both cases where $T > \omega_1$ and cases where $\omega_1 > T$ are measured. When $T \gg \omega_1$, the temperature provides most of the energy in the scattering process and we have $k_3, \omega_3, k_4, \omega_4 \sim T$. When $T \ll \omega_1$, the energy of the damped magnon provides most of the energy in the scattering process and we have $k_3, \omega_3, k_4, \omega_4 \sim \omega_1$.

- The *number* of thermal magnons also scales with T. Assuming that there is no significant mass gap at $k_2 = 0$ for the magnons considered in [118], we have $\int d^3k_2 f_2 \sim T^3$, as for a black body.
- We have also $\int d^3k_3 d^3k_4 \sim T^2$ when $T \gg \omega_1$ from the factor of k_4^2 in the phase space integral.
- As $T \gtrsim m_m$, the ω_1 and k_1 terms in $\mathcal{M}$ dominate. Using the scalings above, this gives $\mathcal{M} \sim T^{-1/2}$.

Putting these elements together, we find $\Gamma_{4m} \sim T^3 T^2 T^{-1} = T^4$ for $\omega_1 \ll T$ and $\Gamma_{4m} \sim T^3 T^{-1} = T^2$ for $\omega_1 \gg T$. We can compare this prediction with the measured result in figure 4 in [118]. For low magnon wavenumber q (corresponding to low ω_1, we have $\Gamma_{4m} \sim T^4$ as expected. As q is increased, the scaling with T decreases towards $\Gamma_{4m} \sim T^2$ as predicted. However, the measured $\Gamma_{4m} \sim T$ when $q = 0$ case is not explained by this analysis.

We would also expect that for temperatures much lower than the magnon mass, very few thermal magnons would be excited, and Γ_{4m} would be exponentially suppressed. For a magnon mass $m_m \sim 1$ meV, this corresponds to $T < 10$ K.

Starting from the Boltzman equation, we have argued that magnon-magnon scattering decays with T, reproducing the experimentally observed trends in [118], and is then exponentially suppressed at temperatures below the magnon mass. The scattering contribution to the antiferromagnetic magnon linewidth is calculated analytically for several low T regimes in [116]. This yields a power law fall off with T in each case.

We therefore conclude that, at low T, and particularly for temperatures below the magnon mass, the magnon scattering contribution to the linewidth is negligible.

Axion-photon scattering, $\Gamma_{\gamma m}$

Scattering of magnons from thermal photons contributes to the magnon line-width Γ_m. This process is induced by the four particle amplitude

$$\delta\theta(k_1) + \gamma(k_2) \longleftrightarrow \delta\theta(k_3) + \gamma(k_4)\,, \tag{2.49}$$

i.e. magnon/AQ-photon scattering mediated by the Chern-Simons interaction, eq. (2.1). Inspecting the Feynman diagram, figure 5 (right panel), this amplitude is suppressed by two powers of the fine structure constant α with respect to the four magnon amplitude, and so we do not expect magnon-photon scattering to be significant compared with magnon-magnon scattering. The inverse process, scattering thermal magnons from the electric field, is similarly suppressed, and thus likely to be subdominant to conductive losses to $\boldsymbol{E}$.

Axion lifetime, $\Gamma_{m\gamma\gamma}$

The Chern-Simons interaction leads to direct decay of an AQ into two photons. The contribution to the width is:

$$\Gamma_{m\gamma\gamma} = \frac{\alpha^2}{256\pi^3}\frac{m_s^3}{f_\Theta^2} = 6.7 \times 10^{-22}\,\text{eV}\left(\frac{m_s}{\text{meV}}\right)^3\left(\frac{100\,\text{eV}}{f_\Theta}\right)^2\,, \tag{2.50}$$

JCAP08(2021)066

corresponding to a lifetime on the order of months. This process can be safely neglected compared to all other scales in the problem.

Off-diagonal losses

The off-diagonal terms in the loss correspond to loss terms of the form $\frac{d\phi_k}{dt} \sim \langle A_k \rangle$ and $\frac{dA_k}{dt} \sim \langle \phi_k \rangle$. As we generically expect $\frac{d\phi_k}{dt} \sim \langle \phi_k \rangle$ and $\frac{dA_k}{dt} \sim \langle A_k \rangle$, these will all be of the form:

$$\frac{d\phi_k}{dt} \sim \langle A_k \rangle \langle \phi_k \rangle, \tag{2.51}$$

$$\frac{dA_k}{dt} \sim \langle A_k \rangle \langle \phi_k \rangle. \tag{2.52}$$

These off-diagonal loss terms are therefore not present at linear order in the perturbations A_k and ϕ_k.

Impurities and domains, $\Gamma_{\text{cryst.}}$

At low temperatures, the dominant contribution to the magnon linewidth in ref. [118] is attributed to scattering of magnons off magnetic domains and crystal impurities, which is T-independent.

In the simplest picture, scattering from magnetic domains leads to a lifetime:

$$\tau \sim \frac{L_{\text{mag.}}}{2v(q)}\,, \tag{2.53}$$

where $v(q)$ is the velocity of the mode with momentum q, and $L_{\text{mag.}}$ is the size of the domain. The ref. [111] crystals of $MnBi_2Te_4$ have estimated magnetic domain size $L_{\text{mag.}} \sim 1\,\mu$m. We require the axion-polariton to propagate at least through the thickness, d, of the sample, and thus magnetic domains appear to strongly affect the skin depth and resonance width of axion-quasiparticle dominated polaritons in the limit $d \gg L_{\text{mag.}}$.

However, in the $q \to 0$ limit the magnon wavelength exceeds the size of a domain and eq. (2.53) ceases to apply. Furthermore we consider the limit $v_s = 0$ and ignore the magnon propagation compared to the electric field. It is currently unknown how scattering from domains will affect such long wavelength mixed modes. On one hand, it may be that the domain walls appear as small scale fluctuations that decouple from large wavelength modes. Conversely, given that the domain walls disrupt the short range interactions that support the small q magnons it is possible that they have non-trivial effects despite the scale separation.

A second T-independent contribution to the linewidth, which is expected to remain in the $q \to 0$ limit, is due to scattering from impurities. This was accounted for in ref. [118] with the simple phenomenological model for the impurity density:

$$\Gamma_{\text{cryst.}} = \left(\frac{\delta L}{L}\right) \omega(k) \tag{2.54}$$

where δL is the lattice constant, and L is the spacing between impurities, thus $\delta L/L$ is the average number of lattice sites between impurities. The model eq. (2.54) accounts in the same manner for magnetic and crystal impurities. In ref. [111] the crystal impurities occur on the same scale as the magnetic domains, $L_{\text{cryst.}} \sim 1\,\mu$m, while $\delta L \sim (V_{\text{u.c.}})^{1/3} \sim 6$ Å leading to:

$$\Gamma_{\text{cryst.}} = 7 \times 10^{-4} \omega \left(\frac{\delta L}{6\text{ Å}}\right) \left(\frac{1\,\mu\text{m}}{L_{\text{cryst.}}}\right). \tag{2.55}$$

JCAP08(2021)066

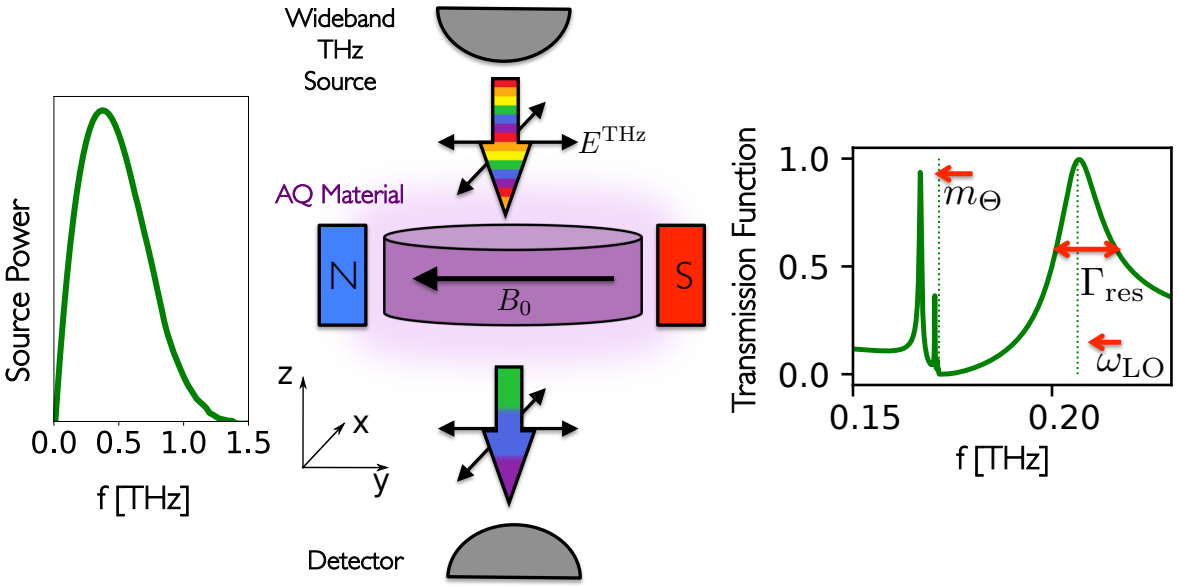

Figure 6. Proposed transmission experiment to detect the axion-polariton. *Left:* THz source power spectrum. *Centre:* transmission experiment concept. A source field, which propagates along the negative z-direction is incident on a TMI. An external B-field B_e is applied parallel to the TMI surface. If AQs exist in the material, the dispersion relation has a gap where no propagating modes exist, thus altering the spectrum of the transmitted radiation. *Right:* theoretical transmission spectrum. The green line corresponds to the case where a dynamical AQ is present. The gap is indicated by the vertical green dotted lines. The width on resonance, Γ_{res}, serves to measure the polariton losses.

We estimate that crystal impurity scattering is the dominant contribution to the AQ linewidth in the regime of interest. Given the lack of conclusive calculations or measurements in the literature (or even, as far as we can tell, a detailed model), we regard this as a question best resolved by experimental studies. Indeed, an understanding of the dynamics of small q magnons and axion-polaritons is an interesting off-shoot of the studies proposed in section 3. However, given the importance of this linewidth contribution to our proposed dark matter search, we must adopt a reference value. We adopt the range given in table 6, $\Gamma_{\mathrm{cryst.}} \in [10^{-4}, 10^{-3}]$ meV, corresponding to impurity separations of order $1\,\mu$m.

3 Discovering the axion quasiparticle

One of the methods proposed by ref. [42] to detect the presence of AQs in TMIs was total-reflectance measurement, and idea we explore further here. In the following we show to compute the transmission function of TMIs using axion electrodynamics. The transmission function is shown to display a gap, leading to total reflectance. Furthermore, by using a wideband THz source, such a measurement can also determine the axion-polariton resonant frequencies, and loss parameters. The concept of this *THz transmission spectroscopy* measurement is shown in figure 6. Similar measurements have been performed on antiferromagents (e.g. ref. [46]), which demonstrate AFMR and determine the magnon linewidth (losses on resonance) for an electromagnetic source.[3] Such a measurement has not to date

[3]Crucially, for our purposes, such a measurement uses precisely the same physics (oscillating E-field source) as occurs for dark axion detection. This is in contrast to neutron scattering of antiferromagnets (e.g. ref. [118]),

JCAP08(2021)066

been performed on any AQ candidate material.

3.1 Axion electrodynamics and boundary conditions

In this section, we review the axion-Maxwell equations for TMIs. We then derive a one-dimensional model as well as the correct interface conditions for all fields involved. Based on the one-dimensional model, we compute the reflection and transmission coefficients for incoming THz radiation.

3.1.1 General formulation

The macroscopic axion-Maxwell equations for a three-dimensional TMI are [42]

$$\nabla \cdot \boldsymbol{D} = \rho_f - \frac{\alpha}{\pi} \nabla(\delta\Theta + \Theta^0) \cdot \boldsymbol{B}\,, \tag{3.1}$$

$$\nabla \times \boldsymbol{H} - \partial_t \boldsymbol{D} = \boldsymbol{J}_f + \frac{\alpha}{\pi} \left(\boldsymbol{B}\partial_t(\delta\Theta + \Theta^0) - \boldsymbol{E} \times \nabla(\delta\Theta + \Theta^0)\right), \tag{3.2}$$

$$\nabla \cdot \boldsymbol{B} = 0\,, \tag{3.3}$$

$$\nabla \times \boldsymbol{E} + \partial_t \boldsymbol{B} = 0\,, \tag{3.4}$$

$$\partial_t^2 \delta\Theta - v_i^2 \partial_i^2 \delta\Theta + m_\Theta^2 \delta\Theta = \Lambda \boldsymbol{E} \cdot \boldsymbol{B}\,, \tag{3.5}$$

where $\delta\Theta$ is the pseudoscalar axion quasiparticle (AQ) field, $\Theta^0 \in [0, \pi]$ a constant, f_Θ^2 the AQ decay constant, v_i (with $i = x, y, z$) is the spin wave velocity, m_Θ the spin wave mass, $\boldsymbol{E}$ is the electric field, $\boldsymbol{B}$ the magnetic flux density, $\boldsymbol{D}$ the displacement field, $\boldsymbol{H}$ the magnetic field strength, ρ_f the free charge density, and $\boldsymbol{J}_f$ the free current density, which fulfill the continuity equation $\nabla \cdot \boldsymbol{J}_f + \dot{\rho}_f = 0$ as in usual electrodynamics. In what follows we often use the linear constitutive relations

$$\boldsymbol{D} = \epsilon \boldsymbol{E} \text{ and } \boldsymbol{H} = \mu^{-1} \boldsymbol{B}, \tag{3.6}$$

where ϵ and μ are the scalar permittivity and permeability, respectively. Note that it is important to include the Θ^0 term in the equations above: while Θ^0 is some constant in the TMI, it is always zero in vacuum. Applying the nabla operator can therefore give a delta function at the boundaries of the TMI, i.e. a boundary charge term.

Equations (3.1) and (3.2) can be written such that the terms including the dynamical AQ field $\delta\Theta$ can be interpreted as additional contributions to polarization and magnetization, i.e.

$$\nabla \cdot \boldsymbol{D}_\Theta = \rho_f\,, \tag{3.7}$$

$$\nabla \times \boldsymbol{H}_\Theta - \partial_t \boldsymbol{D}_\Theta = \boldsymbol{J}_f\,, \tag{3.8}$$

$$\nabla \cdot \boldsymbol{B} = 0\,, \tag{3.9}$$

$$\nabla \times \boldsymbol{E} + \partial_t \boldsymbol{B} = 0\,, \tag{3.10}$$

where we define

$$\boldsymbol{D}_\Theta = \boldsymbol{D} + \frac{\alpha}{\pi} (\Theta^0 + \delta\Theta)\, \boldsymbol{B}\,, \tag{3.11}$$

$$\boldsymbol{H}_\Theta = \boldsymbol{H} - \frac{\alpha}{\pi} (\Theta^0 + \delta\Theta)\, \boldsymbol{E}\,. \tag{3.12}$$

which determines the linewidth for a different excitation mechanism.

JCAP08(2021)066

To derive interface conditions for the electromagnetic fields, we consider two domains labeled 1 and 2. Both domains have different ϵ, μ, and Θ^0. Transforming eqs. (3.7)–(3.10) into their integral representation, and applying Gauss's (Stokes') theorem to an infinitesimal volume (surface) element, leads to the following interface conditions for the electromagnetic fields:

$$\boldsymbol{n} \times (\boldsymbol{E}_2 - \boldsymbol{E}_1) = 0\,, \tag{3.13}$$

$$\boldsymbol{n} \cdot (\boldsymbol{D}_{\Theta,2} - \boldsymbol{D}_{\Theta,1}) = \sigma_S\,, \tag{3.14}$$

$$\boldsymbol{n} \cdot (\boldsymbol{B}_2 - \boldsymbol{B}_1) = 0\,, \tag{3.15}$$

$$\boldsymbol{n} \times (\boldsymbol{H}_{\Theta,2} - \boldsymbol{H}_{\Theta,1}) = \boldsymbol{J}_S\,, \tag{3.16}$$

where σ_S and $\boldsymbol{J}_S$ are free surface charge and current densities (both assumed to be zero in what follows) and $\boldsymbol{n}$ is a unit vector pointing from domain 1 to domain 2. It is important to stress that eqs. (3.13)–(3.16) are interface conditions, not boundary conditions.

As described above, interface conditions follow from the differential equation in their integral form. In contrast, boundary conditions can be applied at the boundary domains for which a partial differential equation is solved, and do not follow from the integral representation of the differential equation. This is also the reason why the interface conditions are specified only for the electromagnetic fields, and not for the dynamical axion field $\delta\Theta$. In this section we only consider the case of a TMI surrounded by a non-topological material/vacuum with $\Theta^0 = 0$. We then only need to impose interface conditions for the electromagnetic fields; while they exist in both the TMI and the adjacent region, the dynamical AQ only exists in the TMI. The AQ is therefore only subject to boundary conditions. We revisit and deepen this discussion in section 3.2, in the context of calculating reflection and transmission coefficients for a layer of TMI surrounded by vacuum.

3.1.2 One dimensional model

To develop a one-dimensional model, we assume that all fields only depend on the z-coordinate and time. Furthermore, all fields are taken to be transverse fields, i.e. $B_z = H_z = D_z = E_z = 0$. Then, in a domain with constant Θ^0, eqs. (3.1)–(3.5) reduce to:

$$\partial_z \begin{pmatrix} -H_y \\ H_x \end{pmatrix} - \partial_t \begin{pmatrix} D_x \\ D_y \end{pmatrix} - \boldsymbol{J}_f = \frac{\alpha}{\pi}\left[\begin{pmatrix} B_x \\ B_y \end{pmatrix} \partial_t \delta\Theta + \begin{pmatrix} -E_y \\ E_x \end{pmatrix} \partial_z \delta\Theta \right], \tag{3.17}$$

$$\partial_z \begin{pmatrix} -E_y \\ E_x \end{pmatrix} + \partial_t \begin{pmatrix} B_x \\ B_y \end{pmatrix} = 0\,, \tag{3.18}$$

$$\partial_t^2 \delta\Theta - v_z^2 \partial_z^2 \delta\Theta + m_\Theta^2 \delta\Theta = \Lambda(E_x B_x + E_y B_y)\,, \tag{3.19}$$

where we assumed that no free static charges exist, i.e. $\rho_f = 0$.[4] The interface conditions (3.14) and (3.15) are trivially fulfilled in the one-dimensional model since the z-components of all electromagnetic fields vanish, and $\boldsymbol{n} = \hat{\boldsymbol{e}}_z$.

3.1.3 Linearization

The sources in eqs. (3.17) and (3.19) are non-linear and, therefore, finding analytic solutions is in general not possible. However, we are interested in the special case of solving the equations

[4] This does not mean that $\boldsymbol{J}_f$ vanishes. Since ρ_f and $\boldsymbol{J}_f$ are connected via a continuity equation, $\boldsymbol{J}_f$ only has to fulfil $\nabla \cdot \boldsymbol{J}_f = 0$ if $\rho_f = 0$.

JCAP08(2021)066

in presence of a strong, static external B-field $\boldsymbol{B}_e = B_e \hat{\boldsymbol{e}}_y$. We may therefore separate the total B-field into a static and a dynamical part, i.e. $\boldsymbol{B} \to \boldsymbol{B}_e + \boldsymbol{B}(\boldsymbol{x}, t)$. Similarly, the free current $\boldsymbol{J}_f$ can be split into a part which sources $\boldsymbol{B}_e$, and an additional reaction current, i.e. $\boldsymbol{J}_f \to \boldsymbol{J}_{f0} + \boldsymbol{J}_f$. Physically, the reaction current describes losses of the electromagnetic fields in the materials. Note that $\boldsymbol{B}_e$ fulfils $\nabla \times \boldsymbol{H}_e = \boldsymbol{J}_{f0}$, and $\boldsymbol{J}_{f0}$ satisfies the continuity equation $\nabla \cdot \boldsymbol{J}_{f0} = 0$. With these assumptions the resulting equations are:

$$\partial_z \begin{pmatrix} -H_y \\ H_x \end{pmatrix} - \partial_t \begin{pmatrix} D_x \\ D_y \end{pmatrix} - \sigma \begin{pmatrix} E_x \\ E_y \end{pmatrix} = \frac{\alpha}{\pi} \left[\begin{pmatrix} B_x \\ B_e \end{pmatrix} \partial_t \delta\Theta + \begin{pmatrix} -E_y \\ E_x \end{pmatrix} \partial_z \delta\Theta \right], \tag{3.20}$$

$$\partial_z \begin{pmatrix} -E_y \\ E_x \end{pmatrix} + \partial_t \begin{pmatrix} B_x \\ B_y \end{pmatrix} = 0\,, \tag{3.21}$$

$$\partial_t^2 \delta\Theta - v_z^2 \partial_z^2 \delta\Theta + m^2 \delta\Theta = \Lambda(E_x B_x + E_y B_e)\,, \tag{3.22}$$

where we substitute the reaction current $\boldsymbol{J}_f$ with the loss term $\sigma \boldsymbol{E}$ (Ohm's law). When deriving eqs. (3.20) and (3.22), we used that the external field B_e is much larger than the y-component of the reaction B-field, B_y. Note that it is straightforward to include an external source field in $\boldsymbol{E}$ and $\boldsymbol{B}$.

Let us now justify why the non-linear terms on the right-hand side in eqs. (3.20) and (3.22) can be linearized. Consider the two distinct cases where a strong external laser field is parallel or orthogonal to the static external B-field: first, assume that the external laser field is parallel to $\boldsymbol{B}_e = B_e \hat{\boldsymbol{e}}_y$. Note that

$$B_e \frac{\partial_t \delta\Theta}{\partial_z \delta\Theta} \approx 3 \times 10^4 \, \frac{\mathrm{V}}{\mathrm{m}} \left(\frac{B_e}{1\,\mathrm{T}} \right), \tag{3.23}$$

where we approximated $\frac{\partial_t \delta\Theta}{\partial_z \delta\Theta}$ with a typical spin wave velocity, which is on the order of $v_s = 10^{-4}$ [52]. Typical THz sources have a power around $P = 10^{-5}\,\mathrm{W}$, which leads to $E_y = 27\,\frac{\mathrm{V}}{\mathrm{m}}$ for a beam surface area of $10\,\mathrm{mm}^2$. Equation (3.23) is therefore fulfilled for sufficiently large external B-fields. With these considerations we see directly that $B_e \partial_t \delta\Theta \gg \partial_z \delta\Theta E_x$ since E_x is even smaller than E_y. It follows that the non-linear term in the second component on the right-hand side in eq. (3.20) can be neglected.

Next, we consider the two source terms in the first equation in the reft-hand side of eq. (3.20). The term $E_y \partial_z \delta\Theta$ dominates over the term $B_x \partial_t \delta\Theta$ since E_y contains the external laser source. However, the large source term $B_e \partial_t \delta\Theta$ in the term in eq. (3.20) is larger than the dominating source in the first term: $B_e \partial_t \delta\Theta \gg E_y \partial_z \delta\Theta$, cf. eq. (3.23). From eq. (3.21) it is clear that $\partial_t B_y = -\partial_z E_x$ and therefore due to $H_y \sim B_y$ the source of the first component in (3.20) sources the E_y-component. Therefore we can ignore the non-linear sources in the first equation in (3.20) and focus only on the E_y-component, e.g. the large linear source in the second equation in (3.20). The non-linear term $E_x B_x$ in eq. (3.22) can also be neglected since it is much smaller than the term $E_y B_e$, which includes two external fields.

Second, in the case that the external laser field is orthogonal to $\boldsymbol{B}_e = B_e \hat{\boldsymbol{e}}_y$, the dominating source of the Klein-Gordon equation, cf. eq. (3.22) is the linear term $E_y B_e$. Note that the fields B_x and E_y can only be induced by polarization rotation and are both on the order of $\frac{\alpha}{\pi}$. However, since $3 \times 10^8 \, \frac{\mathrm{V}}{\mathrm{m}} \left(\frac{B_e}{1\,\mathrm{T}} \right) \gg E_x$, we can linearize the source term of the Klein-Gordon, cf. eq. (3.22), i.e. $E_x B_x \ll E_y B_e$. The second component of eq. (3.20) can be linearized because any available THz lasers has an amplitude that is below the limit in eq. (3.23). The first component of eq. (3.20) can also be linearized, i.e. the source terms are

JCAP08(2021)066

neglected since both source terms include electromagnetic fields that are only generated via polarization rotation.

In summary, whether an external laser E-field is parallel or orthogonal to $\boldsymbol{B}_e$, the equations can be linearized, and they reduce to:

$$\partial_z^2 E_x - n^2 \partial_t^2 E_x - \mu\sigma\partial_t E_x = 0\,, \tag{3.24}$$

$$\partial_z^2 E_y - n^2 \partial_t^2 E_y - \mu\sigma\partial_t E_y = \frac{\alpha}{\pi}\mu B_e \partial_t^2 \delta\Theta\,, \tag{3.25}$$

$$\partial_t^2 \delta\Theta - v_z^2 \partial_z^2 \delta\Theta + m_\Theta^2 \delta\Theta = \Lambda E_y B_e\,, \tag{3.26}$$

where we explicitly use the linear constitutive relations, cf. eq. (3.6). Furthermore the refractive index is given by

$$n^2 = \epsilon\,\mu\,. \tag{3.27}$$

The material properties μ, ϵ, m_Θ, σ, Θ^0, v_z, and Λ are constants in the equations of motion. Regions with different material properties are linked by using interface conditions for the fields.

The corresponding interface conditions are given in eqs. (3.13) and (3.16) with $\boldsymbol{n} = \hat{\boldsymbol{e}}_z$. Equation (3.13) remains unchanged after linearization, while the definition of $\boldsymbol{H}_\Theta$ in eq. (3.16) changes due to the linearization to $\boldsymbol{H}_\Theta = \boldsymbol{H} + \frac{\alpha}{\pi}\Theta^0 \boldsymbol{E}$.

3.1.4 Losses

Losses can appear in the linearized equations of motion (3.24)–(3.26) in case of a finite conductivity σ. However, magnon losses, and losses that mix between magnons and photons, are not included. We now generalize eqs. (3.24)–(3.26) to include all possible types of losses. The equations then read:

$$\mathbf{K}\partial_t^2 \boldsymbol{X} - \boldsymbol{\Gamma}\partial_t \boldsymbol{X} + \mathbf{M}\boldsymbol{X} = 0\,, \tag{3.28}$$

where we define

$$\boldsymbol{X} = \begin{pmatrix} E_x \\ E_y \\ \delta\Theta \end{pmatrix}\,,\quad \mathbf{K} = \begin{pmatrix} 1 & 0 & 0 \\ 0 & 1 & \frac{\alpha}{\pi}\frac{B_e}{\epsilon} \\ 0 & 0 & 1 \end{pmatrix}\,,\quad \boldsymbol{\Gamma} = \begin{pmatrix} \Gamma_\rho & 0 & 0 \\ 0 & \Gamma_\rho & \Gamma_{\times,1} \\ 0 & \Gamma_{\times,2} & \Gamma_m \end{pmatrix}\,,$$

$$\mathbf{M} = \begin{pmatrix} \frac{k^2}{n^2} & 0 & 0 \\ 0 & \frac{k^2}{n^2} & 0 \\ 0 & -\Lambda B_e & v_z^2 k^2 + m_\Theta^2 \end{pmatrix}\,, \tag{3.29}$$

and where $\Gamma_\rho = \sigma/\epsilon$ is the photon loss, Γ_m is the equivalent loss for magnons, and $\Gamma_{\times,1/2}$ are mixed losses that can arise when photons and magnons interact. We retain these for the most general treatment, and set them to zero later. Note that not all Γs have the same mass dimension since $[\Gamma_\rho] = [\Gamma_m] = 1$, while $[\Gamma_{\times,1}] = 3$ and $[\Gamma_{\times,2}] = -1$. The approach also gives the possibility to define different refractive indices n and photon losses Γ_ρ for the E_x and E_y components. However, these effects can only become important when polarization rotation effects are discussed in detail. In the following, polarization rotation effect are computed, however they are not discussed at a level of detail, such that including different refractive indices for different polarizations would not change the results significantly.

The interface conditions (3.13)–(3.16) remain the same in the presence of losses, because it is assumed that all losses are bulk losses.

JCAP08(2021)066

3.2 Transmission and reflection coefficients

The presence of an AQ leads to a gap in the dispersion relation, which does not include any propagating modes. Based on this, Li et al. [42] proposed a transmission measurement (cf. figure 6) to determine the band gap in a TMI polariton spectrum, opened by the presence of the AQ (cf. figure 7). We now compute the transmission and reflection coefficients, and we demonstrate how to experimentally determine the parameters of interest — in particular the relevant terms of the loss matrix $\mathbf{\Gamma}$.

3.2.1 Solution of linearized equations

Our strategy for solving the linearized equations is as follows: we solve the equations for each spatial domain of constant material properties. We then apply the appropriate interface conditions to match the solutions in the different domains.

Lossless case ($\mathbf{\Gamma = 0}$). The dispersion relation for the E_x-component, see eq. (3.24), is the usual photon dispersion relation:

$$k^2 = n^2\omega^2 \equiv k_p^2 \,. \tag{3.30}$$

The E_y-component mixes with the AQ and, in the $v_z = 0$ case, we find a typical polariton dispersion [42, 125]:

$$\omega_\pm^2 = \frac{1}{2}\left[\omega_{\mathrm{LO}}^2 + \frac{k^2}{n^2}\right] \pm \frac{1}{2}\left[\left(\omega_{\mathrm{LO}}^2 - \frac{k^2}{n^2}\right)^2 + 4b^2\frac{k^2}{n^2}\right]^{1/2} , \tag{3.31}$$

where we have defined

$$b^2 \equiv \frac{\alpha}{\pi}\frac{\Lambda B_e^2}{\epsilon}, \tag{3.32}$$

$$\omega_{\mathrm{LO}}^2 \equiv b^2 + m_\Theta^2 \,. \tag{3.33}$$

The case $v_z \neq 0$ is discussed later since v_z is on the order of the spin wave velocity 10^{-4} and therefore the expected effect is small.

We show $\omega_\pm$ as a function of the wave number k in the left panel of figure 7. The horizontal black lines indicate the gap between m_Θ and ω_{LO}, where total reflection is expected. The resulting frequencies for m_Θ and ω_{LO} are in the THz regime what makes clear why THz sources are needed to probe the gap in the dispersion relation. ω_+ converges for large k to a photon dispersion (dashed blue line). ω_- has for small k an almost photon-like dispersion $\omega_- = \frac{k}{n}\frac{m}{\sqrt{b^2+m^2}}$ (dashed red line).

Inverting eq. (3.31) gives:

$$k^2 = n^2\omega^2\left[1 - \frac{b^2}{\omega^2 - m_\Theta^2}\right] \equiv k_\Theta^2 \equiv n_\Theta^2\omega^2 \,. \tag{3.34}$$

We show k as a function of ω in the right panel of figure 7. In the limit of $b \to 0$, eq. (3.34) becomes the usual photon dispersion relation. For ω^2 we have two solutions, while the solution for k^2 can be described by a single function. Inside the bandgap, k^2 is negative, thus k is purely imaginary, and no propagating mode is present. In the following section it is explicitly shown that this leads to total reflection and zero transmission.

JCAP08(2021)066

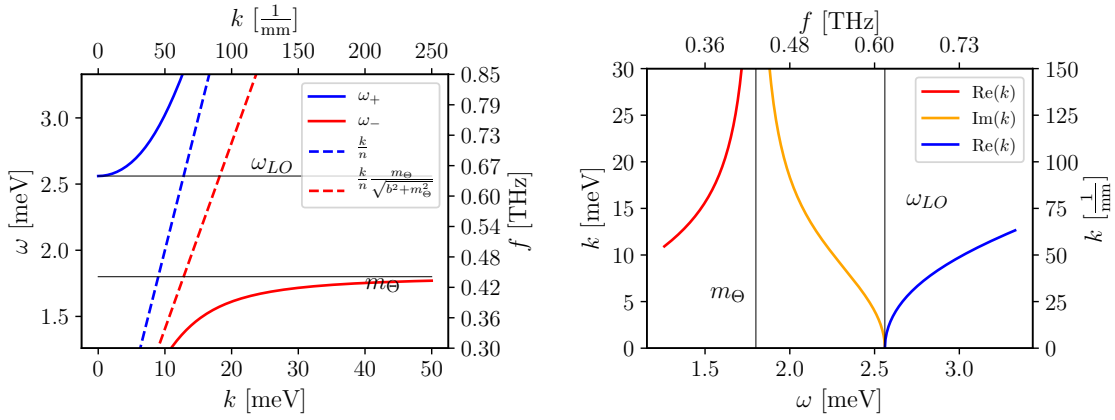

Figure 7. Polariton dispersion relation, arising from the mixing of AQs and photons for a spin wave velocity $v_z = 0$. We use typical material values for a $Mn_2Bi_2Te_5$ TMI, cf. table 5 and eq. (2.3), and $n = 5$ and $\mu = 1$. The external B-field is $B_e = 2\,\mathrm{T}$. The left panel shows the $\omega_\pm$ mode, which has a bandgap between m_Θ and ω_{LO} (horizontal lines). The right panel illustrates the inverse of the dispersion relation for k. Inside the bandgap (vertical lines), k is only imaginary, and hence no propagating modes exist.

The most general ansatz for the field evolution in a TMI medium are

$$E_x(z) = \hat{E}_x^+ e^{ik_p z} + \hat{E}_x^- e^{-ik_p z}\,, \tag{3.35}$$

$$E_y(z) = \hat{E}_y^+ e^{ik_\Theta z} + \hat{E}_y^- e^{-ik_\Theta z}\,, \tag{3.36}$$

$$\delta\Theta(z) = \delta\hat{\Theta}^+ e^{ik_\Theta z} + \delta\hat{\Theta}^- e^{-ik_\Theta z}\,, \tag{3.37}$$

where we omitted the time dependence $e^{-i\omega t}$ in each line. After plugging the solutions into the equations of motion, cf. eq. (3.28) the following relations are obtained:

$$\delta\hat{\Theta}^\pm = \Theta_E \hat{E}_y^\pm\,, \quad \Theta_E = \frac{\Lambda B_e}{m_\Theta^2 - \omega^2}\,, \tag{3.38}$$

or, equivalently,

$$\hat{E}_y^\pm = E_\Theta \delta\hat{\Theta}^\pm\,, \quad E_\Theta = -\frac{\alpha}{\pi}\frac{\mu\omega^2 B_e}{k_p^2 - k_\Theta^2}\,. \tag{3.39}$$

In the following, the relations in eq. (3.38) are used to reduce the number of unknowns in the ansatz (3.37):

$$\delta\Theta(z) = \Theta_E \hat{E}_y^+ e^{ik_\Theta z} + \Theta_E \hat{E}_y^- e^{-ik_\Theta z}. \tag{3.40}$$

The remaining constants $\hat{E}_y^\pm$ can be determined by using the interface conditions (explicitly shown in section 3.2.2). The AQ field $\delta\Theta$ is completely determined, cf. eq. (3.40), and no boundary conditions for $\delta\Theta$ have to be applied when, for example, a layer of TMI surrounded by vacuum is considered. It will become clear in the following that this is a consequence of the $v_z = 0$ limit.

Note that the relations in eq. (3.39) could have also been used to reduce the constants in eq. (3.36). However, a short calculation reveals that this would result in the same outcome, regardless whether the relations in eq. (3.38) or (3.39) was used to reduce the constants.

JCAP08(2021)066

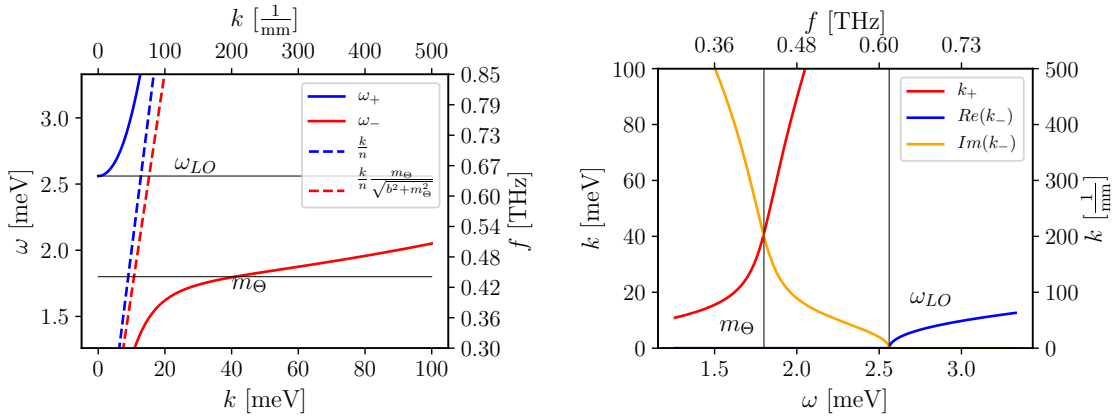

Figure 8. Dispersion relation for a non-zero spin wave velocity of $v_z = 0.01$. This exaggerated value was chosen because for realistic value of 10^{-4} the effect of band crossing of the + mode is not visible. We use typical material values for a $Mn_2Bi_2Te_5$ TMI, cf. table 5 and eq. (2.3), and $n = 5$ and $\mu = 1$. The external B-field is $B_e = 2\,\mathrm{T}$.

A finite spin wave velocity, $v_z \neq 0$, leads a slightly modified dispersion relation:

$$\omega_\pm^2 = \frac{1}{2}\Big[\omega_{\mathrm{LO}}^2 + k^2(v_z^2 + \frac{1}{n^2})\Big] \pm \frac{1}{2}\Big[(\omega_{\mathrm{LO}}^2 + k^2(v_z^2 - \frac{1}{n^2}))^2 + 4b^2\frac{k^2}{n^2}\Big]^{1/2}. \tag{3.41}$$

Equation (3.41) is not a typical polariton dispersion relation, since the sign of v_z under the square root is positive, not negative. The dispersion relation for $\omega_\pm$ from eq. (3.41) is shown in the left panel of figure 8, where we used an unrealistically large vale of $v_z = 0.01$ for illustrative purposes. Typical values for v_z are on the order of 10^{-4}. A non-zero value of v_z leads to a gap-crossing of the ω_- mode. However, due to the smallness of the spin wave velocity compared to the speed of light, the gap crossing happens at large values of the wave number k.

Inverting eq. (3.41) yields two modes for k^2,

$$k_\pm^2 = \frac{1}{2v_z^2}\left[\omega^2 - m_\Theta^2 + n^2\omega^2 v_z^2 \pm \left(\left(m_\Theta^2 + \omega^2(n^2v_z^2 - 1)\right)^2 + 4\omega^2 n^2 b^2 v_z^2\right)^{1/2}\right], \tag{3.42}$$

whereas we only obtained one mode for k^2 in the $v_z = 0$ case, cf. eq. (3.34). The functional dependence of eq. (3.42) is shown in the right panel of figure 8. The imaginary part of the k_- mode, which for $v_z = 0$ was only present inside the gap, now keeps rising outside of the gap for frequencies $\omega < m_\Theta$. The k_+ mode crosses the gap such that for $\omega > \omega_{\mathrm{LO}}$ two propagating modes exist. However the wavelength of the k_+ mode is always much shorter than the wavelength of the k_- mode.

The most general ansatz in the case of non-vanishing spin wave velocity is:

$$E_x(z) = \hat{E}_x^+ e^{ik_p z} + \hat{E}_x^- e^{-ik_p z}, \tag{3.43}$$

$$E_y(z) = \hat{E}_y^{++} e^{ik_+ z} + \hat{E}_y^{+-} e^{-ik_+ z} + \hat{E}_y^{-+} e^{ik_- z} + \hat{E}_y^{--} e^{-ik_- z}, \tag{3.44}$$

$$\delta\Theta(z) = \delta\hat{\Theta}^{++} e^{ik_+ z} + \delta\hat{\Theta}^{+-} e^{-ik_+ z} + \delta\hat{\Theta}^{-+} e^{ik_- z} + \delta\hat{\Theta}^{--} e^{-ik_- z}. \tag{3.45}$$

Relations for the unknown constants in the ansatz (3.43)–(3.45) can be derived in complete analogy to the $v_z = 0$ case. However, we would now need to specify boundary conditions

JCAP08(2021)066

for the dynamical axion in order to determine all constants. We do not perform the explicit calculation here since we expect the difference to the $v_z = 0$ case to be minimal, thanks to the smallness of the spin wave velocity. To see this, consider the following argument:

Let an incoming electromagnetic wave in vacuum be described by $A_0 e^{ik_p z}$. In the TMI material with $v_z \neq 0$, two modes are present. Around $\omega \sim \omega_{\mathrm{LO}}$, the first mode k_s has a wavelength that is much shorter than k_p, while the second mode k_l has a much longer wavelength than k_p, i.e. $|k_s| \gg |k_p| \gg |k_l|$. This is exactly the situation that we face (cf. figure 8), where $k_s = k_+$ and $k_l = k_-$.[5] Neglecting reflections, the fraction of the amplitudes of the two modes in medium 1 are $\left|\frac{A_1^l}{A_1^s}\right| = \left|\frac{k_a - k_p}{k_p - k_l}\right| \approx \left|\frac{k_s}{k_p}\right| \gg 1$, where the index 1 refers to medium 1. Therefore the amplitude of long wavelength mode A_1^l is much larger than the amplitude of the short wavelength mode A_1^s. Based on these arguments, the contribution of the k_+ mode can therefore be neglected — even though it is in principle present. In what follows, we will consequently assume that $v_z = 0$.

Case with losses ($\boldsymbol{\Gamma \neq 0}$). If material losses are included, the dispersion relations (3.30) and (3.34) are modified. The dispersion relation of the E_x-component is

$$k^2 = n^2 \omega^2 \left(1 + i\frac{\Gamma_\rho}{\omega}\right) =: k_p^2 \tag{3.46}$$

and the dispersion relation for the mixed system of E_y and $\delta\Theta$ is

$$\begin{aligned} k_\Theta^2 \equiv k^2 = n^2\omega^2 &\left(1 + \frac{b^2}{-i\Gamma_m\omega + m_\Theta^2 - \omega^2} + i\frac{\Gamma_\rho}{\omega}\right) \\ &+ n^2\omega \left(\frac{iB_e\left(\frac{\alpha}{\pi}\frac{\Gamma_{\times,2}\omega^2}{\epsilon} + \Lambda\Gamma_{\times,1}\right) - \omega\Gamma_{\times,1}\Gamma_{\times,2}}{-i\Gamma_m\omega + m_\Theta^2 - \omega^2}\right). \end{aligned} \tag{3.47}$$

The first part of the dispersion relation in eq. (3.47) only includes the diagonal losses Γ_m and Γ_ρ, while the second part also includes mixed losses. We argued in section 2.5 that mixed losses are smaller than the diagonal losses Γ_ρ and Γ_m. We therefore neglect mixed losses in what follows.

Rewriting the dispersion relation (3.47) without mixed losses gives:

$$\boxed{k_\Theta^2 \equiv k^2 = n^2\omega^2 \left(1 + \frac{(m^2 - \omega^2)\omega b^2}{\Gamma_m^2\omega^2 + (m_\Theta^2 - \omega^2)^2} + i\,\frac{\Gamma_m\omega b^2}{\Gamma_m^2\omega^2 + (m_\Theta^2 - \omega^2)^2} + i\,\frac{\Gamma_\rho}{\omega}\right).} \tag{3.48}$$

Equation (3.48) shows that the Γ_ρ contribution is unaffected by any other material properties, and it stays approximately constant when ω does not vary too much. We show an example for $\Gamma_m = 0$ in the left panel of figure 9. While the peak of the resonance is not affected much by the losses, Γ_ρ introduces an almost constant imaginary for all frequencies. In contrast, magnon losses Γ_m are dominant around m_Θ. This can be seen from the third term in eq. (3.48) which represents a Lorentzian curve that peaks around $\omega = m_\Theta$ and has a full width at half maximum (FWHM) of Γ_m. In the middle and right panels of figure 9 we show examples for $\Gamma_\rho = 0$. The larger Γ_m, the larger the FWHM of the imaginary part

[5] Note that due to the fact that we plot k_+ only up to 100 meV, the much larger values of k_+ around ω_{LO} are not visible in the right panel of figure 8.

JCAP08(2021)066

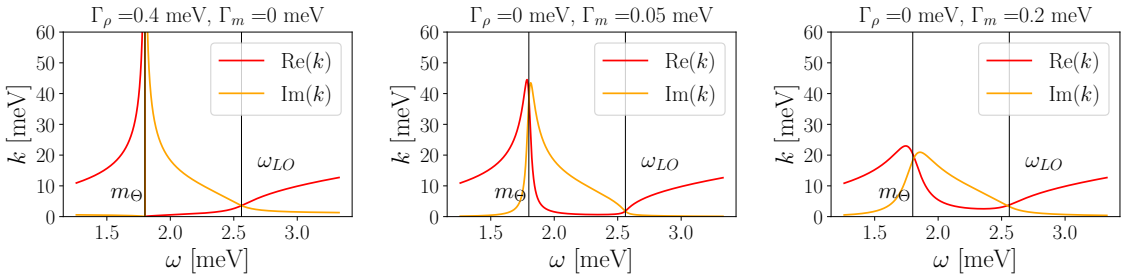

Figure 9. Dispersion relation of the axion-polariton for magnon and photon losses, Γ_m and Γ_ρ. Mixed losses are neglected. *Left:* $\Gamma_\rho = 0.4\,\text{meV}$ and $\Gamma_m = 0$. Photon losses introduce an almost constant imaginary part to the dispersion relation if the chosen frequency interval is not too large. *Middle:* $\Gamma_\rho = 0$ and $\Gamma_m = 0.05\,\text{meV}$, *right:* $\Gamma_\rho = 0$ and $\Gamma_m = 0.2\,\text{meV}$. The larger the magnon loss, the larger the FWHM of the imaginary part in the dispersion relation. We use typical material values for a $Mn_2Bi_2Te_5$ TMI, cf. table 5 and eq. (2.3), and $n = 5$ and $\mu = 1$. The external B-field is $B_e = 2\,\text{T}$.

in the dispersion relation. In other words, frequencies away from the gap are damped more strongly when Γ_m is large. Furthermore, the resonance becomes less pronounced for large Γ_m. As a consequence, it will be difficult to confirm the existence of the gap in the spectrum, and the presence of a dynamical AQ, when large losses are present. We investigate this more quantitatively in section 3.2.3, where we calculate the reflection and transmission coefficients for a single TMI layer.

In the presence of losses the most general solution, cf. eq. (3.35)–(3.37), is still valid. However, the relations in the eqs. (3.38) and (3.39) are modified:

$$\delta\hat{\Theta}^\pm = \Theta_E \hat{E}^\pm\,, \quad \Theta_E = \frac{\Lambda B_e + i\omega\Gamma_{\times,2}}{-\omega^2 + m_\Theta^2 - i\omega\Gamma_m}\,, \tag{3.49}$$

or, equivalently,

$$\hat{E}_y^\pm = E_\Theta \delta\hat{\Theta}^\pm\,, \quad E_\Theta = \frac{\alpha}{\pi}\frac{\omega^2\mu B_e + in^2\omega\Gamma_{\times,1}}{k_\Theta^2 - k_p^2}\,. \tag{3.50}$$

It can be checked that eqs. (3.49) and (3.50) reduce to eqs. (3.38) and (3.39) in the limit of $\boldsymbol{\Gamma} \to 0$. In complete analogy to the case without losses, eq. (3.49) determines the dynamical AQ field, cf. eq. (3.40).

3.2.2 Matrix formalism for many interfaces

In the previous section, we discussed the solutions of the one-dimensional axion-Maxwell equations in a homogeneous TMI. Here, we consider $N+1$ media, separated by N interfaces, as shown in figure 10. Let the first interface be located at $z_0 = z_1$, and the last interface at z_N. We label each medium with an index r, i.e. $r = 0, \ldots, N$. For example, the permittivity and permeability of medium r are thus denoted by μ_r and ϵ_r, respectively. Recall that, in all media, we set $v_z = 0$ and define the constant external B-field to be $\boldsymbol{B}_e = B_e\,\hat{\boldsymbol{e}}_y$.

We now develop a matrix formalism to link the solutions in different materials to each other. This makes it possible to compute the scattering of incoming electromagnetic radiation from a multilayer system. The simplest application is the computation of the reflection and transmission coefficients for THz radiation that hits a layer of TMI; we discuss this case at the end of this section.

JCAP08(2021)066

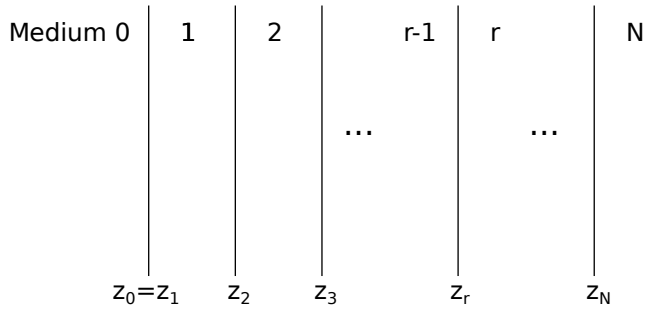

Figure 10. Multilayer system of different materials. Each medium is characterized by ϵ_r, μ_r, $\mathbf{\Gamma}_r$, and Θ_r^0. The external B-field has the same strength and polarization in each medium.

The most general ansatz in medium r is given by:

$$\begin{aligned} E_x^r &= \hat{E}_{x,r}^+ e^{ik_p^r(z-z_r)} + \hat{E}_{x,r}^- e^{-ik_p^r(z-z_r)}\,, \\ E_y^r &= \hat{E}_{y,r}^+ e^{ik_\Theta^r(z-z_r)} + \hat{E}_{y,r}^- e^{-ik_\Theta^i(z-z_r)}\,, \\ \delta\Theta^r &= \Theta_E^r \hat{E}_{y,r}^+ e^{ik_\Theta^r(z-z_r)} + \Theta_E^r \hat{E}_{y,r}^- e^{-ik_\Theta^r(z-z_r)}\,, \end{aligned} \tag{3.51}$$

where, compared to eqs. (3.35)–(3.37), we introduce different phase shifts z_r for each medium. The expressions for k_p, k_Θ, and E_Θ were derived already in eq. (3.30), (3.34), and (3.38) for the case $\mathbf{\Gamma} = 0$ and in eq. (3.46), (3.47), and (3.49), for the case $\mathbf{\Gamma} \neq 0$. Applying the interface conditions (3.13) and (3.16) for the electromagnetic fields at z_r yields the following system of equations:

$$\boldsymbol{t}_r = \mathbf{M}_r^{-1}\,\mathbf{M}_{r-1}\,\mathbf{P}_{r-1}\boldsymbol{t}_{r-1}\,, \tag{3.52}$$

with

$$\boldsymbol{t}_r = \begin{pmatrix} \hat{E}_{x,r}^+ \\ \hat{E}_{x,r}^- \\ \hat{E}_{y,r}^+ \\ \hat{E}_{y,r}^- \end{pmatrix}\,, \quad \mathbf{M}_r = \begin{pmatrix} 1 & 1 & 0 & 0 \\ 0 & 0 & 1 & 1 \\ \frac{k_p^r}{\omega\mu_r} & -\frac{k_p^r}{\omega\mu_r} & -\frac{\alpha}{\pi}\Theta_r^0 & -\frac{\alpha}{\pi}\Theta_r^0 \\ -\frac{\alpha}{\pi}\Theta_r^0 & -\frac{\alpha}{\pi}\Theta_r^0 & -\frac{k_\Theta^r}{\omega\mu_r} & \frac{k_\Theta^r}{\omega\mu_r} \end{pmatrix}\,, \tag{3.53}$$

and

$$\mathbf{P}_r = \mathrm{diag}\left(e^{i\Delta_r^p},\, e^{-i\Delta_r^p},\, e^{i\Delta_r^\Theta},\, e^{-i\Delta_r^\Theta}\right)\,. \tag{3.54}$$

The phases are defined as: $\Delta_r^\Theta \equiv k_\Theta^r(z_{r+1} - z_r)$ and $\Delta_r^p \equiv k_p^r(z_{r+1} - z_r)$.

Let us define the matrix $\mathbf{S}$ to relate the incoming field amplitude from medium 0 to the outgoing field amplitude in medium N:

$$\boldsymbol{t}_N = \mathbf{S}\,\boldsymbol{t}_0\,. \tag{3.55}$$

For instance, for a single interface, $\mathbf{S}$ is given by

$$\mathbf{S} = \mathbf{M}_1^{-1}\,\mathbf{M}_0\,\mathbf{P}_0 \tag{3.56}$$

and, for two interfaces, $\mathbf{S}$ is given by

$$\mathbf{S} = \mathbf{M}_2^{-1}\,\mathbf{M}_1\,\mathbf{P}_1\mathbf{M}_1^{-1}\,\mathbf{M}_0\,\mathbf{P}_0\,. \tag{3.57}$$

JCAP08(2021)066

Finally, for N interfaces, we find $\mathbf{S}$ to be given by

$$\mathbf{S} = \mathbf{M}_N^{-1}\,\mathbf{M}_{N-1}\,\mathbf{P}_{N-1}\,\mathbf{M}_{N-1}^{-1}\,\mathbf{M}_{N-1}\mathbf{P}_{N-2}\,\mathbf{M}_{N-2}\cdots\mathbf{M}_2^{-1}\,\mathbf{M}_1\,\mathbf{P}_1\mathbf{M}_1^{-1}\,\mathbf{M}_0\,\mathbf{P}_0\,. \tag{3.58}$$

For electromagnetic radiation coming into the system from medium 0, $\hat{E}^+_{x0}$ and $\hat{E}^+_{y,0}$ are known and $\hat{E}^-_{x,N} = \hat{E}^-_{y,N} = 0$. The other unknown field values can be determined from the elements of $\mathbf{S}$, i.e. S_{ij}, via

$$\begin{pmatrix} \hat{E}^+_{x,N} \\ \hat{E}^-_{x,0} \\ \hat{E}^+_{y,N} \\ \hat{E}^-_{y,0} \end{pmatrix} = \begin{pmatrix} -1 & S_{12} & 0 & S_{14} \\ 0 & S_{22} & 0 & S_{24} \\ 0 & S_{32} & -1 & S_{34} \\ 0 & S_{42} & 0 & S_{44} \end{pmatrix}^{-1} \cdot \begin{pmatrix} -S_{11}\hat{E}^+_{x0} - S_{13}\hat{E}^+_{y0} \\ -S_{21}\hat{E}^+_{x0} - S_{23}\hat{E}^+_{y0} \\ -S_{31}\hat{E}^+_{x0} - S_{33}\hat{E}^+_{y0} \\ -S_{41}\hat{E}^+_{x0} - S_{43}\hat{E}^+_{y0} \end{pmatrix}. \tag{3.59}$$

3.2.3 Layer of topological magnetic insulator

Let us now apply the matrix formalism to a system with $N = 2$. However, note that the matrix approach developed here is able to describe more complicated systems, consisting of many layers. One particular example could be a layered system of different topological insulators with different material properties. The matrix formalism with $N > 2$ could be useful in DM searches to increase the boost factor using additional layers of TMI or dielectric.

We now calculate the reflection and transmission coefficients for one TMI layer. In the language of the matrix formalism the system has $N = 2$ boundaries, and hence three media. Media 0 and 2 are vacuum while medium 1 is a TMI, hosting a dynamical AQ. The THz laser radiation is coming from medium 0 and hits the layer of TMI. In what follows, we omit the subscripts r that label the materials because the only non-vacuum medium is the TMI, i.e. medium 1.

We assume that the laser polarization is oriented in the y-direction, parallel to the external B-field. In this case, we obtain — to lowest order in $\frac{\alpha}{\pi}\Theta^0$ — the following reflection and transmission coefficients:

$$T_y = \frac{2i\tilde{k}}{\left(\tilde{k}^2+1\right)\sin\Delta + 2i\tilde{k}\cos\Delta} + \mathcal{O}\left(\left(\frac{\alpha}{\pi}\Theta^0\right)^2\right), \tag{3.60}$$

$$R_y = -\frac{\left(\tilde{k}^2-1\right)\sin\Delta}{\left(\tilde{k}^2+1\right)\sin\Delta + 2i\tilde{k}\cos\Delta} + \mathcal{O}\left(\left(\frac{\alpha}{\pi}\Theta^0\right)^2\right), \tag{3.61}$$

where $\tilde{k} = \frac{k_\Theta}{\omega\mu}$, $\Delta \equiv dk_\Theta$ and $d = z_2 - z_1$ is the thickness of the layer. Note that, although $\tilde{k}$ depends on the expansion parameter we did not expand $\tilde{k}$ because otherwise the expansion for the transmission and reflection coefficients would not be valid around the resonance. The calculated transmission and reflection coefficients are valid for both the case with and without losses since we assume all losses to be bulk losses. T_y and R_y agree with the normal transmission and reflection coefficients of a dielectric disk [47] if the coupling b of the AQ to the photon is set to zero, i.e. $k_\Theta \to n\omega$, corresponding to $f_\Theta \to \infty$.

We show the full functions for the reflection and transmission coefficients without losses ($\mathbf{\Gamma} = 0$) in figure 11. The coefficients are shown for different values of the laser frequency ω and sample thickness d. The left column assumes the presence of a dynamical AQ, while the figures in the right column show the case when no dynamical AQ is present. Note that in

JCAP08(2021)066

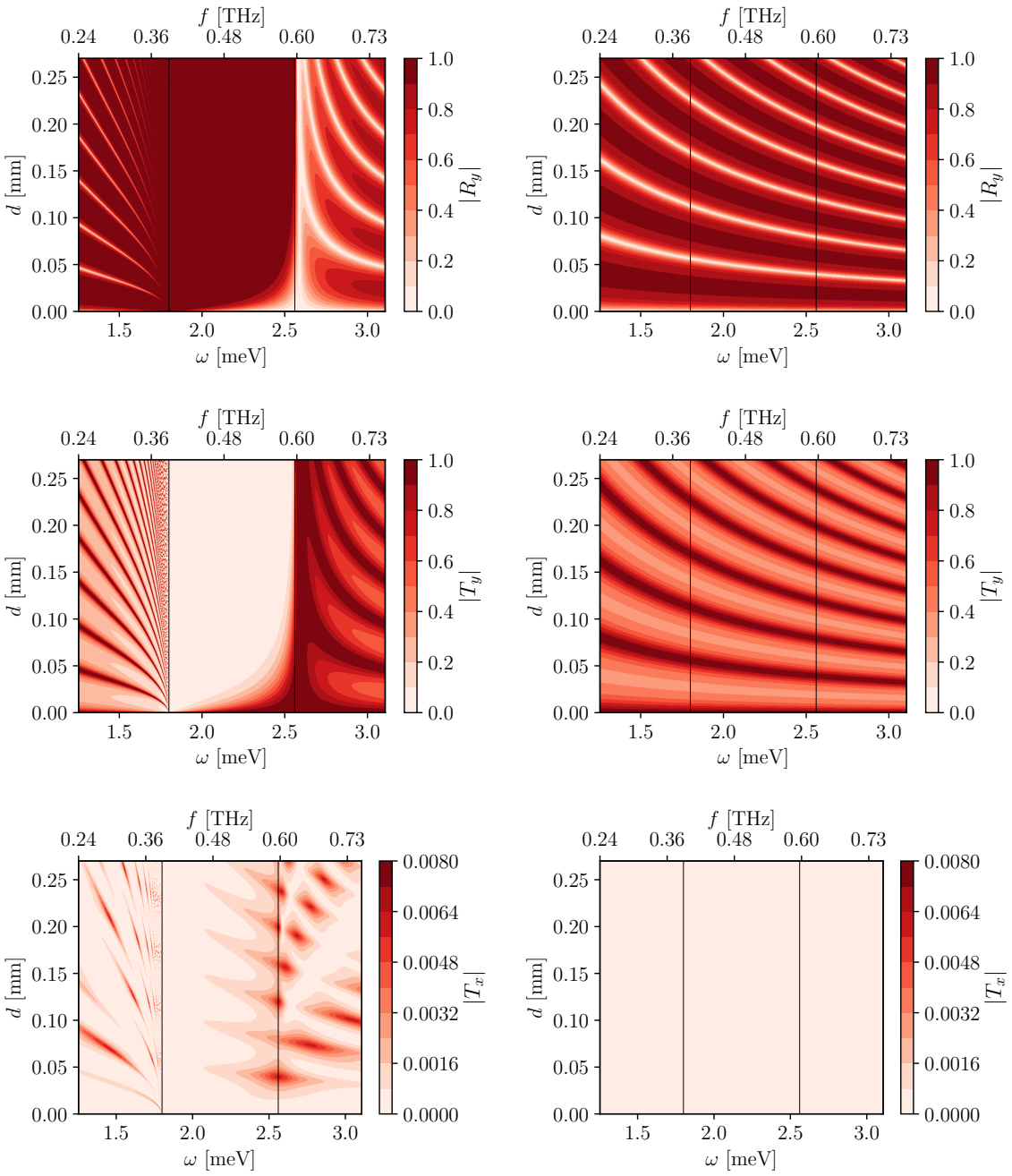

Figure 11. Reflection and transmission coefficients for a laser that hits a material with (*left*) and without (*right*) a dynamical AQ. The laser polarization is in the y-direction, parallel to the external B-field. The materials have $\Theta^0 = 0.8\,\pi$, $n = 5$, and $\mu = 1$. Typical material values for a $Mn_2Bi_2Te_5$ TMI with an external B-field B_e of 2 T are chosen, cf. table 5 and eq. (2.3). m_Θ and ω_{LO} are marked with the black vertical lines. The R_y (T_y) coefficient is always close to one (zero) inside the gap if a dynamical AQ is present. The T_x coefficient is only non-zero is a AQ is present. However the effect of an AQ in the E_x-component is much smaller than in the E_y-component since the E_x-component can only be induced via polarization rotation with non-zero Θ^0.

JCAP08(2021)066

both cases $\Theta^0 = 0.8\,\pi$ is assumed although the shown results for T_y and R_y do not depend on Θ^0 to lowest order, cf. equations (3.60) and (3.61).

First, we discuss the figures in the top and middle row, which show the reflection and transmission coefficients for the E_y-components. If a dynamical AQ is present, the dispersion relation k_Θ becomes imaginary between m_Θ and ω_{LO}. The gap between these two frequencies is marked with the two vertical lines. For large thicknesses d, all frequencies in the gap are reflected, and none are transmitted. This is a direct consequence of the purely imaginary k_Θ in the gap. For small values of the thickness, the gap size is reduced. This happens around ω_{LO}, i.e. the upper part of the gap, since the imaginary part gets reduced (the skin depth becomes larger) the more ω_{LO} is approached from smaller frequencies, cf. right panel of figure 7. When going away from the gap, the figures in the left and right columns agree more and more. This is as expected since the dispersion relation k_Θ differs only significantly from a normal photon dispersion around the gap. In the case of no dynamical AQ (left panel) we notice a clear non-zero reflection and transmission inside the gap. Comparing the figures on the left- and right-hand side, it is clear that the AQ causes an $\mathcal{O}(1)$ modification of the T_y and R_y coefficients compared to the spectrum when no dynamical AQ is present.

Next, we discuss the bottom row of figure 11, which shows the transmission coefficient for the E_x-component. If no dynamical AQ field is present (right panel) but we have a topological material with $\Theta^0 = 0.8\,\pi$, the transmission T_x vanishes. This may be surprising at fist glance because there is mixing at the interface of ordinary TIs and, hence, also a polarization rotation. However, the transmission in the x-component vanishes since the polarization rotations at the two interfaces cancel each other. If in addition to the static $\Theta^0 = 0.8\,\pi$ a dynamical AQ is present (left panel), we get a small non-zero transmission T_x. The signal is much smaller than in the case of the T_y coefficient. This is because the incoming laser is polarized in the E_y component and a non-zero E_x-component can only be induced due to a nonzero Θ^0, i.e. mixing at the interfaces, which is proportional to the small parameter $\frac{\alpha}{\pi}\Theta^0$. In conclusion, we should first look for the AQ by studying the E_y-component because the AQ modification of this component is much larger than for the E_x-component.

However, once the AQ is found, one can also use the E_x-component to determine, for example, Θ^0 of the material by reflection and transmission measurements. Is is also possible to study the influence of non-linear effects with the x-components. In eq. (3.20) it was shown that the laser sources the x-component in a non-linear fashion. This effect is neglected here because the equations are linearized.

Figure 12 shows the transmission coefficient T_y for different losses. The figures are produced for our benchmark material $Mn_2Bi_2Te_5$ with $n = 5, \mu = 1$ and $\Theta^0 = 0.8\,\pi$. In the top row we illustrate the influence of photon losses Γ_ρ for a TMI with a dynamical AQ (left panel) and for a normal TI (right panel). The transmission at large layer thicknesses becomes smaller independently of the resonance. This is due to the fact that Γ_ρ appears in the dispersion relation (3.48) as an additional term which is approximately constant in the small shown frequency interval. The skin depth is of the order of Γ_ρ^{-1}. It is therefore advantageous to have thin material samples for distinguishing between the case of a DA (left panel) and no DA (right panel). However, should not be too thin. For very small thicknesses the frequencies inside the gap lead to a transmission coefficient T_y that is not very small anymore. Note that the effect of losses for large d becomes more pronounced for larger refractive indices n.

In the bottom row of figure 12 photon losses are zero and the effect of magnon losses Γ_m is illustrated. We do not show the case without an AQ because without AQ there are no magnon losses and one should compare to the already existing figure 11 (middle row, right).

JCAP08(2021)066

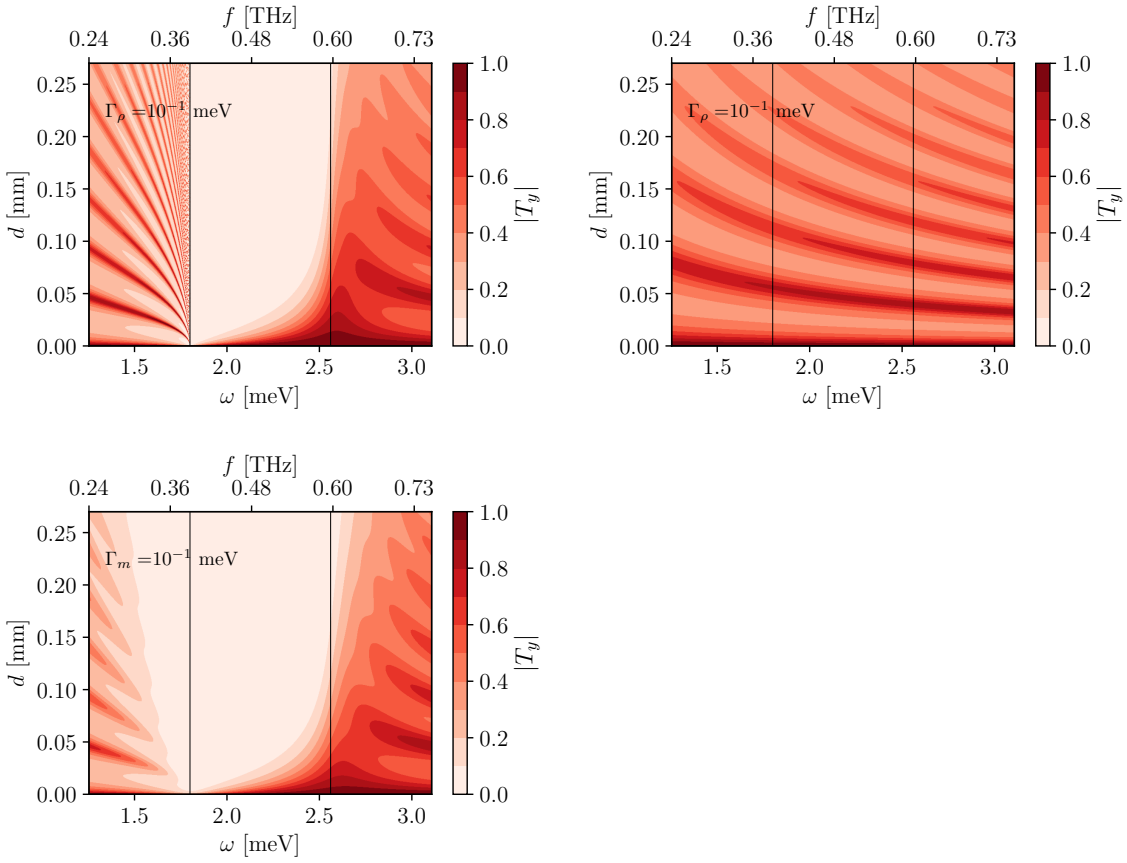

Figure 12. Transmission coefficients for the E_y-component (parallel to the external B-field) for exaggerated photon and magnon losses, Γ_ρ and Γ_m. We show the results for when a dynamical AQ field (*left*) and if no dynamical AQ is present; (*right*). In both cases we have $\Theta^0 = 0.8\,\pi$. We use typical material values for a $Mn_2Bi_2Te_5$ TMI, cf. table 5 and eq. (2.3), and $n = 5$ and $\mu = 1$. The external B-field is $B_e = 2\,\mathrm{T}$. m_Θ and ω_{LO} are marked with the black vertical lines.

The larger the magnon losses, the more pronounced is the widening of the gap. This can be understood by looking at the dispersion relation in eq. (3.48). Magnon losses Γ_m introduce a Lorentzian shaped imaginary part to the dispersion relation. The width of the Lorentzian is proportional to Γ_m. Due to the Lorentzian shape of the damping imaginary part in the dispersion relation also frequencies that are not directly in the gap — but close to the gap — can become highly damped. This effect becomes more pronounced the thicker the sample is.

From the previous discussion it becomes clear that finding the AQ will depend very sensitively on the losses and thickness of the material. The losses that we show in figure 12 are exaggerated and in reality we expect them to be much smaller. Therefore from figure 12 we find that with a layer thickness on the order of 0.03 mm and 0.3 mm AQ can be most effectively be detected.

Once the AQ is detected the characterization of the parameters of the TMI is of huge importance. In section 4 and 5 it is shown how a TMI can be used as dark matter axion detector. To estimate the induced photon signal from a DA, AQ and photon mixing the parameters of the TMI have to be known precisely. In the following we demonstrate that fitting measurements to the presented results can determine the parameters of the TMI.

JCAP08(2021)066

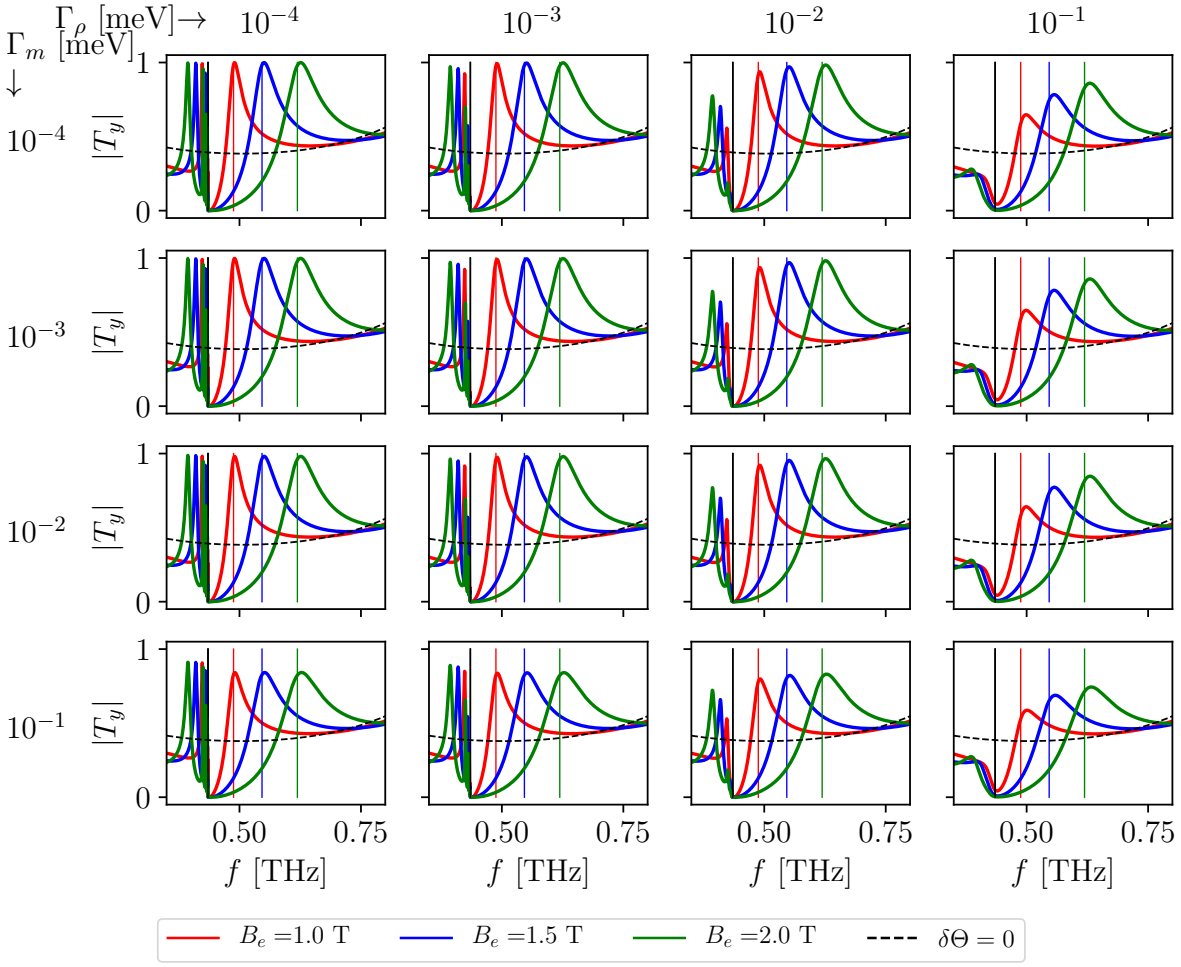

Figure 13. Transmission coefficient T_y for a layer of TMI with thickness $d = 0.03\,\text{mm}$ for different B-fields (colours) are shown. Panels vary the losses Γ_ρ (from left to right) and Γ_m (from top to bottom). The vertical black line indicates the value of $m_\Theta = 2\,\text{meV}$, while the other vertical lines indicate the value of ω_{LO} for different values of the external B-field. The larger the external B-field, the larger the gap between m_Θ and ω_{LO}. We use typical material values for a $Mn_2Bi_2Te_5$ TMI, cf. table 5 and eq. (2.3), and $n = 5$ and $\mu = 1$. The dashed black line shows the result when no dynamical AQ $\delta\Theta$ is present, while the solid coloured lines are for the case with a dynamical AQ.

In figure 13, photon losses Γ_ρ are varied between $\Gamma_\rho = 3 \times 10^{-4}\,\text{meV}$ and $0.3\,\text{meV}$, and magnon losses between $\Gamma_m = 3 \times 10^{-4}\,\text{meV}$ and $0.3\,\text{meV}$. The layer thickness is fixed to $d = 0.03\,\text{mm}$. In each figure, we show three different external B-field values. The values of m_Θ and ω_{LO} are marked with a vertical black and coloured lines, respectively. The weaker the external B-field, the smaller the gap.

Figure 13 makes again clear that the larger the losses the harder it is to distinguish the case where a dynamical AQ is present (solid coloured curves) from the case that not dynamical AQ (dashed black line) is present. For relatively small losses, the distinction between the curves is very clear. We therefore conclude that comparing these results to future measurements will make it possible to explicitly determine the material parameters, i.e. losses, refractive index, Θ^0, and the parameters that enter the AQ mass m_Θ and the gap size parameter b.

JCAP08(2021)066

We now investigate further the resonance around $\omega_{\rm LO}$, cf. figure 13. When the losses in figure 13 are small the resonance frequency $f_{\rm res} = \frac{\omega_{\rm res}}{2\pi}$ corresponds to $\omega_{\rm LO}$. However, with higher losses, the resonance frequency $\omega_{\rm res}$ moves to higher frequencies, i.e. $f_{\rm res} > \frac{\omega_{\rm LO}}{2\pi}$. With increasing losses, the resonance smears out until it vanishes completely. Figure 13 allows us to directly read off the amount of losses that would still be acceptable AQ detection (for a sample of thickness $d = 0.03\,\text{mm}$). The resonance peaks to the right of $\omega_{\rm LO}$ in figure 13 are not symmetric. We therefore define the width of the resonance peak, $\Gamma_{\rm res}$, as two times the frequency interval that ranges from the frequency at the transmission maximum down to the smaller frequency at half the transmission maximum.

The ratio $\frac{f_{\rm res}}{\Gamma_{\rm res}}$ is called the Q-factor. It describes the quality of the resonance in the sense that large Q-factors give rise to a well-defined resonance, whereas low Q-factors show that the resonance is highly damped. In figure 14, the Q-factor is shown with respect to the applied external B-field for different losses. We consider the case of dominant conductive losses (red) and dominant magnon losses (blue). The largest Q-factor is observed at small external B-field, and the low magnon losses lead to the largest Q. This is consistent with the intuition that at low B-field the polariton is largely magnon-like. For larger external B-fields the difference between the two cases becomes small, as both sources of loss contribute almost equally.

4 Axion dark matter and axion quasiparticles

4.1 Dark axion, axion quasiparticle and photon mixing

Paper I proposed using dynamical AQs in TMIs to detect DAs. This is possible since DAs can mix resonantly with axion polaritons. Compared to Paper I, we work out a more detailed calculation for the emitted photon signal by taking into account the correct interface conditions and material losses. This, in turn, allows us to present a more rigorous calculation of the sensitivity reach for DA searches using TMIs.

As a starting point, we use the three-dimensional equations of motion, eqs. (3.1)–(3.5). We linearize these and derive a one-dimensional model in analogy to section 3.1.3. In what follows, the one-dimensional model is used to derive the photon signal generated by DAs passing through a magnetized TMI that hosts dynamical AQs.

4.1.1 General formulation

To describe the threefold mixing between AQs, DAs, and photons, we need to add the Klein-Gordon equation for DAs, which is sourced by the electromagnetic fields, to eqs. (3.1)–(3.5). Additional source terms, arising due to the presence of DAs, have therefore to be added to eqs. (3.1) and (3.2). Doing so results in the following equations of motion:

$$\nabla \cdot \boldsymbol{D} = \rho_f - \frac{\alpha}{\pi}\nabla(\delta\Theta + \Theta^0)\cdot\boldsymbol{B} - g_{a\gamma}\nabla a\cdot\boldsymbol{B}\,, \tag{4.1}$$

$$\begin{aligned}\nabla\times\boldsymbol{H} - \partial_t\boldsymbol{D} = \boldsymbol{J}_f + \frac{\alpha}{\pi}\left[\boldsymbol{B}\partial_t(\delta\Theta+\Theta^0) - \boldsymbol{E}\times\nabla(\delta\Theta+\Theta^0)\right]\\ + g_{a\gamma}\left(\boldsymbol{B}\partial_t a - \boldsymbol{E}\times\nabla a\right),\end{aligned} \tag{4.2}$$

$$\nabla\cdot\boldsymbol{B} = 0\,, \tag{4.3}$$

$$\nabla\times\boldsymbol{E} + \partial_t\boldsymbol{B} = 0\,, \tag{4.4}$$

$$\partial_t^2\delta\Theta - v_i^2\partial_i^2\delta\Theta + m_\Theta^2\delta\Theta = \Lambda\,\boldsymbol{E}\cdot\boldsymbol{B}\,, \tag{4.5}$$

$$(\partial_t^2 - \nabla^2 + m_a^2)\,a = g_{a\gamma}\,\boldsymbol{E}\cdot\boldsymbol{B}\,, \tag{4.6}$$

JCAP08(2021)066

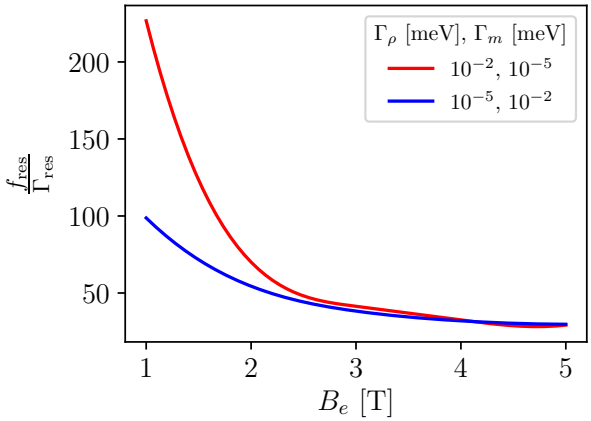

Figure 14. TMI Quality factor, $Q = f_{\rm res}/\Gamma_{\rm res}$, for different losses, with respect to the external B-fields. $f_{\rm res}$ is the frequency of the maximal transmission peaks around $\omega_{\rm LO}$, cf. figure 13. The TMI layer has a thickness of $d = 0.03\,\mathrm{mm}$.

where a is the pseudoscalar DA field, $g_{a\gamma}$ is the DA-photon coupling, and m_a is the DA mass, in addition to the other variables already defined in eqs. (3.1)–(3.5).

In section 3.1.1 we already noted that one cannot obtain interface conditions from the Klein-Gordon equation for an interface between media with and without AQs. However, DAs are expected to permeate any medium due to the necessarily feeble interactions of dark matter, and their presence in the Galaxy. Therefore, for two media that both contain DAs, eq. (4.6) can be used to derive an interface condition for the DA field.

Consider an infinitesimal volume element between two media, say, between medium 1 and medium 2. We integrate over this infinitesimal volume element and apply the divergence theorem. It follows that the normal derivative of the DA field between two interfaces has to be continuous,

$$\boldsymbol{n} \cdot (\nabla a_1 - \nabla a_2) = 0\,. \tag{4.7}$$

Furthermore, we require that the DA field be continuous over the interface:

$$a_1 - a_2 = 0\,. \tag{4.8}$$

We stress that the continuity of the axion field in eq. (4.8) does not follow from the axion-Maxwell equations, but is a reasonable approximation. In other words, as DAs only interacts with matter through very small couplings, and we are interested in the conversion of axions to photons again by a very small coupling, any modification due to the axion interacting with the interface is at higher order, and thus negligible.

4.1.2 Linearized one-dimensional model

Let us again assume the presence of a strong and static external B-field, $\boldsymbol{B}_e$. Without loss of generality, let $\boldsymbol{B}_e$ be polarized in the y-direction, i.e. $\boldsymbol{B}_e = B_e\,\hat{\boldsymbol{e}}_y$. Then, similar steps as in sections 3.1.2 and 3.1.3 lead to the following linearized equations of motion:

$$\left(\partial_z^2 - n^2\partial_t^2 - \sigma\mu\partial_t\right) E_y = \mu B_e \partial_t^2 \left(\frac{\alpha}{\pi}\delta\Theta + g_{a\gamma} a\right)\,, \tag{4.9}$$

$$\left(v_z^2\partial_z^2 - \partial_t^2 - m_\Theta^2\right)\delta\Theta = -\Lambda B_e E_y, \tag{4.10}$$

$$\left(\partial_z^2 - \partial_t^2 - m_a^2\right) a = -g_{a\gamma} B_e E_y\,. \tag{4.11}$$

JCAP08(2021)066

The photon signal in the E_x-component, induced by DAs, is always an order $\frac{\alpha}{\pi}\Theta^0$ smaller than the E_y-component. This is due to the fact that only the E_y-component mixes with DAs and AQs. The E_x-component can only be generated due to the mixing at the interface, which is proportional to $\frac{\alpha}{\pi}\Theta^0$. The main photon signal is therefore polarized parallel to the external B-field in experimental DA searches, i.e. in the E_y-component. Due to the suppression of the E_x-component, it will be even more challenging to detect a signal in the E_x-component. This justifies neglecting the E_x-component in what follows.

In addition to the linearization assumptions made in section 3.1.3, we further assume that the non-linear terms, which include the DA, can also be linearized. This assumption is justified because of the small coupling and non-relativistic nature of Galactic DAs, for which $\partial_t a/\partial_z a \approx 10^{-3}$.

The interface conditions for the electromagnetic fields after linearization are obtained with the linearized fields $\boldsymbol{D}_\Theta = \boldsymbol{D} + \frac{\alpha}{\pi}(\Theta^0 + \delta\Theta)\boldsymbol{B}_e$ and $\boldsymbol{H}_\Theta = \boldsymbol{H} - \frac{\alpha}{\pi}\Theta^0\boldsymbol{E}$. In the one-dimensional model, the conditions $\boldsymbol{n}\cdot(\boldsymbol{D}_{\Theta 2} - \boldsymbol{D}_{\Theta 1}) = 0$ and $\boldsymbol{n}\cdot(\boldsymbol{B}_2 - \boldsymbol{B}_1) = 0$ are always fulfilled, since transverse waves are assumed to vanish, i.e. $B_z = 0$ and $E_z = 0$. The only non-trivial interface conditions are:

$$\boldsymbol{n}\times(\boldsymbol{H}_{\Theta,2} - \boldsymbol{H}_{\Theta,1}) = 0\,, \tag{4.12}$$

$$\boldsymbol{n}\times(\boldsymbol{E}_2 - \boldsymbol{E}_1) = 0\,, \tag{4.13}$$

where $\boldsymbol{n} = \hat{\boldsymbol{e}}_z$ and it is assumed again that no free surface charges and currents are present.

Including bulk losses in the one-dimensional model does not change the interface conditions. The magnon losses Γ_m, photon losses Γ_ρ, and mixed losses $\Gamma_{\times,1}$ and $\Gamma_{\times,2}$ are included in complete analogy to section 3.1.4. The resulting equations of motion are:

$$\mathbf{K}\,\partial_t^2\boldsymbol{X} - \boldsymbol{\Gamma}\,\partial_t\boldsymbol{X} + \mathbf{M}\,\boldsymbol{X} = 0\,, \tag{4.14}$$

where we define

$$\boldsymbol{X} = \begin{pmatrix} E_y \\ \delta\Theta \\ a \end{pmatrix}, \quad \mathbf{K} = \begin{pmatrix} 1 & \frac{\alpha}{\pi}\frac{B_e}{\epsilon} & \frac{g_{a\gamma}B_e}{\epsilon} \\ 0 & 1 & 0 \\ 0 & 0 & 1 \end{pmatrix}, \quad \boldsymbol{\Gamma} = \begin{pmatrix} \Gamma_\rho & \Gamma_{\times,1} & 0 \\ \Gamma_{\times,2} & \Gamma_m & 0 \\ 0 & 0 & 0 \end{pmatrix},$$

$$\mathbf{M} = \begin{pmatrix} \frac{k^2}{n^2} & 0 & 0 \\ -\Lambda B_e & v_z^2k^2 + m_\Theta^2 & 0 \\ -g_{a\gamma}B_e & 0 & k^2 + m_a^2 \end{pmatrix}. \tag{4.15}$$

No losses for the DA are included since a valid DM candidate must, by necessity, have an astronomically long lifetime (indeed, the QCD axion in the mass range of interest satisfies this constraint by many orders of magnitude).

4.2 Dark matter signal calculation

In this section, we solve the linearized equations of motion (4.14). We first consider the lossless case and then generalize the solutions to include losses. Material properties are always considered piecewise homogeneous, We introduce a matrix formalism to calculate emitted photon and axion power from an experimental setup with multiple TMI layers. We apply the matrix formalism to our benchmark setup, a single-TMI layer surrounded by vacuum. Using a multi-layer might be able to boost the signal, similar to multi-layer proposals for the MADMAX haloscope [47], although the higher frequencies considered here would lead to significant mechanical challenges if any tuning was required. Note that we set $v_z = 0$ in our calculations, cf. section 3 for an explanation.

JCAP08(2021)066

4.2.1 Solution of the one-dimensional model

Lossless case ($\Gamma = 0$). We first focus on the case without losses. The dispersion relation implied by eq. (4.14) is:

$$\left(k^2 - \frac{k_a^2 + k_\Theta^2}{2}\right)^2 = b_a^2 k_p^2 + \left(\frac{k_a^2 - k_\Theta^2}{2}\right)^2 , \tag{4.16}$$

where $b_a^2 = \frac{g_{a\gamma}^2 B_e^2}{\epsilon}$ was defined in analogy to $b^2 = \frac{\alpha}{\pi}\frac{\Lambda B_e^2}{\epsilon}$. The dispersion relations, up to leading order in the DA-photon coupling, therefore are

$$k_+ = k_\Theta + \mathcal{O}(g_{a\gamma}^2) , \tag{4.17}$$

$$k_- = k_a + \mathcal{O}(g_{a\gamma}^2) . \tag{4.18}$$

The most general ansatz for the fields is:

$$\begin{aligned} E &= \hat{E}^{++} e^{ik_\Theta z} + \hat{E}^{+-} e^{-ik_+ z} + \hat{E}^{-+} e^{ik_- z} + \hat{E}^{--} e^{-ik_- z} , \\ \delta\Theta &= \delta\hat{\Theta}^{++} e^{ik_+ z} + \delta\hat{\Theta}^{+-} e^{-ik_+ z} + \delta\hat{\Theta}^{-+} e^{ik_- z} + \delta\hat{\Theta}^{--} e^{-ik_- z} , \\ a &= s\hat{a}^{++} e^{ik_+ z} + \hat{a}^{+-} e^{-ik_+ z} + \hat{a}^{-+} e^{ik_- z} + \hat{a}^{--} e^{-ik_- z} . \end{aligned} \tag{4.19}$$

In the following, we focus on the DA zero-velocity limit, i.e. $k_a = 0$. This is an appropriate approximation for dark matter and the most general ansatz in eq. (4.19) reduces to:

$$\begin{aligned} E &= \hat{E}^{++} e^{ik_\Theta z} + \hat{E}^{+-} e^{-ik_+ z} + \hat{E}^{-} , \\ \delta\Theta &= \delta\hat{\Theta}^{++} e^{ik_+ z} + \delta\hat{\Theta}^{+-} e^{-ik_+ z} + \delta\hat{\Theta}^{-} , \\ a &= \hat{a}^{++} e^{ik_+ z} + \hat{a}^{+-} e^{-ik_+ z} + \hat{a}^{-} , \end{aligned} \tag{4.20}$$

where we omit the y index of the E-field since we ignore the E_x-component. The case of finite axion velocity was explored in ref. [126].

Plugging eq. (4.20) into the equations of motion, eqs. (4.9)–(4.11), we obtain relations between the constants in the general ansatz. After plugging these relations back into the ansatz (4.20), we obtain:

$$\begin{pmatrix} E \\ \delta\Theta \\ a \end{pmatrix} = \hat{E}^{++} \begin{pmatrix} 1 \\ \Theta_E^+ \\ a_E^+ \end{pmatrix} e^{ik_+ z} + \hat{E}^{+-} \begin{pmatrix} 1 \\ \Theta_E^+ \\ a_E^+ \end{pmatrix} e^{-ik_+ z} + \hat{a}^{-} \begin{pmatrix} E_a^- \\ \Theta_a^- \\ 1 \end{pmatrix} , \tag{4.21}$$

where the following variables were defined:

$$\Theta_E = \frac{\Lambda B_e}{m_\Theta^2 - \omega^2} , \quad a_E = \frac{g_{a\gamma} B_e}{k^2} , \tag{4.22}$$

$$E_a = \frac{\omega^2 \mu g_{a\gamma} B_e}{k^2 - k_\Theta^2} , \quad \Theta_a = \Theta_E E_a . \tag{4.23}$$

From eq. (4.21) it becomes clear that the dynamical AQ is completely determined by fixing the variables $\hat{E}^{++}$, $\hat{E}^{+-}$, and $\hat{a}^{-}$. In the next section we show that these variables can be fully determined by using the interface conditions for the electromagnetic and DA fields. Therefore no boundary conditions for the AQ need to be applied.[6]

[6] If we were to consider a finite spin wave velocity, we would obtain three modes $k_{1,2,3}^2$. In this case, the most general ansatz would have six unknowns per field, and we would have to specify boundary conditions for the AQ.

JCAP08(2021)066

The case with losses ($\Gamma \neq 0$). When losses are included, the full dispersion relation $k_\pm^2$ takes on a more complicated form. However, in the limit $g_{a\gamma} \to 0$ we find that $k_-^2 \to k_a^2$ and $k_+^2 \to k_\Theta^2$, where k_Θ^2 is given by eq. (3.47). In what follows, a_E and E_a are needed also in the case of losses. a_E in eq. (4.22) does not get modified in the case of losses, and E_a has the same form as in eq. (4.23). However, we now require the full form of k_Θ from eq. (3.47).

4.2.2 Matrix formalism

In the previous section, we described the solution of the linearized equations in a homogeneous medium. Here, we discuss solutions for the fields in a multilayer system that consists of $N+1$ media, cf. figure 10. We use the same labels for the media as in section 3.2.2. There are N interfaces, which we label by $r = 0, \ldots, N$. The first interface is at $z_0 = z_1$ and the last interface is at z_N. The material properties in eq. (4.21) of each medium are labeled with the corresponding index r as a subscript. The constant Θ^0 does not influence the emitted photon signal at lowest order and is therefore neglected in the following. We further introduce a phase similar to the case of AQ-photon mixing is introduced in the ansatz, cf. eq. (3.51). The external B-field B_e is the same in all media and is polarized in the y-direction. Recall that we consider the DA zero-velocity limit with a zero spin wave velocity.

Applying the interface conditions for the electromagnetic fields, cf. eq. (4.12), (4.13), and (4.13) and for the DA, cf. eq. (4.7), at z_r between medium $r-1$ and r we obtain the following system of equations:

$$\boldsymbol{t}_r = \mathbf{M}_r^{-1}\, \mathbf{M}_{r-1}\, \mathbf{P}_{r-1}\, \boldsymbol{t}_{r-1}\,, \tag{4.24}$$

with

$$\mathbf{M}_r = \begin{pmatrix} 1 & 1 & E_{a,r}^- \\ \frac{k_+^r}{\mu_r} & -\frac{k_\pm^r}{\mu_r} & 0 \\ a_{E,r}^+ & a_{E,r}^+ & 1 \end{pmatrix}\,, \quad \boldsymbol{t}_r = \begin{pmatrix} \hat{E}_r^{++} \\ \hat{E}_r^{+-} \\ \hat{a}_r^- \end{pmatrix} \tag{4.25}$$

and, defining $\Delta_r^+ \equiv k_+^r (z_{r+1} - z_r)$,

$$\mathbf{P}_r = \mathrm{diag}(\mathrm{e}^{i\Delta_r^+}, \mathrm{e}^{-i\Delta_r^+}, 1)\,. \tag{4.26}$$

In complete analogy to section 3.2.2 the S-matrix, which relates the states in media 0 and N to each other, is defined via

$$\boldsymbol{t}_N = \mathbf{S}\, \boldsymbol{t}_0\,. \tag{4.27}$$

The expressions for one, two, ..., N interfaces are the same as in eqs. (3.56)–(3.58). The unknown fields can be calculated from the S-matrix as follows:

$$\begin{pmatrix} \hat{E}_N^{++} \\ \hat{E}_0^{+-} \\ \hat{a}_N^- \end{pmatrix} = -\hat{a}_0^- \begin{pmatrix} -1 & S_{12} & 0 \\ 0 & S_{22} & 0 \\ 0 & S_{32} & -1 \end{pmatrix}^{-1} \cdot \begin{pmatrix} S_{13} \\ S_{23} \\ S_{33} \end{pmatrix}\,, \tag{4.28}$$

where the amplitude of the DAs is known and, has to lowest order the same magnitude in each medium $|\hat{a}_0^-| = |\hat{a}_r^-|$ for all $r = 1, \ldots, N$. The emitted E-field in medium N that propagates in the positive z-direction is called $\hat{E}_N^{++}$. The emitted E-field that propagates in the negative z-direction is called $\hat{E}_0^{+-}$.

JCAP08(2021)066

4.2.3 Layer of topological insulator

Let us now consider the case of a single TMI layer (hosting a dynamical AQ) surrounded by vacuum. Dark axions are present in the form of an background field that oscillates in time with a frequency that is determined by the DA mass, m_a. The DAs mix with the AQs and photons. In terms of the matrix formalism, there are two interfaces ($N = 2$), with media 0 and 2 are vacuum, and medium 1 is a TMI of thickness d. The TMI has constant refractive index $n^2 = \epsilon$,[7] and losses $\mathbf{\Gamma}$. The external B-field is present in all media. The DAs have the same magnitude in each medium, which is determined by the axion dark matter density ρ_a: $|\hat{a}_0^-|^2 = |\hat{a}_r^-|^2 = 2\rho_a/m_a^2$.

The three-way mixing between DAs, AQs, and photons produces a photon at the boundary, which propagates away from the TMI layer. Note that, since we neglect the spin wave velocity, the system behaves essentially as a two-level system of massive photons and DAs. The emitted E-fields in media 0 and 2 are denoted by $\hat{E}_0^{+-}$ and $\hat{E}_2^{++}$, respectively. Recall that $\hat{E}_0^{+-}$ is the E-field amplitude that is emitted in negative z-direction in medium 0 and $\hat{E}_2^{++}$ is the emitted photon signal emitted in the positive z-direction in medium 2. We assume that the DA particles are effectively at rest. In this limit there is no preferred direction and the magnitudes of $\hat{E}_2^{++}$ and $\hat{E}_0^{+-}$ are the same.

Lossless case ($\mathbf{\Gamma} = \mathbf{0}$). The full formula for $\hat{E}_2^{++}$ from the matrix formalism is impractical. We therefore quote the result first order in the DA-photon coupling, which, assuming that $g_{a\gamma}$ is sufficiently small, should be a good approximation:

$$\hat{E}_2^{++} = \hat{a}_0^- \frac{\sin(\Delta/2)\,(n_\Theta^2 - 1)}{n_\Theta\,(n_\Theta \sin(\Delta/2) + i\cos(\Delta/2))}\, g_{a\gamma}\, B_e + \mathcal{O}\left((g_{a\gamma}\, B_e)^2\right), \tag{4.29}$$

where we define the phase depth $\Delta = dk_\Theta = d\omega n_\Theta$ (where k_Θ is the lossless solution to the dispersion relation, eq. (3.34)) and the effective refractive index is

$$\boxed{n_\Theta^2 = n^2\left(1 - \frac{b^2}{\omega^2 - m_\Theta^2}\right).} \tag{4.30}$$

Furthermore, we used in the language of the matrix formalism, such that $a_{E,0}^+ = \frac{g_{a\gamma}\, B_e}{\omega^2} = a_{E,2}^+$, $E_{a,0}^- = -g_{a\gamma}\, B_e = E_{a,2}$, and $a_{E,1}^+ = \frac{g_{a\gamma}\, B_e}{n_\Theta^2 \omega^2}$, $E_{a,1}^- = -\frac{g_{a\gamma}\, B_e}{n_\Theta^2}$. From now on, terms of the order $\mathcal{O}\left((g_{a\gamma}\, B_e)^2\right)$ are omitted to simplify the expressions. We also normalize the field amplitude $\hat{E}_2^{++}$ to the DA-induced field in vacuum, $E_0 = g_{a\gamma}\, B_e\, a_0^-$,

$$\frac{\hat{E}_2^{++}}{E_0} = -\frac{\sin(\Delta/2)\,(1 - n_\Theta^2)}{n_\Theta\,(n_\Theta \sin(\Delta/2) + i\cos(\Delta/2))}. \tag{4.31}$$

Note that eq. (4.31) has the same form as in the case of fields emitted from as a dielectric disk [47], with the effective refractive index n_Θ, which is equivalent to introducing a photon mass.

From analysing eq. (4.31), it becomes clear that a resonance occurs if the condition

$$\Delta = \Delta_j = n_\Theta(\omega_j)\,\omega_j d = (2j+1)\,\pi\,, \quad j \in \mathbb{N}_0\,, \tag{4.32}$$

[7] A nontrivial permeability, $\mu \neq 1$, can be incorporated straight-forwardly into the matrix formalism, described in the previous sections. However, we set $\mu = 1$ for simplicity and because this is a good approximation for the TMI materials discussed in section 2.4.

JCAP08(2021)066

is fulfilled. Here, ω_j are the resonance frequencies, which are located at

$$\omega_j^2 = \frac{\omega_{\rm LO}^2}{2} + \sqrt{\frac{\omega_{\rm LO}^4}{4} + \Delta_j^2 \frac{b^2}{n^2 d^2}} = \omega_{\rm LO}^2 + \delta\omega_j^2 + \mathcal{O}\left(\frac{4\Delta_j^2 b^2}{n^2 d^2 \omega_{\rm LO}^4}\right), \tag{4.33}$$

where we have defined

$$\delta\omega_j^2 \equiv \frac{\Delta_j^2 b^2}{n^2 d^2 \omega_{\rm LO}^2}. \tag{4.34}$$

From eq. (4.33), it is evident that — in the lossless limit — the resonance frequencies are always larger than $\omega_{\rm LO}$, i.e. $\omega_{\rm LO} < \omega_0 < \omega_1 < \ldots$. As the thickness of the TMI increases, $d \to \infty$, the resonant frequencies converge to the limiting value, i.e. $\omega_j \to \omega_{\rm LO}$. Furthermore, eq. (4.33) implies that the resonance frequency ω_j can be *tuned* via the external B-field, since $b \propto B$. In section 5.1 we investigate the frequency and, equivalently, DA mass range that can be scanned with our benchmark materials and realistic external B-fields.

To understand why the frequencies defined via eq. (4.32) are indeed resonance frequencies, consider the following: equation (4.32) implies that $\cos\Delta_j = 0$ and, hence, the emitted field in eq. (4.31) is $\hat{E}_2^{++} \sim 1/n_\Theta^2 - 1 \sim 1/n_\Theta^2$ for small n_Θ. In fact, the smaller n_Θ the more pronounced the resonance and, from figure 7, we can see that this is the case when $\omega_j \sim \omega_{\rm LO}$. Consequently, resonances that are further away from $\omega_{\rm LO}$ (i.e. $j > 0$) have less pronounced peak values, such that the maximal value of $\hat{E}_2^{++}$ is always obtained for $j = 0$. Furthermore, eq. (4.33) reveals that resonances are more pronounced for larger sample thickness d of a given TMI. We now investigate the resonances in more detail and provide analytical expressions for their widths and maximum values.

Around the resonances we have $|n_\Theta| \ll 1$, and eq. (4.31) can be approximated as:

$$\frac{\hat{E}_2^{++}}{E_0} = -\frac{1}{n_\Theta^2 + i\, n_\Theta \cot\left(\frac{\Delta}{2}\right)}. \tag{4.35}$$

Expanding n_Θ^2 around ω_j^2 yields, to lowest order,

$$n_\Theta^2 = n^2 \frac{\delta\omega_j^2}{b^2}, \tag{4.36}$$

where we require that $b^2 > \delta\omega_j^2$. The expansion of $\cot(\Delta/2)$ leads, to lowest order, to

$$\cot\left(\frac{\Delta}{2}\right) = -\frac{1}{2}\frac{\omega_j d n^2}{2 n_\Theta(\omega_j) b^2}\left(\omega^2 - \omega_j^2\right). \tag{4.37}$$

The emitted fields in eq. (4.35) can then be approximated about the resonances as follows:

$$\frac{\hat{E}_2^{++}}{E_0} = -\frac{i A_j}{i\gamma_j\omega_j + (\omega^2 - \omega_j^2)}, \tag{4.38}$$

with

$$\gamma_j = \frac{4}{d}\frac{\omega_j^2 - \omega_{\rm LO}^2}{\omega_j^2} \approx \frac{4\Delta_j^2 b^2}{n^2 d^3 \omega_{\rm LO}^4}, \tag{4.39}$$

$$A_j = \frac{4b^2}{n^2 \omega_j d} \approx \frac{4b^2}{n^2 \omega_{\rm LO} d}, \tag{4.40}$$

where we used that in a resonant case ω_j is close to $\omega_{\rm LO}$.

JCAP08(2021)066

The power output on resonance is:

$$P = \frac{|E_0|^2}{2}\beta^2 A\,, \tag{4.41}$$

where A is the surface area of the TMI layer and where we used that the Poynting vector in z-direction has magnitude $\frac{1}{2}|\hat{E}_2^{++}|^2$. The power boost factor β^2 is defined as

$$\beta^2 = \left|\frac{\hat{E}_2^{++}}{E_0}\right|^2 . \tag{4.42}$$

Following ref. [47], we refer to the unsquared β as the boost factor.

The full width at half the maximum value (FWHM) of β^2 about the resonance ω_j is given by γ_j. The highest value at the resonance, the peak amplitude, ω_j is given by

$$\beta^2(\omega_j) = \frac{A_j^2}{\gamma_j^2\omega_j^2} \approx \left(\frac{d\omega_{\rm LO}}{\Delta_j}\right)^4 \approx \frac{1}{n_\Theta(\omega_j)^4}. \tag{4.43}$$

With eq. (4.43) it now becomes explicitly clear that the higher modes have a lower maximum resonance value, since $\Delta_j < \Delta_{j+1}$. Also large layer thicknesses d increases the maximal emitted E-field on resonance. Therefore to achieve a certain amount of signal boost from one layer of TMI a relatively large layer thickness $d > 1/\omega$ is needed. Equation (4.39) tells us the necessary information about the width of the resonance. First note, that going to larger modes j or larger b will increase the FWHM γ_j. Relatively thick TMI layers, i.e. large d, yield a very narrow resonance. Therefore a good balance for d has to be found because d should be relatively large to reach a high resonance value. The refractive index n does not affect the maximum value of the resonance, cf. eq. (4.43). However large n makes the FWHM γ_j very small. We therefore conclude that it is advantageous to have low n materials fro broadband response.

In figure 15 the boost amplitude β is shown for our benchmark material $Mn_2Bi_2Te_5$ for four different layer thicknesses. For the thinnest case, $d = 0.2\,\text{mm}$, no clear enhancement of the boost factor is reached, since for this relatively small thickness we obtain a resonance frequency ω_0 (dashed vertical line) that is too far away from $\omega_{\rm LO}$ (solid vertical line) such that $n_\Theta(\omega_0)$ is not much smaller than unity. For $d = 2\,\text{mm}$ we have a resonance at ω_0. A larger width, but a lower maximum value, is realized at the second resonance peak ω_1. According to eq. (4.39), the width of the resonance around ω_1 should be broader by a factor of about $(\Delta_1/\Delta_0)^2 = 9$ than the resonance width around ω_0.

For thicker samples still, $d = 5\,\text{mm}$, $d = 10\,\text{mm}$ the resonant boost at ω_0 increases further. In particular from eq. (4.43) we find that the peak heights scale as $(d_1/d_2)^2$. Furthermore, the width of the peak around ω_0 shrinks as d increases. From eq. (4.39) we can directly read off that the width shrinks by a factor $(d_2/d_1)^3$. For $d = 10\,\text{mm}$ the linewidth of β is on the order of the DA linewidth, $10^{-6}m_a$. Without taking into account material losses the linewidth of the power boost factor is larger that the axion linewidth if

$$\gamma_j > 10^{-6}\omega_j \approx 10^{-6}\omega_{\rm LO}. \tag{4.44}$$

Equation (4.44) tells us the requirements for the material parameters such that the power boost factor bandwidth is larger than the axion linewidth.

JCAP08(2021)066

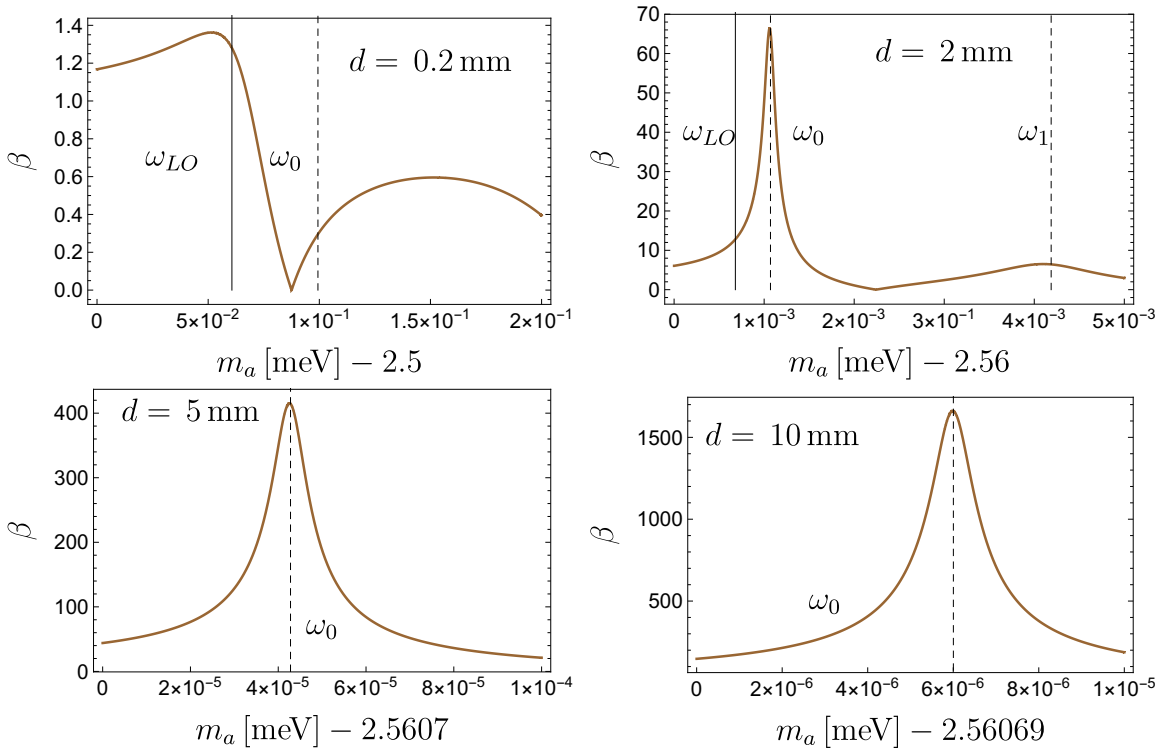

Figure 15. *Effect of material thickness, d, on the boost factor.* In the lossless limit for one layer β is given by eq. (4.31). We assume zero DA velocity ($v_{\rm DM} = 0$, valid when the resonance is wide compared to the DA linewidth). Typical material values for $Mn_2Bi_2Te_5$ TMI with an external B-field B_e of 2 T are chosen, cf. table 5 and eq. (2.3). Vertical lines mark the frequencies $\omega_{\rm LO}$ and the resonance frequencies ω_j. The resonance boost increases, and bandwidth decreases, as the thickness d increases.

Before we discuss the influence of material losses we want to give a clearer physical picture of the observed resonances. In figure 16 we consider three domains. The middle domain is a TMI layer with thickness d and with an effective refractive index $n_\Theta = \frac{1}{2}$. The two outer domains are vacuum with $n = 1$. The axion induced field, which is shown in blue, is one in vaccum and enhanced inside the TMI, cf. eq. (4.22). The enhancement of the axion induced field in the TMI layer is proportional to $\frac{1}{n_\Theta^2}$. Consider now the interface between the TMI and the left vacuum. To fulfil the continuity requirement of the total electric field, propagating modes (red) are emitted to both sides. One can check that this is indeed the case by adding the red and blue amplitudes at the interface. The emitted amplitude in vacuum is one, while the propagating fields inside the TMI are enhanced, since they are proportional to $\frac{1}{n_\Theta^2}$. The outlined scenario happens at both interfaces of the TMI. Let us first consider the emitted radiation that propagates inside the TMI from left to right. The radiation hits the right interface. The transmission and reflection coefficients determine the fraction of the radiation, which is transmitted to the outside or reflected. For plane waves we have $T = \frac{2n_\Theta}{1+n_\Theta}$ and $R = \frac{n_\Theta - 1}{1+n_\Theta}$. The important point is that the transmitted radiation is added in phase ($T > 0$) to the radiation which is emitted from the right interface to the outside. The part of radiation which is reflected at the right interface receives a phase shift since $R < 0$. Therefore the reflected radiation is coherently added to the radiation which is emitted from the right surface to the left in the TMI. A similar scenario happens at the left interface.

JCAP08(2021)066

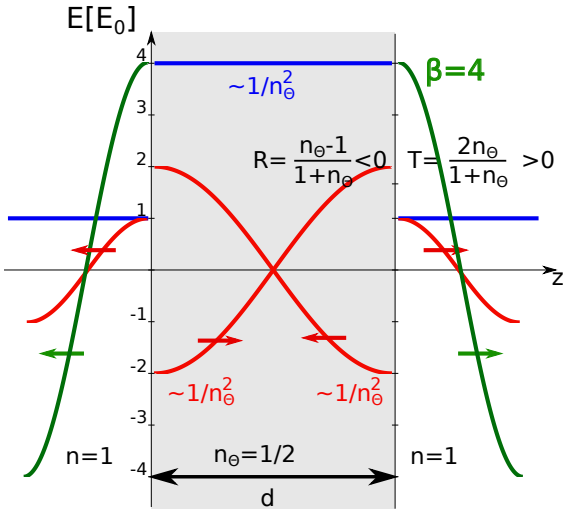

Figure 16. Physical understanding of the resonant enhancement of the emitted electromagnetic fields from the mixing between DAs, AQs and photons. The TMI layer (gray) of thickness d has an effective refractive index $n_\Theta = \frac{1}{2} < 1$ and is surrounded by vacuum. The axion induced field (blue) is enhances inside the TMI and since the total electric field has to be continuous over the two interfaces propagating modes (red) are emitted off both interfaces. The E-fields are given in units of the axion-induced field in vacuum, E_0. Due to the smallness of n_Θ around the resonance the transmission coefficient for the fields which propagate inside the TMI is small, while the reflection coefficient is large. Therefore effectively the TMI works as a cavity. After bouncing many times between the two interfaces the effective emitted field is proportinal to $\beta \gg 1$. In the specific example of n_Θ the emitted field is four times larger than the axion induced field in vacuum ($\beta = 4$). A more detailed description can be found in the text.

Now since $n_\Theta \ll 1$ the transmission coefficient is small and the reflection coefficient is large. Therefore the radiation bounces many times between both interfaces. After each bounce a small fraction of the radiation is transmitted to the outside. This is exactly how a cavity works and due to the fact that the transmitted fields to the outsides are all added coherently the total emitted field is enhanced by the boost factor $\beta = 1/n_\Theta^2$. The total emitted field is shown in green in figure 15. With this physical picture in mind we can also understand why larger thicknesses d lead to larger β's on resonance. To fulfill the resonance condition $n_\Theta(\omega_j)\omega_j d = \pi$ we need a smaller $n_\Theta(\omega_j)$ the larger we make d. However making $n_\Theta(\omega_j)$ smaller leads to a larger axion induced field and therefore also to a larger total emitted field.

Case with losses ($\Gamma \neq 0$). In the case of losses we can use that $g_{a\gamma}$ is a relatively small coupling and therefore $k_+ \to k_\Theta$, where k_Θ now includes losses, cf. eq. (3.47). $k_- \to k_a = 0$ in the axion zero velocity limit. Furthermore we have shown in section 4.2.1 that the relations for a_E and E_a still hold when we include the losses into the effective refractive index. In conclusion we can use eq. (4.31) also if losses are present. The only thing that we have to do is to use the effective refractive index which includes losses:

$$\boxed{n_\Theta^2 = n^2\left(1 + \frac{b^2}{m_\Theta^2 - \omega^2 - i\omega\Gamma_m} + i\frac{\Gamma_\rho}{\omega}\right).} \tag{4.45}$$

We subsequently neglect mixed losses.

JCAP08(2021)066

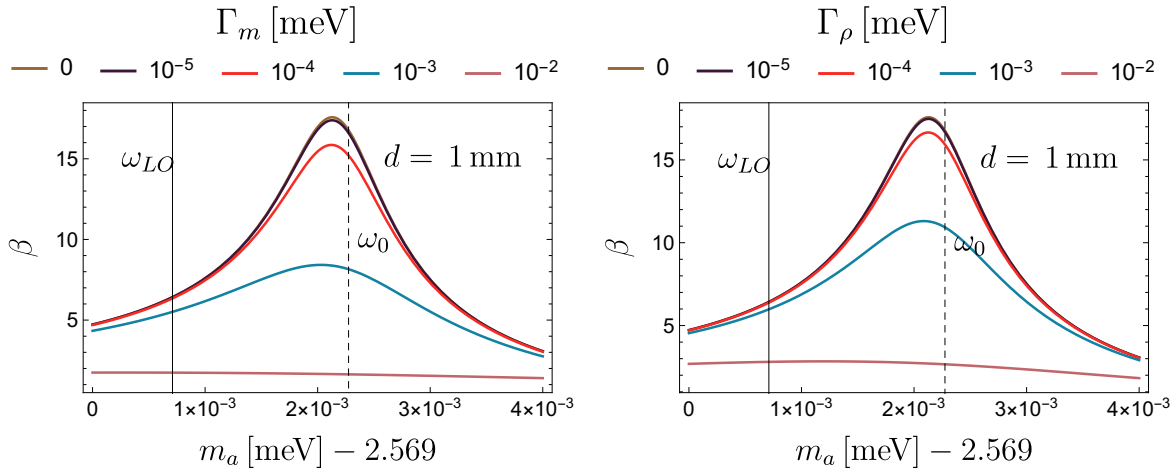

Figure 17. *Effect of losses on the boost factor.* TMI layer of thickness $d = 1\,\text{mm}$. Other parameters are as figure 15. *Left*: varying magnon losses Γ_m, with $\Gamma_\rho = 0$. *Right*: varying photon losses Γ_ρ with $\Gamma_m = 0$.

We begin by expanding the boost factor around the resonance frequencies ω_j, which remain unmodified by the losses, cf. eq. (4.32). Then an expansion can be done in complete analogy to the lossless case. For $|1 - n_\Theta^2(\omega_j)| \approx 1$ the emitted field takes the same form as in the lossless case, cf. eq. (4.35), where n_Θ is given now by eq. (4.45). We now expand the two terms, n_Θ^2 and $\cot\left(\frac{\Delta}{2}\right)$, that appear in the denominator in eq. (4.35). We find

$$n_\Theta^2(\omega_j) = n^2\left(\frac{\delta\omega_j^2}{b^2} + i\tilde{\Gamma}_j^2\right) \tag{4.46}$$

with $\tilde{\Gamma}_j^2 \equiv \frac{\Gamma_\rho}{\omega_j} + \frac{\omega_j\Gamma_m}{b^2}$. In deriving eq. (4.46) we have assumed that $b^2 > \delta\omega_j^2$ and $b^2 > \omega_j\Gamma_m$. If such a condition is not fulfilled, the material is likely too lossy to be useful in DA detection. Next we consider the nearly lossless limit, i.e. $\frac{\delta\omega_j^2}{b^2} > \tilde{\Gamma}_j^2$. In this case the relevant expressions for us are $n_\Theta(\omega_j) = n\frac{\delta\omega_j}{b}\left(1 + i\frac{1}{2}\frac{\tilde{\Gamma}_j^2}{\delta\omega_j^2}b^2\right)$ and $n_\Theta^2(\omega_j) = n^2\frac{\delta\omega_j^2}{b^2}$, where we have written down only the important leading order terms. Next we expand the $\cot\left(\frac{\Delta}{2}\right)$ term:

$$\cot\left(\frac{\Delta}{2}\right) = \cot\left(\frac{\Delta}{2}\right)_{\omega^2=\omega_j^2} + \left[\frac{\partial}{\partial\omega^2}\cot\left(\frac{\Delta}{2}\right)\right]_{\omega^2=\omega_j^2}\left(\omega^2 - \omega_j^2\right) + \cdots \tag{4.47}$$

where we approximate $\omega \approx \omega_j$ for the linear dependencies and the dots represent higher order terms, which we do not have to consider for a reasonable expansion. The expansion in eq. (4.47) can be simplified in the small thickness limit, $\text{Im}\left[\Delta(\omega_j)\right] < 1$. Equation (4.47) then simplifies to:

$$\cot\left(\frac{\Delta}{2}\right) = -i\frac{\text{Im}\left[\Delta(\omega_j)\right]}{2} - \frac{1}{4}\frac{\Delta_j}{\delta\omega_j^2}\left(\omega^2 - \omega_j^2\right) \tag{4.48}$$

Putting everything together we obtain — as in the lossless case, cf. eq. (4.38) — a Lorentzian shaped functional dependence around the resonance frequencies. The width of the curve

JCAP08(2021)066

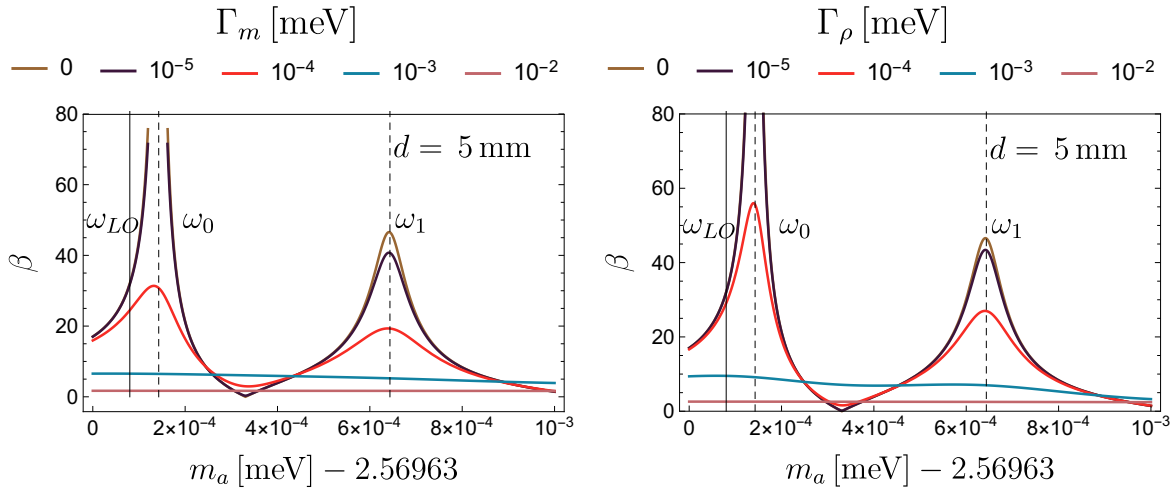

Figure 18. *Effect of losses on the higher resonance peaks.* TMI layer of thickness $d = 5\,\mathrm{mm}$. Other parameters are as figure 17. The value of β at ω_0 without losses is around $\beta \approx 500$, cf. figure 15 (bottom left). Therefore the relative reduction due to losses at the resonant frequencies is larger at ω_0 than at ω_1.

receives an additional term in the presence of losses:

$$\gamma_j = \frac{4b^2\Delta_j^2}{n^2\omega_{\mathrm{LO}}^4 d^3} + \left(\Gamma_m + \frac{b^2}{\omega_{\mathrm{LO}}^2}\Gamma_\rho\right) , \tag{4.49}$$

and the amplitude A_j remains unchanged with respect to the lossless case.

In figure 17 we show the boost factor β around the first resonance ω_0 for a layer thicknesses of $d = 1\,\mathrm{mm}$ for different values of the loss parameters Γ_ρ and Γ_m. We observe that each loss parameter has a similar quantitative effect on redicing the boost factor peak, with magnon losses being only slightly more important. This is due to the fact that Γ_m directly enters the resonance, cf. eq. (4.45), while photon losses Γ_ρ only enter via an additional term that is added to the other terms of the dispersion relation.

Next let us discuss the effect of losses on the higher resonance frequencies. In figure 18 we show the first two resonance peaks at ω_0 and ω_1 for $d = 5\,\mathrm{mm}$. In the lossless case we have $\beta(\omega_0) \approx 500$, cf. figure 15. The reduction of the ω_0 resonance is therefore more severe than the resonance at ω_1. This is simply the case because the system is more resonant at ω_0 and losses lead to a larger reduction. We conclude that losses may lead to a scanning strategy in the end that uses a higher resonance mode $j > 0$. However, the final scanning strategy can only be given when the losses are determined experimentally.

We can see from eq. (4.49) that the point where losses dominate is a function of the refractive index, thickness of the material and intrinsic losses. While, in the lossless case, increasing the thickness of the layer increases the resonance, we can see that this is limited by the losses, which give a width independent of d. Looking at the height of the resonance in the loss dominated limit is quite revealing

$$\beta(\omega_j) = \frac{A_j}{\gamma_j\omega_j} = \frac{4b^2}{n^2\omega_{\mathrm{LO}}^2 d}\,\frac{1}{\frac{4b^2\Delta_j^2}{n^2\omega_{\mathrm{LO}}^4 d^3} + \frac{b^2}{\omega_{\mathrm{LO}}}\left(\frac{\omega_{\mathrm{LO}}\Gamma_m}{b^2} + \frac{\Gamma_\rho}{\omega_{\mathrm{LO}}}\right)} \overset{\text{loss dom.}}{\approx} \frac{4}{dn^2\left(\frac{\omega_{\mathrm{LO}}^2}{b^2}\Gamma_m + \Gamma_\rho\right)} . \tag{4.50}$$

JCAP08(2021)066

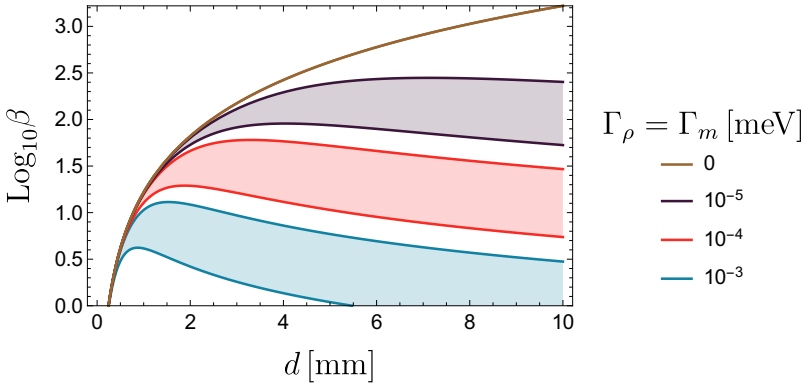

Figure 19. Maximal boost factor β on resonance at ω_0 with respect to the TMI layer of thickness d for different levels of loss. Material parameters correspond to $Mn_2Bi_2Te_5$ with $B = 2\,\mathrm{T}$. The bands show variation of the refractive index from $n = 3$ (upper curve of the bands) to $n = 7$ (lower curve of each band).

Unlike the lossless case, increasing d now hinders the resonance height, if not its width. Similarly, while n does not effect γ_j, again the height is significantly reduced on resonance, further discouraging high n materials. Once the loss term of a material is known, the optimal thickness can be found by requiring that losses do not dominate.

To get an idea of the scale of the maximum losses that still allow for useful DA detection, we plot the maximum of β at the first resonance ω_0 as a function of d in figure 19. The different colours indicate different losses. We also vary the refractive index around our best guess value, $n = 5$: the upper band for each colour corresponds to $n = 3$, while the lower to $n = 7$. Lower values of n lead to greater boost factor maxima.

From figure 19 we can read off that for given material parameters there is an optimal thickness, which maximizes β on resonance. Analytically one can show

$$\boxed{d_{\mathrm{opt}} = \frac{2}{\omega_{\mathrm{LO}}}\left(\frac{\Delta_j}{n}\right)^{\frac{2}{3}}\left(\frac{1}{\frac{\Gamma_\rho}{\omega_{\mathrm{LO}}} + \frac{\Gamma_m \omega_{\mathrm{LO}}}{b^2}}\right)^{\frac{1}{3}}}. \tag{4.51}$$

Note that the otimal thickness d_{opt} gives a thickness that is consistent with the small d limit that we have used in the expansion only if $2\left(n^2\tilde{\Gamma}_j^2\Delta_j\right)^{\frac{1}{3}} < 1$. This inequality is fulfilled for the cases that we are interested in. In the zero loss limit the optimal thickness d_{opt} diverges. However it is important to stress that in this limit $\gamma_j \to 0$ and our optimal thickness has to be understood as the thickness that maximizes β on resonance. Which thickness will be the optimal one with respect to a scanning strategy and sensitivity reach will be discussed in the next section. If the losses are finite they enter with the third root. Also note that scanning different frequencies changes ω_{LO} and therefore in principle for each scanning frequency a different optimal layer thickness is needed. It is not possible to change the layer thickness for each scanning frequency, and therefore the true optimal thickness will depend on the details of the frequencies to be scanned and the scan strategy.

Note that in figure 19 we are approximating the boost factor as a resonance. However, as $\beta \to 1$ the boost factor is no longer well described by a Lorentzian. For the purposes of an experiment, all advantage over say a dish antenna is then lost. To estimate the highest

JCAP08(2021)066

allowable losses, we can note that the strongest resonance occurs when $\delta_j = Pi$ and $d = d_{\rm opt}$. By requiring that $\beta \gg 1$ we then find the requirement

$$\frac{\Gamma_\rho}{\omega_{\rm LO}} + \frac{\Gamma_m \omega_{\rm LO}}{b^2} \ll \frac{1}{2n^2}\,. \tag{4.52}$$

Thus the highest allowable losses are actually set by the refractive index of the material, at least in order to ensure a resonance occurs.

5 Dark matter discovery potential

In this section, we review the suitability of TMIs hosting AQs for DA detection. We systematically investigate the discovery reach of the proposed single-TMI-layer benchmark experiment, and the necessary requirements for THz detectors. Astrophysical limits on the axion mass and coupling, and motivation for axion DM in the milliectronvolt range, is reviewed in appendix B.

5.1 Scanning range

Before considering THz detection technology and the reach of the proposed experiment in terms of the DA coupling, $g_{a\gamma}$, we first determine the range of DA masses that can in principle be accessed using TMIs. Recall from section 4.2.3 that the resonance frequencies of the experiment, ω_j, can be tuned by changing the external magnetic field, $B_{\rm e}$. To estimate the resulting range, we look at the first resonance ω_0 since $|\beta(\omega_0)| > |\beta(\omega_j)|$ for all $j > 0$. Doing so, we find that

$$\omega_0(B_{\rm e}) \approx \omega_{\rm LO}(B_{\rm e}) = \sqrt{m_\Theta^2 + b^2(B_{\rm e})}\,, \tag{5.1}$$

where m_Θ is the AQ mass and b is given by eq. (2.3). In the limit of $B_{\rm e} \to 0$ we simply have $\omega_0 \to m_\Theta$, while for very strong B-fields of $B_{\rm e} = 10\,\mathrm{T}$ and our benchmark parameters in table 8 (our best approximation to $Mn_2Bi_2Te_5$), we find that

$$1.8\,\mathrm{meV} = m_\Theta < \omega_0 < 8.2\,\mathrm{meV}\,. \tag{5.2}$$

As of now, the DA mass is unknown, so it is desirable to cover a wide range of axion masses with a given TMI crystal. Since typical magnetic fields in the lab are restricted to the order of a few tesla, we cannot arbitrarily increase $B_{\rm e}$ and hence need to maximise the relative response of the AQ to $B_{\rm e}$, viz.

$$\frac{1}{m_\Theta}\frac{\mathrm{d}b}{\mathrm{d}B_{\rm e}} = \frac{\alpha}{\pi\sqrt{2}}\frac{1}{\sqrt{\epsilon} f_\Theta m_\Theta} \approx \frac{0.46}{\mathrm{T}}\left(\frac{25}{\epsilon}\right)^{1/2}\left(\frac{70\,\mathrm{eV}}{f_\Theta}\right)\left(\frac{1.8\,\mathrm{meV}}{m_\Theta}\right)\,. \tag{5.3}$$

This means that smaller f_Θ, m_Θ, or ϵ are beneficial for a TMI in order to cover a larger range of frequencies for a given maximum possible value of the applied B-field.

A large relative AQ response in eq. (5.3) is only beneficial if the applied B-field value can be controlled to sufficiently high accuracy over the course of the measurement. This is because fluctuations in $B_{\rm e}$ will translate into fluctuations in ω_0, which might result in the resonance around ω_0 fluctuating in and out of the bandwidth of the detector. The magnet design for TOORAD will thus require relatively precise control of the B-field, and could be a limitation in cost, field strength, or total volume.

JCAP08(2021)066

Detector type	Fundamental noise limit		Metric
Amplifiers & heterodyne mixers	quantum noise	$\hbar\omega$ [127, 129, 130]	T_Q
Bolometers	thermal fluctuations	$\sqrt{4G_{\rm th}k_{\rm B}T_0}$ [45, 128]	NEP
Calorimetric SPDs	energy resolution for finite bandwidth	$\sqrt{C_{\rm th}k_{\rm B}T_0^2}$ [131, 132]	dark count rate

Table 7. Comparison of detector technologies for searching dark matter using quasiparticle axions. See the main text for explanations of the symbols.

5.2 Detectors for THz radiation

Searching for dark DAs is challenging because the resultant photon signal is very weak and can be hidden in wide range of frequencies, since the DA mass in unknown. To improve our chance of success, we need to understand the intrinsic and extrinsic background noise of our photon detection system, coupling efficiency of photon detectors to our proposed experimental setup, and scalability in collecting more photons from the material that hosts the AQ. In earlier sections, we have discussed the generation of electromagnetic radiation in the THz (millimeter wave) regime using AQs for DA detection. We will focus here to the available technology to detect these photons with energies from 0.01 to a few THz.

Detectors that have high sensitivity for the search of DAs in our frequency range of interest include amplifiers, heterodyne mixers, bolometers, and single-photon detectors (SPDs). We shall consider experiments performing at temperatures much lower than the frequency, i.e. $T \ll \omega$ to avoid the thermal photons from the blackbody radiation and to focus on the fundamental limit of photon detection [127–130]. Since amplifiers and heterodyne mixers, e.g. superconductor-insulator-superconductor (SIS) and hot-electron bolometric mixers, are sensitive to the voltage or the electric field of the signal, we can put them into one category, while bolometers and SPDs go into another. We present a comparison of all detector types discussed in what follows in table 7.

State-of-the-art amplifiers and mixers can detect a very weak signal from as little as a few photons by parametric amplification or non-linear mixing processes. As the signal-to-noise ratio is given by the ratio of the number of photons in the signal to that in the amplifier noise, the amplifier noise can be quantified naturally in units of photon quanta, i.e. $\hbar\omega$, or amplifier noise temperature, i.e. $T_Q = \hbar\omega/k_{\rm B}$. For the linear, phase-preserving amplification, the minimum amplifier noise is one quanta [127, 129, 130]. Half of this comes from the quantum fluctuation from the parametric pumping port used in modulation for the amplification gain, whereas another half from the quantum noise in the signal port. At lower microwave frequencies, quantum noise-limited amplifiers have been achieved based on parametric effects [133–135] and, at higher frequencies, in SIS detectors [129, 136], hot electron bolometric mixers [137, 138], and plasmonic mixers [139]. However, the insertion loss and insufficient first amplification gain may degrade the overall performance, resulting in a higher system noise temperature $T_{\rm sys} \geq T_Q$. For a total measurement time, $t_{\rm meas}$, and measurement bandwidth, BW, the average noise is given by the Dicke radiometer formula,

$$\text{Noise} = \frac{T_{\rm sys}}{\sqrt{\text{BW}t_{\rm meas}}} \tag{5.4}$$

JCAP08(2021)066

Instead of amplifying the voltage, bolometers are high-sensitivity, square-law detectors that measure the power of microwave and far-infrared radiation. They operate by first absorbing the incident radiation and subsequently inferring the radiation power from the temperature rise due to the increase of its internal energy. The bolometer sensitivity is quantified by noise equivalent power (NEP), measured in units of $\mathrm{W}/\sqrt{\mathrm{Hz}}$, i.e. the power fluctuations of the bolometer in absence of any incident power during a 1-second averaging window. Previous experiments project NEP values as low as $10^{-21}\,\mathrm{W}/\sqrt{\mathrm{Hz}}$ [140]. The sensitivity of this technique is not limited by quantum fluctuations, but rather by the fundamental thermal fluctuations [45, 128]. This fundamental-fluctuation-limited NEP is given by $\sqrt{4G_{\mathrm{th}}k_{\mathrm{B}}T_0}$ with G_{th} being the thermal conductance of the bolometric material to the thermal bath, and T_0 is the bolometer (bath) temperature. Therefore, bolometers for DA detection will require to operate at the lowest achievable temperatures with the least thermal conductance to its surrounding.

In addition to power detection by bolometer, single-photon detectors (SPD) is another viable option to capture the photons generated from DAs. Efficient DA searches will require the SPD to have simultaneously a high quantum efficiency to register every precious photon, and a low dark count rate to minimize the false positive signal. Naturally, these two requirements are competing against each other because a higher quantum efficiency also means the detector can be triggered by noises to produce a count in the absence of photons. Fortunately at cryogenic temperatures, we can employ superconductors to detect photons efficiently and accurately. When the photon energy is larger than the superconducting gap energy, Δ_{S}, the incident photons can break Cooper pairs and produce a sizable number, $\eta_{\mathrm{d}}\hbar\omega/\Delta_{\mathrm{S}}$, of quasiparticles, with $\eta_{\mathrm{d}} < 1$ being the energy downconversion efficiency [141]. These quasiparticles can then transduce into a readout signal of resistance, temperature, kinetic inductance, or excess current in SPDs such as superconducting nanowire SPD [142, 143], transition edge sensor [144], microbolometer [140, 145], Josephson junction SPD [146], kinetic inductance detector [141], and superconducting tunneling junction detector [147]. SPDs based on this mechanism have been highly successful especially in the near infrared domain when the relatively high photon energy can produce a considerable amount of quasiparticles. Single-photon detection in THz regime is a lot more challenging. Microbolometers based on the superconducting nanowire have demonstrated experimentally energy-resolved, single-photon detection down to 38 THz [145] and projection give energy resolutions as low as 0.12 THz [140]. Recently, quantum capacitance detector [148] has demonstrated the detection of 1.5 THz by sensitively sensing the change of quantum capacitance from the quasiparticle through a resonator.

Since the photon detection mechanism depending on Cooper pair breaking will inevitably become more and more challenging at lower millimeter wave frequencies, we can also exploit the giant thermal response in graphene [132, 149–151] to absorb the incident photon first before measuring the temperature rise. The concept of calorimetric SPDs has been developed for x-ray detection and superconducting SPDs [131, 152]. In contrast to bolometers, single photon detection not strictly limited by thermal fluctuations if a large enough detection bandwidth and high sensitivity temperature transducer is available. Intuitively, this is because when the photon impinges into the detector, SPDs produce a sharp rising signal that can be observed with a wide-bandwidth detector. Quantitatively, this is due to the improvement of signal-to-noise ratio through a matched filter that is tailored to the shape of the expected signal from a single photon. Nevertheless, the energy resolution, $\Delta\epsilon = \sqrt{C_{\mathrm{th}}k_{\mathrm{B}}T_0^2}$ with C_{th} being the thermal heat capacity of the calorimeter, is still a good

JCAP08(2021)066

benchmark for calorimeter SPDs. When the NEP is white-noise limited, we can use [152]

$$\Delta\epsilon = \mathrm{NEP}\sqrt{\frac{C_{\mathrm{th}}}{G_{\mathrm{th}}}} \tag{5.5}$$

to compare the sensitivity with bolometers. For DA searches in wide frequency bandwidth, graphene-based single photon detection also has an advantage in wide bandwidth photon coupling by impedance matching the input to the photon absorber with an antenna. Spiral, log-periodic, and bow-tie antennas have been implemented for graphene detectors [153, 154]. As graphene-based bolometers have been demonstrated recently in the microwave regime [45, 155] with energy resolution projections to a few 10 GHz, it can potentially complement SPDs by operating at millimeter wave frequencies.

In addition to superconductor-based and calorimeter SPD, superconducting qubits and quantum dots can also detect single photons [156, 157]. These nano fabricated devices have discrete energy states and can serve effectively as artificial atoms. When incident photons promote the qubit or quantum dot to an excited state, they can be detected by measuring the state of the artificial atoms. Detection of single photons has been demonstrated using superconducting qubits at microwave frequencies [158, 159] and using quantum dots as low as 1.5 THz [157] with photon coupling through superconducting resonators and dipole antenna, respectively.

Table 7 compares the fundamental limit of detectors that will be useful for dark matter detectors; since the quantum noise rises linearly with frequency, SPDs will have an advantage over amplifiers for the search of higher axion mass [160]. A dark count rate $\lambda_{\mathrm{d}} \sim 1\,\mathrm{mHz}$ has been demostrated experimentally [157, 161] for a quantum dot detector. Note, however, that the realised experimental efficiency for that detector was only $\eta = 0.01$ [157, 161]. Overall, it is desirable to obtain a detector with the optimal combination of low dark count rate and high efficiency, as this will ultimately determine the sensitivity of TOORAD. Detectors that feature a better efficiency typically have a worse dark count rate than the detector from ref. [157] considered above. We will therefore define a pessimistic (optimistic) scenario by setting $\lambda_{\mathrm{d}} \sim 1\,\mathrm{mHz}$ with a detection efficiency of $\eta = 0.01$ ($\eta = 1$).

Last but not least, we shall consider how to put the photon detector together with the material that hosts the AQs. The efficiency of the dark matter search relies on this system integration. The goal is to maximize the photon coupling as the axion quasiparticle material scales up. Therefore we will need to design an antenna that can collect the photons emitted from the AQs to the detector with the least inert loss. This will be an important factor to select a potential detector technology to develop. Ultimately, to detect a small signal from DA, the detector metric should be the total experimental averaging time for an experiment to reach a statistical significance and will depend on both efficiency and sensitivity. To improve our chance of detecting dark matter, we need more research on detector technologies, which are also be useful in other applications including radio astronomy, spectroscopy, and medical imaging [148, 162, 163].

5.3 Experimental sensitivity and forecasts

As discussed above, the signal from the DA-polariton-photon conversion may be detected using an SPD, which is superior compared to heterodyne power detection in THz. In this section we quantify the sensitivity and discovery reach for a photon-counting experiment.

The detection of individual photon events is governed by Poisson statistics i.e. the likelihood of detecting $\mathbb{N}$ photons given model parameters $\boldsymbol{x}$ (the set of DA and material

JCAP08(2021)066

properties) is given by

$$p(\mathbb{N}|\boldsymbol{x}) = \frac{(\eta\, n_\mathrm{s} + n_\mathrm{d})^{\mathbb{N}}}{\mathbb{N}!}\, \mathrm{e}^{-\eta\, n_\mathrm{s} - n_\mathrm{d}}\,, \tag{5.6}$$

where $n_\mathrm{s} = \lambda_\mathrm{s}\tau$ and $n_\mathrm{d} = \lambda_\mathrm{d}\tau$ are the number of expected signal and dark count events, respectively, as calculated from their respective rates, λ_s and λ_d, and total observation time τ. The parameter η describes the total detector efficiency i.e. takes into account the intrinsic efficiency of the detector as well as any other imperfections in the experimental setup. Note that eq. (5.6) assumes that there are no external backgrounds present. While we do not use a likelihood approach based on eq. (5.6) directly for our estimates, it should be noted that the form above is a better approach than the asymptotic, approximate equations used in what follows. For the case of a single-bin Poisson distribution without any nuisance parameters — i.e. assuming that the material and detector properties are perfectly known — we performed a Monte Carlo simulation to check the validity of the asymptotic formulae that we employ. We found them to be conservative and, hence, suitable for the purpose of estimating TOORAD's sensitivity. For an actual analysis of experimental data, however, a likelihood-based approach should be used.

5.3.1 Sensitivity

In order to compute the sensitivity, we assume that no significant signal over background is found. The significance is $S = 2(\sqrt{n_s + n_d} - \sqrt{n_d})$, where n_s is the number of signal events and n_d the number of dark count events [164–166]. Then the exclusion limit at 95% C.L. for photon counting based on Poisson statistics (eq. (5.6)) is obtained from $S < 2$, i.e. $\lambda_\mathrm{s} < \frac{1}{\tau} + 2\sqrt{\frac{\lambda_\mathrm{d}}{\tau}}$, where λ_d is the dark count rate, λ_s the signal rate and τ the measurement time. For a discovery one would require $S > 5$. In section 5.2 we argued that $\lambda_\mathrm{d} = 1\,\mathrm{mHz}$ is reasonable. In the following we estimate the sensitivity in two scenarios. The case $\frac{1}{\tau} < 2\sqrt{\frac{\lambda_\mathrm{d}}{\tau}}$ can be achieved for sufficiently long measurement times and is called the background dominated scenario, i.e. $\tau > \frac{1}{4\lambda_\mathrm{d}} = 250\,\mathrm{s}$. If the measurement time is short $\tau < \frac{1}{4\lambda_\mathrm{d}} = 250\,\mathrm{s}$ then it is not background dominated.

First, we investigate the case that the measurement is not background dominated. The number of signal photons per measurement time is $\lambda_\mathrm{s} = \eta \frac{|E_0|^2}{2\omega} A\, \beta^2$ where A is the surface area of the TMI, η the photon counting efficiency and $\omega = \omega_j \approx \omega_\mathrm{LO}$ is the resonance frequency where the power boost factor peaks. The power boost factor is the emitted electromagnetic field normalized to the axion induced field E_0, which is determined by the local axion dark matter density ρ_a, the axion photon coupling $g_{a\gamma}$ and the strength of the external B-field: $E_0 = g_{a\gamma} B_\mathrm{e} a_0^- \simeq g_{a\gamma} \frac{\sqrt{2\rho_a}}{m_a} B_\mathrm{e}$. Putting everything together we obtain the sensitivity estimate:

$$\begin{aligned} g_{a\gamma} > 4.4 \times 10^{-11}\,\mathrm{GeV}^{-1} &\left(\frac{0.01}{\eta}\right)^{\frac{1}{2}} \left(\frac{2\,\mathrm{T}}{B_\mathrm{e}}\right) \left(\frac{100}{\beta}\right) \left(\frac{(0.2\,\mathrm{m})^2}{A}\right)^{\frac{1}{2}} \left(\frac{4\,\mathrm{min}}{\tau}\right)^{\frac{1}{2}} \\ &\times \left(\frac{0.3\,\frac{\mathrm{GeV}}{\mathrm{cm}^3}}{\rho_a}\right)^{\frac{1}{2}} \left(\frac{m_a}{2.83\,\mathrm{meV}}\right)^{\frac{3}{2}}, \quad \text{(negligible backgrounds, } \tau < \lambda_d^{-1}\text{)} \end{aligned} \tag{5.7}$$

where an axion mass $m_a = 2.83\,\mathrm{meV}$ corresponds to the scanned axion mass with a 2 T external B-field under the assumption of the benchmark material ($n = 5, f_\Theta = 64\,\mathrm{eV}$ and $m_\Theta = 2\,\mathrm{meV}$). The reference area in eq. (5.7), $A = (0.2\,\mathrm{m})$. 0.2 m, is around half of the square de Broglie wavelength for an axion with velocity $v = 10^{-3}c$ and mass 2.83 meV. Single

JCAP08(2021)066

crystals of $MnBi_2Te_4$ grown in ref. [111] are on the order of cm^2. Reaching large surface area will thus require tiling and machining many crystals together. Tiling is known to introduce significant complications for dielectric haloscopes like MADMAX [167, 168]. Further, as the axion gives an opening angle of $v \sim 10^{-3}$ the collecting area of the THz detector must be large. We anticipate that this problem can be overcome with the correct antenna.

When there are finite losses, we can use the peak value from eq. (4.50) to eliminate β and obtain:

$$g_{a\gamma} > 4.95 \times 10^{-11}\,\mathrm{GeV}^{-1} \left(\frac{0.01}{\eta}\right)^{\frac{1}{2}} \left(\frac{2\,\mathrm{T}}{B_\mathrm{e}}\right) \left(\frac{(0.2\,\mathrm{m})^2}{A}\right)^{\frac{1}{2}} \left(\frac{4\,\mathrm{min}}{\tau}\right)^{\frac{1}{2}} \left(\frac{0.3\,\frac{\mathrm{GeV}}{\mathrm{cm}^3}}{\rho_a}\right)^{\frac{1}{2}} \times \left(\frac{2.83\,\mathrm{meV}}{m_a}\right)^{\frac{1}{2}} \left(\frac{\Delta_j}{\pi}\right)^2 \left(\frac{2\,\mathrm{mm}}{d}\right)^2 \times \Sigma, \tag{5.8}$$

where we have defined in the dimensionless quantity:

$$\Sigma \equiv 1 + 2\left(\frac{d}{d_\mathrm{opt}}\right)^3. \tag{5.9}$$

We did not plug in any specific value for Σ in the sensitivity estimate because when the thickness is chosen to be close or equal to the optimal thickness Σ is of the order one. The losses, AQ decay constant, f_Θ, and refractive index, n, all appear implicitly via the determination of d_opt, the optimal material thickness.

Compare the sensitivity eq. (5.8) to that obtained with heterodyne detection. In this case we use the Dicke radiometer equation with noise temperature T. The signal over noise ratio is given by $\mathrm{SNR} = \frac{P_s}{T_\mathrm{sys}}\sqrt{\frac{\tau}{\Delta\nu_a}}$, where $\Delta\nu_a = 10^{-6}\,m_a$ is the DA linewidth, and P_s. If the physical system temperature is low enough, cf. section 5.2, T_sys is limited by the standard quantum limit (SQL) $T_\mathrm{sys} = \omega = m_a$. The resulting sensitivity is:

$$g_{a\gamma} > 1.1 \times 10^{-9}\,\mathrm{GeV}^{-1} \left(\frac{\mathrm{SNR}}{2}\right)^{\frac{1}{2}} \left(\frac{m_a}{2.83\,\mathrm{meV}}\right)^{\frac{7}{4}} \left(\frac{2\,\mathrm{T}}{B_\mathrm{e}}\right) \left(\frac{0.3\,\frac{\mathrm{GeV}}{\mathrm{cm}^3}}{\rho_a}\right)^{\frac{1}{2}} \times \left(\frac{100}{\beta}\right) \left(\frac{(0.2\,\mathrm{m})^2}{A}\right)^{\frac{1}{2}} \left(\frac{4\,\mathrm{min}}{\tau}\right)^{\frac{1}{4}} \quad \text{(heterodyne SQL)}. \tag{5.10}$$

The sensitivity is worse than the SPD, cf. eq. (5.7), by approximately an order of magnitude. This is as expected since for high frequencies the SQL pushes T to large values. The SQL can, however, be overcome by "squeezing" [37].

Next we focus on the case that the measurement is background dominated ($\lambda_\mathrm{s} < 2\sqrt{\frac{\lambda_\mathrm{d}}{\tau}}$). For our benchmark dark count rate of λ_d this gives $\tau > 250\,\mathrm{s}$. Long measurement times on a fixed frequency could be adopted in a "hint" scenario where the axion mass is thought to be known by some other means (for example, an astrophysical hint, or highly accurate relic density prediction), and a resonant DM search is required to verify the hint. To consider this scenario, we take the measurement time on each frequency to be $\tau = 3\,\mathrm{yr}$, i.e. an entire experimental campaign. The sensitivity in this case is:

$$g_{a\gamma} > 1.63 \times 10^{-12}\,\mathrm{GeV}^{-1} \left(\frac{0.01}{\eta}\right)^{\frac{1}{2}} \left(\frac{2\,\mathrm{T}}{B_\mathrm{e}}\right) \left(\frac{100}{\beta}\right) \left(\frac{(0.2\,\mathrm{m})^2}{A}\right)^{\frac{1}{2}} \left(\frac{\lambda_\mathrm{d}}{10^{-3}\,\mathrm{Hz}}\right)^{\frac{1}{4}} \left(\frac{3\,\mathrm{yr}}{\tau}\right)^{\frac{1}{4}} \times \left(\frac{0.3\,\frac{\mathrm{GeV}}{\mathrm{cm}^3}}{\rho_a}\right)^{\frac{1}{2}} \left(\frac{m_a}{2.83\,\mathrm{meV}}\right)^{\frac{3}{2}} \quad \text{(background dominated)}. \tag{5.11}$$

JCAP08(2021)066

Using now again the maximum peak value from eq. (4.43) to eliminate β in the previous equation we obtain the sensitivity estimate

$$g_{a\gamma} > 1.94 \times 10^{-12}\,\mathrm{GeV}^{-1} \left(\frac{0.01}{\eta}\right)^{\frac{1}{2}} \left(\frac{2\,\mathrm{T}}{B_\mathrm{e}}\right) \left(\frac{(0.2\,\mathrm{m})^2}{A}\right)^{\frac{1}{2}} \left(\frac{\lambda_d}{10^{-3}\,\mathrm{Hz}}\right)^{\frac{1}{4}} \left(\frac{3\,\mathrm{yr}}{\tau}\right)^{\frac{1}{4}} \times \left(\frac{0.3\,\frac{\mathrm{GeV}}{\mathrm{cm}^3}}{\rho_a}\right)^{\frac{1}{2}} \left(\frac{2.83\,\mathrm{meV}}{m_a}\right)^{\frac{1}{2}} \left(\frac{\Delta_j}{\pi}\right)^2 \left(\frac{2\,\mathrm{mm}}{d}\right)^2 \times \Sigma\,. \tag{5.12}$$

To complete our discussion we also estimate the sensitivity for bolometric detectors whose performance is specified by the NEP. The minimal detectable signal power which such a detector can detect is $P_s > \mathrm{NEP}/\sqrt{\tau}$. Evaluating this leads to the sensitivity:

$$g_{a\gamma} > 9.7 \times 10^{-13}\,\mathrm{GeV}^{-1} \left(\frac{\mathrm{NEP}}{10^{-21}\mathrm{W}/\sqrt{\mathrm{Hz}}}\right)^{\frac{1}{2}} \left(\frac{(0.2\,\mathrm{m})^2}{A}\right)^{\frac{1}{2}} \left(\frac{3\,\mathrm{yr}}{\tau}\right)^{\frac{1}{4}} \times \left(\frac{m_a}{2.83\,\mathrm{meV}}\right) \left(\frac{0.3\,\frac{\mathrm{GeV}}{\mathrm{cm}^3}}{\rho_a}\right)^{\frac{1}{2}} \left(\frac{100}{\beta}\right) \tag{5.13}$$

The sensitivity estimate in eq. (5.13) has a similar order of magnitude as the SPD sensitivity, cf. eq. (5.11) but a slightly different scaling with the axion mass.

5.3.2 Scanning strategies

We now compute forecasts for the baseline parameters of "Material 2" (best approximation to $Mn_2Bi_2Te_5$, with refractive index $n = 5$ and $\mu = 1$), and consider three possibilities for the losses,[8] $\Gamma_m/\omega = \Gamma_\rho/\omega = 10^{-5}, 10^{-4}, 10^{-3}$.

Assuming a fixed ratio Γ/ω is consistent with our model for the impurity based losses, and assumes ϵ_2 is approximately constant in the relevant range. For fixed ratio Γ/ω, there are larger losses at higher frequencies. We first assumed SPD efficiency of $\eta = 0.01$ and dark count rate $\lambda_d = 10^{-3}\,\mathrm{Hz}$, which has been demonstrated. We also show a more optimistic sensitivity estimate with $\eta = 1$ (dotted line) for $\Gamma_\rho/\omega = \Gamma_m/\omega = 10^{-4}$. The surface area of the TMI layer is fixed to be $A = (0.2\,\mathrm{m})^2$, where 0.2 m is on the order of half of the de Broglie wavelength. Furthermore we use the main resonance $j = 0$ for the sensitivity estimate.

We consider two different scanning scenarios, with B-field values from 1 T to 10 T:

- Scanning I. We begin at the highest frequency with the largest B-field where the base power is largest and the QCD band is at the largest $g_{a\gamma}$. We scan to the top of the QCD band. We then move by the width γ_0 on to the next frequency at lower B, and repeat for a total scan time of 3 years.[9] Figure (20,a). We compute the optimal thickness with the largest axion mass within the scanned region.

[8] Note that we now take into account the frequency scaling of the losses which we have found in section 2.5. In all previous results of this paper we did not take into account this scaling since it was not necessary in order to understand the physical picture. However, here we want to estimate a realistic sensitivity of a DA search and therefore we take the frequency scaling of the losses into account.

[9] Note that we assume the peak power is achieved over the width γ_0. While this is less conservative than assuming the minimal value (i.e., half the maximum), note that power also exists outside of γ_0, which would still be integrated over during the scan. As this is an estimate, rather than a detailed exclusion limit of an experiment, the final limit would likely fall somewhere between the two.

JCAP08(2021)066

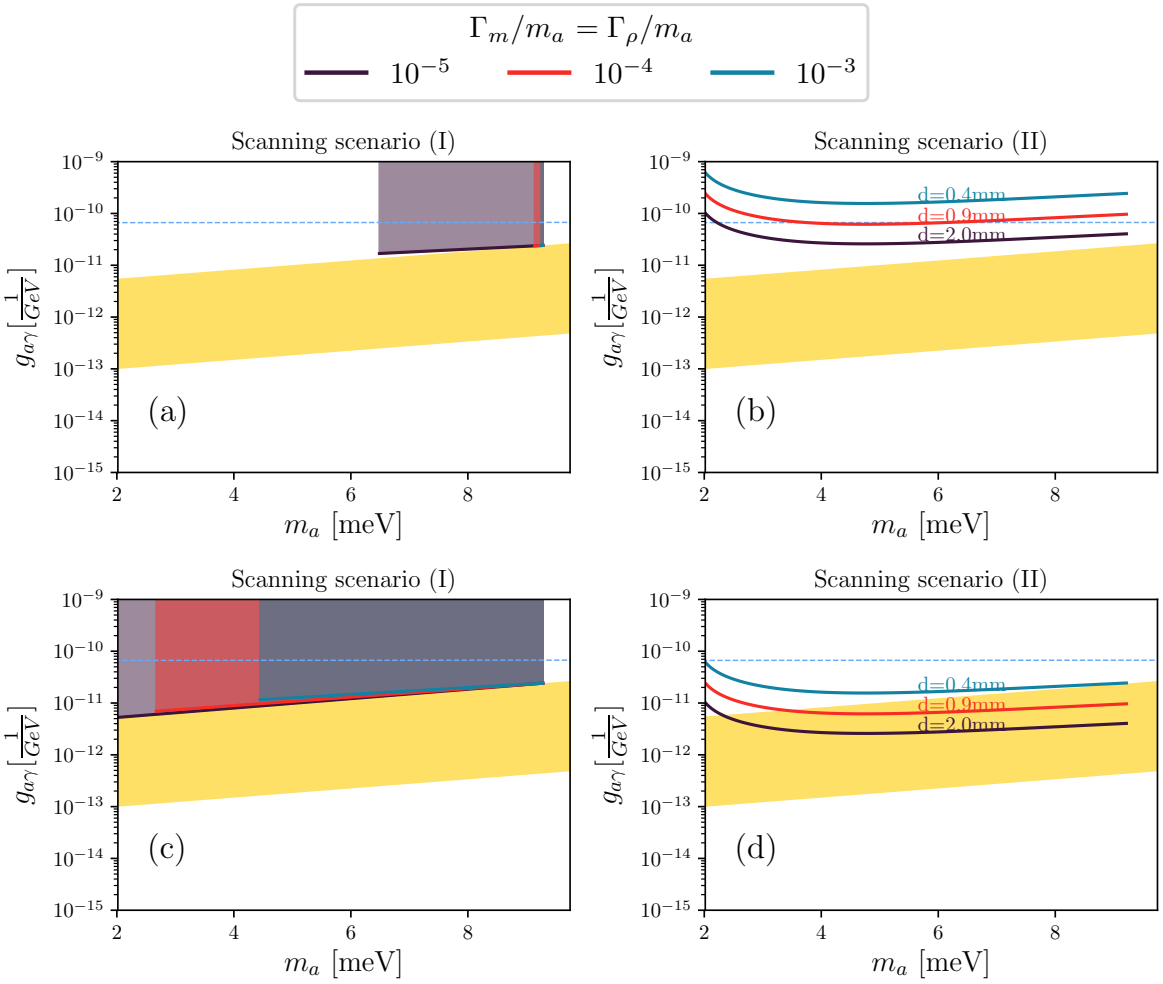

Figure 20. Sensitivity for "Material 2" baseline parameters (see text for details) for various loss values Γ. Top row: $\eta = 0.01$. Bottom row: $\eta = 1$. We fix the dark count rate $\lambda_d = 10^{-3}\,\mathrm{Hz}$. The yellow band shows QCD axion models, and the dashed blue line the CAST exclusion on $g_{a\gamma}$. The scanning scenarios are defined in the text.

- Scanning II. We scan for a fixed time set equal on all frequencies and repeat for a total scan time of 3 years. In each step we move in frequency by the width γ_0, figure 21 (eq. (4.49)). We compute the optimal thickness with the axion mass that is in the middle of the scanned interval.

In each case the limit is found for signal to noise equal to two, 95% C.L. exclusion.

In the Scanning II case we assume that each individual scan takes the same amount of time τ. Then with the bandwidth from eq. (4.49) (figure 21) we can calculate the total number of scans. From this we then calculate the scan time for each individual scan such that the total scanning time for each case is $t_{\mathrm{scan}} = 3\,\mathrm{years}$. Depending on the individual scan time τ we calculate the sensitivity in the right limit, cf. eq. (5.8) and (5.12).

In the Scanning I scenario for $\eta = 0.01$, we find that a wide range of the QCD band can only be covered in the case with extremely small losses, $\Gamma/\omega = 10^{-5}$. With this scanning strategy, $\eta = 1$ detection efficiency allows a wide range of the top of QCD band to be scanned

JCAP08(2021)066

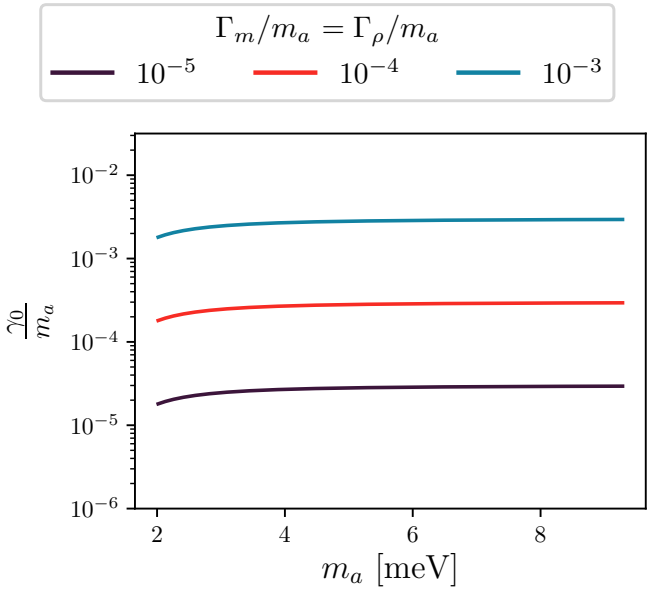

Figure 21. Linewidth of the boost parameter for "Material 2" baseline parameters (see text for details) for various loss values Γ.

for all loss parameters. In the Scanning II scenario the QCD band cannot be reached with $\eta = 0.01$. However, with $\eta = 1$ we find that a reasonable portion of the upper part of the QCD band can be scanned with $\Gamma/\omega = 10^{-4}$. With very low losses $\Gamma/\omega = 10^{-5}$ and $\eta = 1$ the Scanning II scenario reaches almost KSVZ sensitivity across a wide range of masses. We also considered the intermediate case $\eta = 0.1$, which allows some sensitivity to the QCD axion band with $\Gamma/\omega = 10^{-4}$. We conclude that a successful QCD-sensitive experiment requires high efficiency SPDs.

5.4 Parameter study

We now wish to investigate how the sensitivity and scan range depend on the yet unknown material parameters of the TMIs. In this section we consider only the scanning II scenario. In table 8 we list the unknown parameters, and reasonable ranges they might take in different materials within our rough approximations to the theoretical uncertainties. The ranges for the parameters have been motivated in section 2.4.

In figure 22 we study the effect of varying the AQ decay constant f_Θ and the refractive index n on the scan range and sensitivity (we do not vary the AQ mass, since this has the trivial effect of changing the lower limit of the scan range). The sensitivity and other parameters are fixed as described in the previous subsection. Let us first discuss the scanning range. The smaller n and f_Θ the larger is the axion mass range that can be probed. This is because the upper range of the scanned axion mass is determined by eq. (5.1).

To understand the effect of n and f_Θ on the sensitivity, it is enlightening to study the behaviour of the sensitivity estimates in the limit that the external B-field is very large, i.e. $m_a \approx \omega_{\mathrm{LO}} \approx b \sim \frac{B_e}{n f_\Theta}$. Both sensitivity estimates in the background dominated, cf. eq. (5.11), and in the non-background dominated limit, cf. eq. (5.8), are proportional to $g_{a\gamma} \sim \frac{1}{B_e}\frac{1}{d_{\mathrm{opt}}^2}$,

JCAP08(2021)066

Parameter name & symbol		Range	Benchmark
TMI parameters			
Decay constant	f_Θ	$[50,\ 200]\,\mathrm{eV}$	$70\,\mathrm{eV}$
AQ mass	m_Θ	$\sim \mathcal{O}(\mathrm{meV})$	$1.8\,\mathrm{meV}$
Permittivity	ϵ	[9,49]	25
Magnetic permeability	μ	$\sim \mathcal{O}(1)$	1
Magnon losses	Γ_m	$[10^{-5},\ 10^{-3}]\,\mathrm{meV}$	
Specific conductance	Γ_ρ	$[10^{-5},\ 10^{-3}]\,\mathrm{meV}$	
Area of crystal face	A	$(0.2\,\mathrm{m})^2$	
Thickness	d	d_{opt}, cf. eq. (4.51)	
Experimental parameters			
External B-field	B_e	$[1,\ 10]\,\mathrm{T}$	$2\,\mathrm{T}$
Detection effciency	η	[0.01, 1]	0.01
Dark count rate	λ_d	$\gtrsim 1\,\mathrm{mHz}$	$1\,\mathrm{mHz}$

Table 8. Parameter reference values and ranges. Our benchmark material is "Material 2", based on $Mn_2Bi_2Te_5$.

where we have assumed that Σ does not vary too much.[10] Plugging in the optimal thickness we obtain the scaling behaviour:

$$g_{a\gamma} \sim \left(\frac{1}{B_e}\right)^{\frac{1}{6}} \left(\frac{1}{f_\Theta}\right)^{\frac{5}{6}} \sqrt{n}. \tag{5.14}$$

The strongest scaling is induced by the AQ decay constant f_Θ. This view is also confirmed by the plots in figure 22. However increasing f_Θ also leads to a smaller scanning interval such that the reached $C_{a\gamma}$ in the QCD band is almost constant. The refractive index n enters in the sensitivity only weakly with a square root dependence. However for fixed f_Θ it is visible from the plots in figure 22 that decreasing n gives a slightly better limit on the DA-photon coupling. Furthermore, the scaling in eq. (5.14) only applies so long as the approximation $m_a \approx \omega_{\mathrm{LO}} \approx b \sim \frac{B_e}{n f_\Theta}$ holds. At large f_Θ this approximation breaks down for suitable values of B_e (either the experimental maximum, or spin flop field, whichever is lower).

With these effects in mind, we revisit the candidate AQ material $(Bi_{1-x}Fe_x)_2Se_3$ ("Material 1"), considered in Paper I. We estimate that this material has slightly smaller f_Θ, and will thus have a slightly worse sensitivity to $g_{a\gamma}$ than the alternative Material 2, although it will have a narrower possible scan range. To be more optimistic with Material 1, we adopt $n = 3$ for presentation (although this has a very small effect). Our results are collected in figure 23.[11]

[10] Remember that Σ would be exactly 3, if we would choose for each axion mass that is scanned the exact optimal thickness. However, in a scanning scenario this will for practical reasons not be possible and we choose d to be the optimal thickness that corresponds to the axion mass that is in the center of all axion masses that are scanned. As a consequence Σ can also be slightly larger than 3 in the whole axion mass that is being scanned.

[11] Appendix B gives more details about the QCD axion model assumptions indicated in this figure.

JCAP08(2021)066

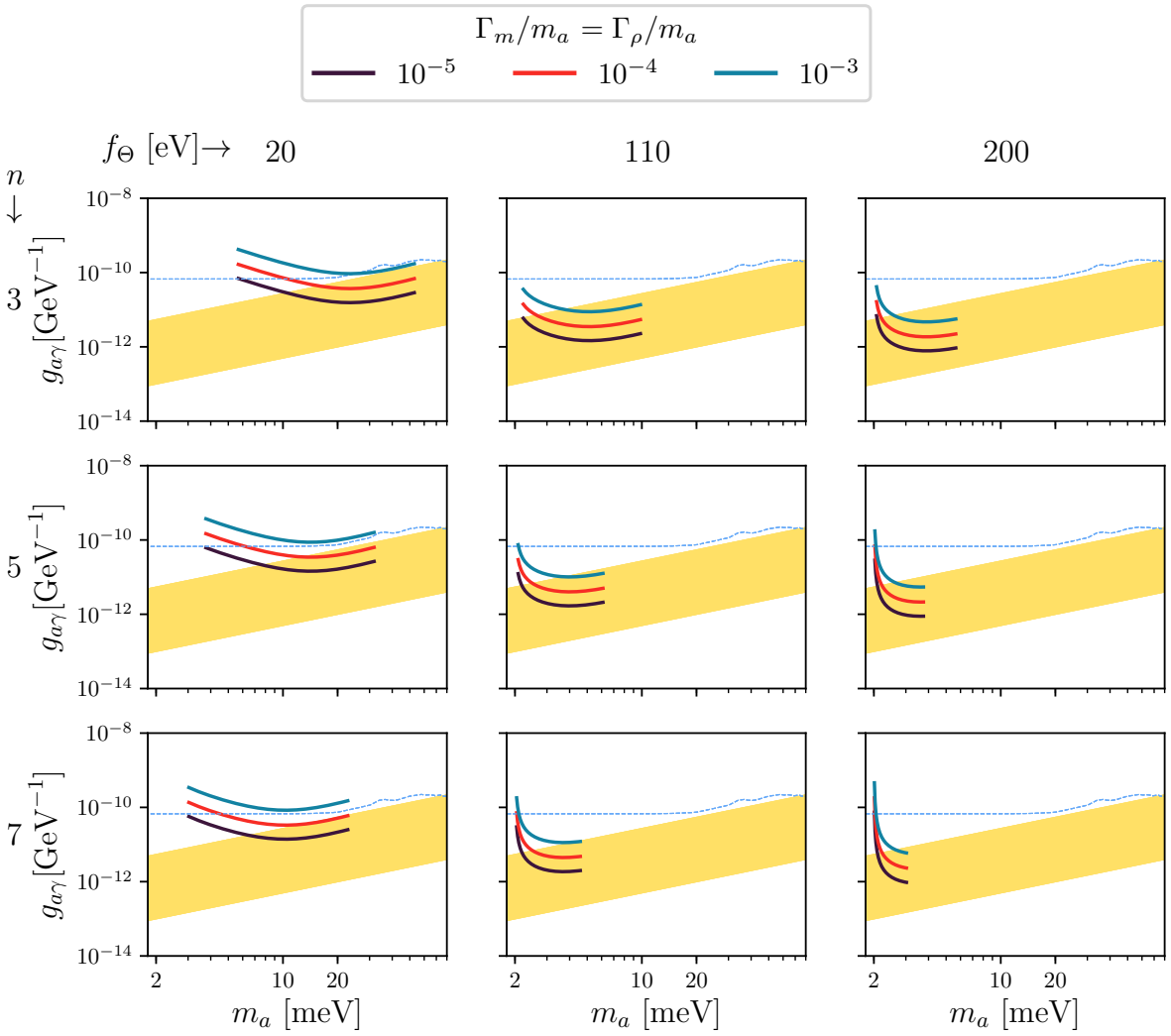

Figure 22. Sensitivity estimate for the DA-photon coupling $g_{a\gamma}$ varying the external B-field from 1 T to 10 T. The surface area is fixed to $A = (0.2\,\mathrm{m})^2$. The thickness d is set to the optimal thickness, cf. eq. (4.51). We assume each frequency is scanned for the same amount of time, and the total scanning time is $t_{\mathrm{scan}} = 3\,\mathrm{years}$. For the detector $n_b = 10^{-3}\,\mathrm{Hz}$ and efficiency $\eta = 1$. The yellow band represents the QCD band with $C_{a\gamma} = 12.75 \cdots 0.25$, cf. eq. (B.3) for the definition of $C_{a\gamma}$. The dashed blue line shows the CAST limit.

JCAP08(2021)066

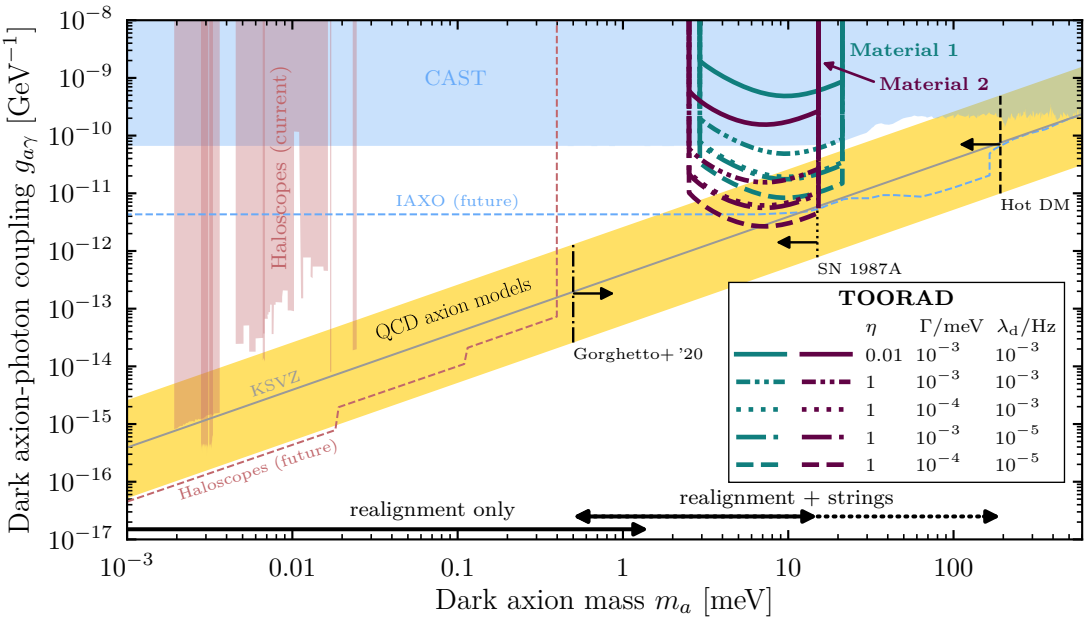

Figure 23. The projected TOORAD sensitivity for Material 1 [$(Bi_{1-x}Fe_x)_2Se_3$-inspired] and Material 2 ($Mn_2Bi_2Te_5$-inspired) for different losses and detector sensitivities. See table 8 for all other benchmark parameter values. We show limits and forecasts [169] for CAST [170, 171], IAXO [172], and various haloscopes [31, 37, 168, 173–180] (for $\rho_{\rm loc} = 0.3\,{\rm GeV/cm^3}$) as well as the bounds from hot dark matter constraints [181], energy loss arguments in SN1987A [13]. The preferred regions cold dark matter [182] in the realignment scenario, and with the latest cosmic string decay calculations [183] are also indicated as horizontal arrows. The QCD axion band encompasses all "preferred" KSVZ-type axion models as defined in ref. [29], in addition to the original KSVZ and DFSZ models.

JCAP08(2021)066

6 Discussion and conclusions

6.1 Summary of results

The present work has developed the theory of axion quasiparticles in topological magnetic insulators, and how such materials can be used to detect axion dark matter.

Model of axion quasiparticles. We first presented in some detail the symmetry criteria for the existence of axion quasiparticles, and the Dirac model for their realisation in topological magnetic insulators. While already known in the literature (e.g. refs. [42, 43, 50, 51]), these have not been shown in detail in relation to axion DM, and provide important background to the subsequent results. We laid out carefully the symmetry criteria necessary for a material to posses an AQ. Our exploration of the model sheds light on the nature of the AQ as a longitudinal magnon, i.e. a spatially and temporally varying AF spin fluctuation. It is non-linearly related to the transverse magnons of ordinary AFMR.

In order to estimate the parameters f_Θ and m_Θ of the model, we used the result of the *ab initio* calculation given in ref. [42] for $(Bi_{1-x}Fe_x)_2Se_3$ on a cubic lattice. We rescaled the results to use updated values of the material parameters of $(Bi_{1-x}Fe_x)_2Se_3$, and $Mn_2Bi_2Te_5$, for which there is not a result available in the literature. More accurate *ab initio* calculations of the parameters for both $(Bi_{1-x}Fe_x)_2Se_3$ and $Mn_2Bi_2Te_5$ are highly desirable. We considered multiple possible sources of loss in these materials, and attempted to estimate the contributions to the polariton linewidth. This often involved extrapolation of results obtained at different frequencies and only measured in related materials. Direct spectroscopic measurement of all these parameters is thus necessary.

Axion quasiparticle detection. We computed explicitly the transmission function of AQ materials. This transmission function displays a magnetic field-dependent gap, and a series of resonances, which depend on the size of the loss terms. By measuring the frequency of the upper and lower ends of this gap, and the linewidths of the resonances, one could determine the parameters of the model directly. Furthermore, the gap in the polariton spectrum, and the scaling of the gap size with field strength, demonstrate directly the existence of the AQ and its coupling to the electromagnetic field via a Chern-Simons interaction. Thus, THz transmission spectroscopy can be used to discover the AQ.

The considered material candidates that can host an AQ are all antiferromagnets. Antiferromagnets exhibit an antiferromagnetic resonance (AFMR) with typical resonance frequencies in the THz regime. This raises the question how one can distinguish the AFMR from the axion-polariton resonance in the transmission spectrum. It is well known how the AFMR frequency scales with a non-zero external B-field [125, 184, 185]. This scaling is distinct from that of the axion-polariton resonance, which consists of a fixed resonance at m_Θ, and a second one near $\omega_{\text{LO}} = \sqrt{m_\Theta^2 + b_0^2(B/B_0)^2}$ (where $b_0 = b(B_0)$ and B_0 is a reference scale). We expect transmission spectra of the AF axion insulator $MnBi_2Te_4$ to show the single AFMR, while the AQ material $Mn_2Bi_2Te_5$ will show both the axion polariton resonances and AFMR. Comparing results for both materials and the B-field dependence will help isolate the effect of the AQ.

Axion dark matter detection. We developed the computation of the power output of an AQ material in the presence of axion DM. The system bears many similarities to dielectric and plasma haloscopes, and is characterised by a boost amplitude, $\beta(\omega)$. The boost amplitude increases with thicker sample sizes, and the height and width of the boost are affected by

JCAP08(2021)066

magnon and photon losses. The power is amplified by β^2 compared to a magnetized mirror, and for realistic models of the loss $10^2 \lesssim \beta^2 \lesssim 10^3$ with a bandwidth of order 10^{-4} to 10^{-3}.

Figure 23 shows our best estimates for the discovery potential of TOORAD compared to other constraints on axion dark matter, and proposals for future experiments. The present best estimate shows that TOORAD, using a material similar to $Mn_2Bi_2Te_5$ could scan an $\mathcal{O}(1)$ range in the upper half of the QCD axion model band if the SPD efficiency is very good, $\eta \approx 1$. In the best case scenario with low dark count rate detectors the KSVZ band can be reached.

The primary difference between the two material candidates considered lies in the estimated value of f_Θ, with slightly higher values being favourable in the scan depth, but having a slightly narrower total range. If the spin flop transition of the material is lower than the maximum 10 T field assumed, then the scans would begin at lower frequencies, and span a slightly smaller range of masses.

6.2 Discussion

Comparison to other axion detection proposals. We have considered detecting the dark matter axion via the axion-photon coupling, $g_{a\gamma}$, combined with the mixing between the photon and the AQ. It is interesting to note that if the dark matter axion also possess a coupling to electrons, g_{ae}, then this can excite AFMR in the TMI via the "axion wind" derivative interaction [186] (this interaction has been successfully constrained with nuclear magnetic resonance [187] and ferromagnetic resonance [40, 188]). The AFMR axion wind interaction opens the possibility that AQ materials could measure both couplings, $g_{a\gamma}$ and g_{ae}, with the same material by tuning to different resonant modes. This could be used to perform model discrimination between the KSVZ model, with loop suppressed electron coupling, and the DFSZ model, with leading order electron coupling. This would be an interesting line of future research.

Similarly to dielectric and plasma haloscopes, TOORAD aims to avoid the Compton wavelength limits imposed in traditional cylindrical cavities. Most experiments try to avoid this limit through breaking translation invariance on roughly half Compton wavelength scales. Examples include dielectric haloscopes [33] like MADMAX [189] and LAMPOST [190], multicavity arrays [191, 192] such as RADES [35, 193] and hybrid approaches using dielectric loaded resonators [194, 195] such as Orpheus [196]. In contrast, TOORAD aims to give the photon an effective mass (in the low spin wave momentum limit). In this sense, the most similar analogue in axion experimental design is a plasma haloscope [179], which directly gives the photon a mass in the form of a plasma frequency.

The THz regime represents a unique challenge for axion detection, as it represents an intermediate regime between scales and technologies. Dielectric haloscopes have been proposed at lower [189] and higher [190] frequencies. THz represents a middle ground between the use of discrete, movable disks and $\mathcal{O}(1000)$ layer deposited thin films implying unique engineering challenges to cover the available parameter space.

Dish antennas [30] are the simplest structure to target THz, due to their broadband nature, however they lack resonant enhancement that could allow a more targeted search at higher signal to noise. Currently the only proposed dish antenna in this range is BRASS [197].

A more recent idea in the meV range is to use the axion's coupling to phonon polaritons or magnons [198], however the resonance frequency in this proposal is not easily tuned, which makes scanning axion masses difficult. To cover a range of axion masses, different materials

JCAP08(2021)066

of high quality would need to be measured. Further, the single quanta measurement of such particles remains challenging [198].

As the field of THz axion detection is still very young, and each approach has different material or engineering challenges, it is important to have a wide range of ideas in order have a chance to look in this well motivated, but very difficult, parameter space.

Materials science. In terms of material research we have revealed there is a stark contrast between conventional strong dynamical axion response in solids and dynamical axion quasiparticle response suitable for DM detection discussed here.

- The axion quasiparticles for DM detection favour longitudinal spin waves with linear coupling to photons. In contrast, the heterogeneous dynamical axion field present in the chiral magnetic effect or antiferromagnetic resonance of the standard transversal spin modes does not provide within minimal models for such a coupling [43].
- While conventional large axion response can be achieved close to the magnetic phase transition [43], a DM search favours lower temperatures, ensuring sharper resonance linewidth free of thermal and scattering disorder.
- The static quantised axion insulators are protected by axion odd symmetries such as spatial inversion (parity). Our dynamical axion quasiparticles favour $\mathcal{PT}$ symmetric systems: $\mathcal{PT}$ allows for Dirac quasiparticles enhancing the (dynamical) nonquantized AQ response by allowing tunability close to the topological phase transition.

Antiferromagnetism is favourable in many ways for axion DM detection. Reasons for this include its compatibility with tunable axionic Dirac quasiparticles [66], availability of semiconducting band-structure with potentially large band-gaps, high critical temperatures, and large spin-flop fields. Furthermore, multi-sublattice systems can provide for a combination of separated heavy atomic elements with strong spin-orbit interaction and lighter magnetic elements.

Materials wishlist. We close with stating the desirable properties of an AQ material for axion DM detection.

- Longitudinal spin wave mass, m_Θ, in the meV range. The goal is to detect the QCD axion in this mass range. With much smaller m_Θ there are already existing technologies, while for much larger values the QCD axion is already excluded.
- Decay constant, f_Θ, in the 10 to 100 eV range.[12] For f_Θ much larger than 100 eV the AQ is not strongly coupled enough to the Θ term for efficient mixing. Another way to express this requirement is that the polariton gap for fields of order 1 T should be of order m_Θ.
- Low refractive index ($n \lesssim 5$) and high resistivity ($\rho > 10^3$ meV^{-1}) in THz, preferably measured from the axion-polariton spectrum resonance.
- Low impurity density: impurity separation scale of microns or larger.
- High spin flop field. This should definitely exceed 1 T for sufficiently large power output. Larger spin flop fields permit a wider scan range.

[12] Recall that in the Dirac model $f_\Theta^2 = 2M_0^2 J$ where M_0 is the bandgap and J is the spin wave stiffness.

JCAP08(2021)066

- High Néel temperature. The experiment can be operated in a dilution refrigerator with $T \ll 4$ K. However, the further this is below the Néel temperature, the better, since we expect magnon losses to decrease for $T \ll T_N$.

- Ability to manufacture samples with thickness in excess of 1 mm. Ultimately one must also machine multiple samples together into a large surface area disk.

We have shown that, with plausible assumptions, $Mn_2Bi_2Te_5$ and $(Bi_{1-x}Fe_x)_2Se_3$ both satisfy many of these requirements, although we expect the AQ phase of $Mn_2Bi_2Te_5$ to be more stable, since it does not require magnetic doping. If it can be proven that any material satisfies the above requirements, then, in combination with existing detector and magnet technology, such a material can be used to make an effective search for axion dark matter in the theoretically well-motivated mass range near 1 meV.

Acknowledgments

We thank Bobby Acharya, Caterina Braggio, Nicolò Crescini, Matthew Lawson, Erik Lentz, Chang Liu, Eduardo Neto, Naomi Nimubona, Alireza Qaiumzadeh, Andreas Ringwald, and David Tong for useful discussions. DJEM, SH, and MA are supported by the Alexander von Humboldt Foundation and the German Federal Ministry of Education and Research. JSE is supported through Germany's ExcellenceStrategy — EXC 2121 "Quantum Universe" — 390833306. KCF was supported in part by Army Research Office under Cooperative Agreement Number W911NF-17-1-0574. FC-D is supported by STFC grant ST/P001246/1, Stephen Hawking Fellowship EP/T01668X/1. EH is supported by STFC grant ST/T000988/1. AM is supported by the European Research Council under Grant No. 742104 and by the Swedish Research Council (VR) under Dnr 2019-02337 "Detecting Axion Dark Matter In The Sky And In The Lab (AxionDM)". AS is supported by the Special Postdoctoral Researcher Program of RIKEN. LS acknowledges the EU FET Open RIA Grant No. 766566, the Elasto-Q-Mat (DFG SFB TRR 288), Czech Science Foundation Grant No. 19-28375X, and Sino-German DFG project DISTOMAT.

A Antiferromagnetic resonance and magnons for particle physicists

A.1 Effective field theory of AFMR

We follow refs. [122, 199], and present the effective field theory of antiferromagnetic resonance (EFT of AFMR), which we believe is illuminating, especially from a particle physics perspective.

The EFT of AFMR considers the dynamics of the AF magnetization $\boldsymbol{n}$ considered as a field in the continuum limit of the Heisenberg model of the magnetic lattice, which is equivalent to the Hubbard model in the half-filling limit, as discussed in section 2.4. The magnetic lattice consists of A sites and B sites, with spins $\boldsymbol{S}_A$ and $\boldsymbol{S}_B$ at each site, and $\boldsymbol{n} = (\boldsymbol{S}_A - \boldsymbol{S}_B)/2$. The symmetry group $G = \mathrm{SO}(3)$ is related to the internal rotations of $\boldsymbol{n}$ (not spatial rotations). This symmetry is broken by the groundstate AF order, $\langle \boldsymbol{n} \rangle = (\langle \boldsymbol{S}_A \rangle - \langle \boldsymbol{S}_B \rangle)/2$ (which can be normalised to unity) and is invariant under the group $H = \mathrm{SO}(2)$ of rotations about the axis. Magnetic order implies that the groundstate breaks time translation invariance, $\mathcal{T}$, which flips the spin orientations. However, the groundstate preserves an effective time translation invariance $\widetilde{\mathcal{T}} = \mathcal{T}\mathcal{S}$, where $\mathcal{S}$ swaps the A lattice sites

JCAP08(2021)066

for the B lattice sites. This leads, as we shall see, to a "relativistic" dispersion relation for AF spin waves. Spin-orbit effects (finite electron mass corrections) lead to explicit breaking of SO(3), which can be considered as a perturbation, and leads to a preferred "easy axis" related to a direction in the crystal lattice.

The Lagrangian for fluctuations in $\boldsymbol{n}$ must be invariant under the coset space G/H, which has the symmetry group of rotations on the surface of the two-sphere, S^2, and imposes the restriction $\boldsymbol{n} \cdot \boldsymbol{n} = 1$. This restriction can be imposed as a constraint and expanded for small perturbations in Cartesian coordinates for $\boldsymbol{n}$, which is sufficient to derive the normal modes and dispersion relation. More generally, the constraint can be imposed by the correct choice of coordinates and metric, in this case the SO(3) invariant metric on S^2, and leads to the full non-linear model in polar coordinates. We begin with the first case, since we can align the coordinates with the spacetime directions and arrive at well known results quickly, while the second case is illuminating since it preserves the symmetries manifestly, and leads to insights into the nature of the longitudinal mode.

A.1.1 AFMR in Cartesian coordinates

The Lagrangian at leading order in derivatives is:

$$\mathcal{L} = \frac{F_1^2}{2}\dot{\boldsymbol{n}} \cdot \dot{\boldsymbol{n}} - \frac{F_2^2}{2}\nabla \boldsymbol{n} \cdot \nabla \boldsymbol{n}\,, \tag{A.1}$$

where F_1^2 is the spin wave stiffness, and $F_2^2 = v^2 F_1^2$ with v the spin wave speed. The external fields are the applied field, $\boldsymbol{H}_0$, the probe photon with fields $\boldsymbol{E}_\gamma$, $\boldsymbol{H}_\gamma$ and wavevector $\boldsymbol{k}_\gamma$, and the anisotropy field, $\boldsymbol{H}_A$, which defines the easy-axis in the material. In the simplest AFMR geometry we consider the applied field to be parallel to the z-axis, which is also parallel to the anisotropy field. We further consider the probe photon (RF-field) moving along the positive z-axis, polarised in the y-direction. The fields are thus:

$$\begin{aligned}
\boldsymbol{k}_\gamma &= (0, 0, k)\,, \\
\boldsymbol{H}_\gamma &= (H_\gamma, 0, 0)\,, \\
\boldsymbol{E}_\gamma &= (0, E_\gamma, 0)\,, \\
\boldsymbol{H}_0 &= (0, 0, H_0)\,, \\
\boldsymbol{H}_A &= (0, 0, H_A)\,.
\end{aligned} \tag{A.2}$$

For ordinary AFMR, the photon electric field is decoupled from the system.

The applied field H_0 and the photon magnetic field are coupled into the Lagrangian eq. (A.1) by replacing the derivatives with SO(3) $\cong$ SU(2) covariant derivatives:

$$\partial_\mu n_a \to D_\mu n_a = \partial_\mu n_a + \epsilon_{abc} f_{\mu b} n_c\,, \tag{A.3}$$

where n_a are the directions in the SO(3) group space, $\mu = 0, 1, 2, 3$ as subscript is the spacetime index (which should not be confused with the Bohr magneton μ_B), ϵ_{abc} is the antisymmetric symbol in three dimensions with $\epsilon_{123} = 1$ (i.e. the structure constants of SU(2)), and $f_{\mu b}$ is the applied field. For an applied magnetic field we have $\mu_B H_i = f_{0i}$ which allows us to relate the group space index a to the spacetime axis $i = 1, 2, 3$. At lowest order in the applied fields, this result can be understood by appealing to the interaction Lagrangian:

$$\begin{aligned}
\mathcal{L}_{\text{em}} &= -\mu_B \boldsymbol{s} \cdot \boldsymbol{H}\,, \quad \boldsymbol{s} = F_1^2(\dot{\boldsymbol{n}} \times \boldsymbol{n})\,, \\
\Rightarrow \mathcal{L}_{\text{em}} &= \mu_B F_1^2 \epsilon_{ijk} \dot{n}_i H_j n_k\,,
\end{aligned} \tag{A.4}$$

where the spin density $\boldsymbol{s}$ follows from the leading order term in the derivative expansion of the Noether current due to the SO(3) invariance.

The anisotropy field is included in the Lagrangian via a perturbation of the form $\Delta\mathcal{L} = \mathcal{O}^a n_a$ and for our field geometry is given by:

$$\Delta\mathcal{L} = \mu_B \Sigma_s H_A n_3 \tag{A.5}$$

where $\Sigma_s = S/V_{\text{u.c.}}$ is the "staggered magnetization", $(S_A - S_B)/2$, in the unit cell.

In order to derive the dispersion relation (the propagator), we only require the quadratic Lagrangian. Anticipating the well-known Keffer-Kittel result for the AFMR polarisations [184] we use n_1 and n_2 as coordinates, and Taylor expand for small n_3 using the constraint, i.e. $n_3 = (1 - n_1^2 - n_2^2)^{1/2}$. Momentum conservation demands that $\boldsymbol{k} = \boldsymbol{k}_\gamma$, and with the given geometry this simplifies the problem to effectively one-dimensional along the $z(3)$-axis. After some basic algebra, the quadratic Lagrangian is found to be:

$$\begin{aligned}\mathcal{L} = &\frac{F_1^2}{2}\left[\dot{n}_1^2 + \dot{n}_2^2\right] - \frac{F_2^2}{2}\left[(\partial_z n_1)^2 + (\partial_z n_2)^2\right] \\ &- F_1^2 \mu_B H_\gamma [\dot{n}_2 + \mu_B H_0 n_1] + F_1^2 \mu_B H_0 [\dot{n}_2 n_1 - \dot{n}_1 n_2 + \mu_B H_0 (n_1^2 + n_2^2)] - \frac{\mu_B \Sigma_s H_A}{2}(n_1^2 + n_2^2)\,.\end{aligned} \tag{A.6}$$

The first line is the kinetic term, and the second line includes the effects of the external fields. The photon field has been considered a perturbation, and thus couples linearly to the fields n_i in the Lagrangian. The photon field thus acts as an oscillating source term in the equations of motion. On the other hand H_0 and H_A couple to quadratic combinations of n_i, and affect the dispersion relation.

The equations of motion are:

$$\ddot{n}_1 - 2\mu_B H_0 \dot{n}_2 + \left(v^2 k^2 + \frac{\mu_B \Sigma_s H_A}{F_1^2} - \mu_B^2 H_0^2\right) n_1 = \mu_B^2 H_\gamma H_0\,, \tag{A.7}$$

$$\ddot{n}_2 - 2\mu_B H_0 \dot{n}_1 + \left(v^2 k^2 + \frac{\mu_B \Sigma_s H_A}{F_1^2} - \mu_B^2 H_0^2\right) n_2 = \mu_B \dot{H}_\gamma\,. \tag{A.8}$$

To derive the dispersion relation, we consider the homogeneous equation with the right hand side set equal to zero, and move to frequency space by Fourier transforming $t \to \omega$. The system is diagonalised by the complex fields $n_\pm = n_1 \pm i n_2$ leading to the system:

$$\omega_\pm^2 \mp 2\mu_B H_0 \omega_\pm - \left(v^2 k^2 + \frac{\mu_B \Sigma_s H_A}{F_1^2} - \mu_B^2 H_0^2\right) = 0\,, \tag{A.9}$$

which is solved by

$$\begin{aligned}\omega_+ &= \mu_B H_0 \pm \sqrt{v^2 k^2 + \frac{\mu_B \Sigma_s H_A}{F_1^2}}\,, \\ \omega_- &= -\mu_B H_0 \pm \sqrt{v^2 k^2 + \frac{\mu_B \Sigma_s H_A}{F_1^2}}\,.\end{aligned} \tag{A.10}$$

The dispersion relation, eq. (A.10) for the fields $n_\pm = n_1 \pm i n_2$ displays all the well-known properties of AFMR. The two modes $n_\pm = n_1 \pm i n_2$ correspond to clockwise and anticlockwise precession of the Néel vector [184]. The resulting spin wave is depicted in figure 24. The constraint $|\boldsymbol{n}|^2 = 1$ leads to an oscillation of n_3 accompanying the precession.

JCAP08(2021)066

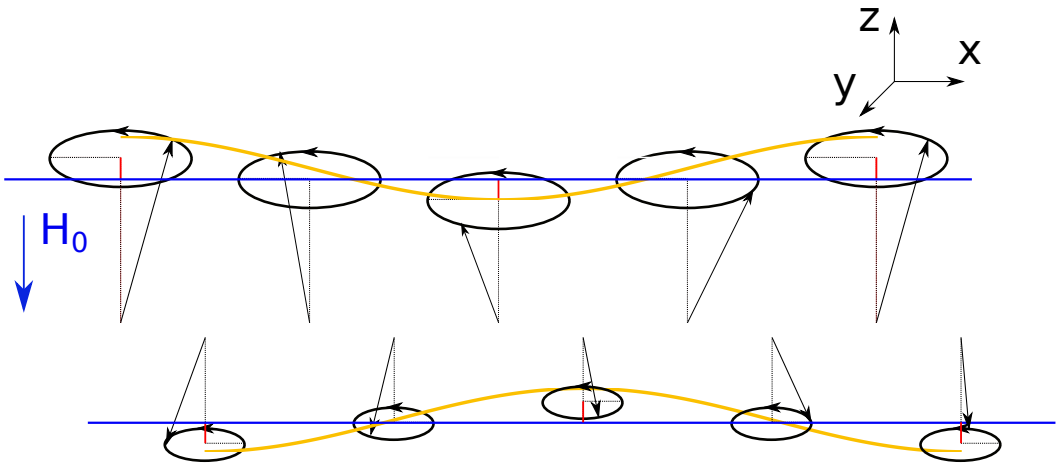

Figure 24. AFMR spin wave, with $|\boldsymbol{n}|^2 = 1$, indicating the higher order change in n_3 associated with the spin precession.

As shown in appendix A.2, n_3 in this case oscillates with a frequency twice that of the AFMR. However, if $|\boldsymbol{n}|^2 = 1$, then n_3 in not an independent polarisation and its fluctuation does not change the length of the Néel vector.

In the absence of H_A, the dispersion relation is linear in k. The application of H_A induces a "mass term", i.e. a term inducing a gap and leading order quadratic piece in the dispersion relation near $k = 0$:

$$m_s^2 = \frac{\mu_B \Sigma_s H_A}{F_1^2} \tag{A.11}$$

Rearranging, we find

$$m_s^2 F_1^2 = \mu_B \Sigma_s H_A \,, \tag{A.12}$$

which has the form $m_s^2 F_1^2 =$ (spontaneous) $\times$ (explicit) symmetry breaking, and is the AF analogue of the Gell-Mann-Oakes-Renner relation [109] for pions [122] (and also the QCD axion). Furthermore, since $F_1^2 \propto \Sigma_s$ this fits with the microscopic interpretation of F_1^2 as arising from the staggered magnetization angular momentum per unit cell mentioned above.

The applied field H_0, rather than leading to a mass term, instead induces a linear shift in the frequency, the "Kittel shift", which arises from an effective (anti-)damping term and "negative mass squared" in the equations of motion for $n_\pm$.

The exchange field, H_E, is not incorporated directly in our treatment of EFT. However, as noted in ref. [122], we should fix the EFT parameters with reference to a microscopic theory. The microscopic theory (e.g. ref. [200]) gives the spin wave mass from the energy gap:

$$m_s^2 = \mu_B^2 H_A (2H_E + H_A) \,, \tag{A.13}$$

where H_E is the exchange (or Weiss) field. The second term of eq. (A.13) is not present in the EFT, which is linear in H_A. Indeed, EFT is valid in the limit $H_A/H_E \ll 1$, and breaks down for large anisotropy fields [122]. Comparing eq. (A.12) with the first term of eq. (A.13) we identify $H_E = \Sigma_s / 2\mu_B F_1^2$ leading to:

$$F_1^2 = \frac{\Sigma_s}{\mu_B H_E} = \frac{S}{\mu_B H_E V_{\text{u.c.}}} \,. \tag{A.14}$$

JCAP08(2021)066

The EFT of AFMR is based on the mean field Heisenberg model. The Heisenberg model is the strong coupling limit of the Hubbard model (the fundamental model on which our theory of the AQ is based), with different perturbative degrees of freedom. In the Heisenberg model with nearest neighbour interactions the Hamiltonian is:

$$H = J_H \sum_{<ij>} \sigma_i \cdot \sigma_j - D \sum_i (\sigma_i^z)^2 \tag{A.15}$$

where the first sum is over the spins σ_i and σ_j on adjacent lattice sites. The anisotropy field is given by $H_A = \frac{2SD}{g\mu_B}$. The anisotropy field arises due to the spin orbit coupling which explicitly breaks the SO(3) symmetry of the Heisenberg model due to finite electron mass corrections. The Heisenberg EFT is valid for weak spin orbit coupling $H_A \ll H_E$.

A.1.2 AFMR in polar coordinates

In the following we explicitly follow the treatment of ref. [199], and use the field geometry:

$$\begin{aligned} \boldsymbol{k}_\gamma &= (k, 0, 0)\,, \\ \boldsymbol{H}_\gamma &= (0, 0, H_\gamma)\,, \\ \boldsymbol{E}_\gamma &= (0, E_\gamma, 0)\,, \\ \boldsymbol{H}_0 &= (H_0, 0, 0)\,, \\ \boldsymbol{H}_A &= (H_A, 0, 0)\,. \end{aligned} \tag{A.16}$$

In terms of polar coordinates, we have

$$n_1 = \sin\theta\cos\phi\,, \quad n_2 = \sin\theta\sin\phi\,, \quad n_3 = \cos\theta\,. \tag{A.17}$$

AF order breaks the SO(3) internal symmetry of the spins down to the coset space SO(3)/SO(2) which has the geometry of S^2. The dynamics of the Goldstone modes can be expressed using the polar coordinates. The easy axis has coordinates θ_0, ϕ_0, and we normalise the order parameter to unity. The Goldstone mode Lagrangian at lowest order in derivatives is:

$$\mathcal{L} = \frac{F_1^2}{2}\gamma_{ab}\dot{\vartheta}^a\dot{\vartheta}^b - \frac{F_2^2}{2}\gamma_{ab}\nabla\vartheta^a \cdot \nabla\vartheta^b\,, \tag{A.18}$$

where $a, b = \theta, \phi$ and the metric γ_{ab} is the round metric on the sphere, $\gamma_{ab} = \mathrm{diag}[1, \sin^2\theta]$. The dynamics is easiest to express choosing n_1 to be the easy axis, $\theta_0 = \pi/2$, $\phi_0 = 0$. We then find trivially that, at leading order in fluctuations:

$$n_1 = 1 - \frac{\delta\theta^2}{2} - \frac{\delta\phi^2}{2}\,, \quad n_2 = \delta\phi\,, \quad n_3 = -\delta\theta\,. \tag{A.19}$$

The longitudinal fluctuation, i.e. the change in $\boldsymbol{n}$ projected along the direction of travel of the spin wave, n_1 in this case, is quadratic in the Goldstone modes, while the transverse fluctuations are linear. Note, however, that in these coordinates we always have explicitly two polarizations and no change in the length of the Néel vector. The anisotropy field perturbs the Lagrangian as above, $\Delta\mathcal{L}_A = \mu_B\Sigma_s H_A n_1$, and induces a mass term for $\delta\theta$ and $\delta\phi$. The interaction with applied fields follows exactly as in the Cartesian case using the relations in eq. (A.17).

JCAP08(2021)066

A.1.3 Longitudinal spin waves in the Heisenberg model

The AQ is related to longitudinal fluctuations of the Néel vector (i.e. those in the direction of the anisotropy field), but this is *not* equivalent to a third *longitudinal polarisation* that changes the length of the vector. Such a "true" longitudinal mode is the mode that breaks SO(3) giving rise to AF order, i.e. the Higgs-like radial mode (see also refs. [201, 202]). When writing down the model, we need to be careful that it respects all the symmetries. The field $\vec{\phi} = (\langle \boldsymbol{S}_A \rangle - \langle \boldsymbol{S}_B \rangle)/2$ is the total (staggered) magnetization, the Néel vector, and we can write it as:

$$\vec{\phi} = \rho(x)(n_1(x), n_2(x), n_3(x)) = \rho(x)\boldsymbol{n}\,. \tag{A.20}$$

The field ρ is the longitudinal polarization, while $\boldsymbol{n}$ is the AFMR field introduced above with $|\boldsymbol{n}|^2 = 1$. There is a maximum magentization given by the spin density, and a minimum value pointing in the opposite direction. In our conventions, ϕ is dimensionless and normalized to a maximum of unity, thus $|\phi|^2 \leq 1$ [96].

The constraint $|\phi|^2 \leq 1$ can be enforced naturally by considering the EFT given by the SO(3) invariant metric on S^3 with unit radius. We use the field coordinates:

$$\vec{\varphi} = (\alpha, \theta, \phi)\,, \tag{A.21}$$

where θ, ϕ are the AFMR variables in polar coordinates introduced above, and α is a third polar angle. The metric is

$$ds^2 = g_{AB} d\varphi^A d\varphi^B = d\alpha^2 + \sin^2\alpha d\Omega_2\,, \tag{A.22}$$

where $A, B = \alpha, \theta, \phi$, and $d\Omega_2 = \gamma_{ab} d\vartheta^a d\vartheta^b$ is the round metric on S^2, and $\vec{\vartheta} = (\theta, \phi)$ as above. We see that the polar angle α gives the radius of the S^2 submanifold of S^3, as desired and with the correct normalisation, $\rho = \sin\alpha$. We can interpret α as the angle between the spins in a "bending mode".

The Lagrangian in the absence of external fields is:

$$\mathcal{L} = \frac{F_1^2}{2} g_{AB} \dot{\varphi}^A \dot{\varphi}^B - \frac{F_2^2}{2} g_{AB} \nabla\varphi^A \nabla\varphi^B\,. \tag{A.23}$$

Specifying the anisotropy field allows us to identify the polar axis as n_1 as above. The anisotropy field introduces explicit symmetry breaking and a potential for α, $V(\alpha) \propto -n_1 \propto -\sin\alpha$, which is minimized at $\alpha = \pi/2$. To consider the fluctuations, we write $\alpha = \pi/2 - \sigma$ and σ is the angular field giving rise to the fluctuation in ρ, i.e. the third magnon polarization. It has quadratic Lagrangian:

$$\mathcal{L} = \frac{F_1^2}{2}\dot{\sigma}^2 - \frac{F_2^2}{2}\nabla\sigma^2 - \mu_B \Sigma_s H_A \frac{\sigma^2}{2},\,. \tag{A.24}$$

The field σ couples to the other AFMR fields via the metric g_{AB}:

$$\mathcal{L} = \cos^2\sigma \left[\frac{F_1^2}{2}\gamma_{ab}\dot{\vartheta}^a\dot{\vartheta}^b - \frac{F_2^2}{2} g_{ab}\nabla\vartheta^a\nabla\vartheta^b \right]. \tag{A.25}$$

Expanding $\cos^2\sigma = 1 - \sigma^2$ for the quadratic Lagrangian we see that at leading order we obtain the angular AFMR theory from above, and σ is decoupled. Similarly, σ is decoupled from the external fields in the quadratic Lagrangian, since the spin density, $\boldsymbol{s} = F_1^2 \dot{\phi} \times \phi$, only contains

JCAP08(2021)066

σ at cubic order. Thus, in this S^3 EFT of the Heisenberg model, the σ degree of freedom corresponding to changes in the length of the Néel vector is stabilised by the anisotropy field, and is neither excited by external fields nor mixes with the transverse AFMR polarisations. Could this mode be the AQ? We take the general expression for $\delta\Theta$ in eq. (2.26) and expand n_A in the angular fields. Once again, $\delta\Theta$ is quadratic in all the variables of this model, including σ. We have not been able to obtain a quadratic kinetic term for $\delta\Theta$ from an SO(3) invariant EFT including only the Néel order parameter.

The preceding discussion suggests a possible solution to the problem of the EFT of the AQ. We notice that S^3 is in fact the spin group $\mathrm{Sp}(1) = \mathrm{Spin}(3) = \mathrm{SU}(2)$. Furthermore $\mathrm{SU}(2) \cong \mathrm{SO}(3)/\mathbb{Z}_2$, and for the AQ we are concerned with models that break the discrete symmetries P and T. This suggests using a *complex* field ϕ in the fundamental 2-dimensional representation of a *chiral* SU(2) to represent the AF order parameter, which now has four real degrees of freedom. Thus, after SSB this would give *three* goldstone modes: two "charged" goldstones, giving the transverse magnons, and one "neutral" goldstone, which we assume will be the longitudinal magnon. Each goldstone corresponds to a U(1) subgroup of SU(2). The neutral goldstone is a pseudoscalar, and thus this U(1) group is itself chiral, i.e. a Peccei-Quinn symmetry. The Dirac fermions in the band structure should be charged under this symmetry, such that they acquire chiral rotations ("m_5" mass) governed by the longitudinal mode. Just like the axion and the neutral pion, this new goldstone mode can now couple to $\boldsymbol{E}\cdot\boldsymbol{B}$ via the chiral anomaly. We have not, unfortunately, been able to work out this theory completely.

A.2 The Landau-Lifshitz equations

In this appendix, following refs. [203, 204], we describe an antiferromagnetic resonance (AFMR) state using the Landau-Lifshitz equation. We consider the action of the Néel field described by the non-linear sigma model [96],

$$S_{\mathrm{AF}} = g^2 J \int dt d^3r \left[(\partial_\mu \boldsymbol{n}) \cdot (\partial^\mu \boldsymbol{n}) - \Delta_0^2 \boldsymbol{n}^2 \right]. \tag{A.26}$$

In order to implement a little more realistic condition in eq. (A.26), we take into account a small net magnetization $\boldsymbol{m}$ satisfying the constraint $\boldsymbol{n}\cdot\boldsymbol{m} = 0$ with $|\boldsymbol{n}| = 1$ and $|\boldsymbol{m}| \ll 1$. Furthermore, we assume the case of AF insulators with easy-axis anisotropy. Then a modification of eq. (A.26) gives the free energy of such AF insulators as [205, 206]

$$F_{\mathrm{AF}} = \int d^3r \left[\frac{a}{2}\boldsymbol{m}^2 + \frac{A}{2} \sum_{i=x,y,z} (\partial_i \boldsymbol{n})^2 - \frac{K}{2} n_z^2 - \boldsymbol{H}\cdot\boldsymbol{m} \right], \tag{A.27}$$

where a and A are the homogeneous and inhomogeneous exchange constants, respectively, and K is the easy-axis anisotropy along the z direction. The fourth term is the Zeeman coupling with $\boldsymbol{H} = g\mu_B \boldsymbol{B}$ being an external magnetic field.

In the case in which a dc magnetic field $\boldsymbol{H}_0$ and an ac magnetic field (i.e., RF field) $\boldsymbol{h}(t)$ are applied to the AF insulator, the total magnetic field in eq. (A.27) is

$$\boldsymbol{H} = \boldsymbol{H}_0 + \boldsymbol{h}(t), \tag{A.28}$$

where $\boldsymbol{H}_0 = g\mu_B B \boldsymbol{e}_z$ with B being much weaker than both the AF exchange coupling and easy-axial anisotropy and $\boldsymbol{h}(t) = \boldsymbol{h}_{\mathrm{RF}} e^{-i\omega_0 t}$. Here, $\boldsymbol{e}_z$ is the unit vector parallel to the easy

JCAP08(2021)066

axis of the AF order. Now we study the dynamics of $\boldsymbol{m}$ and $\boldsymbol{n}$ phenomenologically, i.e., based on the Landau-Lifshitz-Gilbert (LLG) equation [203, 204, 206]. From the free energy of the system $F_{\rm AF}$, the effective fields for $\boldsymbol{n}$ and $\boldsymbol{m}$ are given by

$$\begin{aligned}\boldsymbol{f}_n &= -\frac{\delta F_{\rm AF}}{\delta \boldsymbol{n}} = A\boldsymbol{n}\times(\nabla^2\boldsymbol{n}\times\boldsymbol{n}) + Kn_z\boldsymbol{e}_z - (\boldsymbol{n}\cdot\boldsymbol{H})\boldsymbol{m},\\ \boldsymbol{f}_m &= -\frac{\delta F_{\rm AF}}{\delta \boldsymbol{m}} = -a\boldsymbol{m} + \boldsymbol{n}\times(\boldsymbol{H}\times\boldsymbol{n}).\end{aligned} \tag{A.29}$$

The LLG equation is given by

$$\begin{aligned}\dot{\boldsymbol{n}} &= (\gamma\boldsymbol{f}_m - G_1\dot{\boldsymbol{m}})\times\boldsymbol{n},\\ \dot{\boldsymbol{m}} &= (\gamma\boldsymbol{f}_n - G_2\dot{\boldsymbol{n}})\times\boldsymbol{n} + (\gamma\boldsymbol{f}_m - G_1\dot{\boldsymbol{m}})\times\boldsymbol{m},\end{aligned} \tag{A.30}$$

where $\gamma = 1/\hbar$ and G_1 and G_2 are dimensionless Gilbert damping constants. For the purpose of deriving the AFMR state, we may neglect the Gilbert damping constants. Then, the LLG eq. (A.30) is simplified as

$$\dot{\boldsymbol{n}} = \gamma(-a\boldsymbol{m} + \boldsymbol{H})\times\boldsymbol{n}, \tag{A.31a}$$

$$\dot{\boldsymbol{m}} = \gamma K n_z\boldsymbol{e}_z\times\boldsymbol{n} + \gamma\boldsymbol{H}\times\boldsymbol{m}, \tag{A.31b}$$

where we have assumed that $\boldsymbol{n}$ is spatially uniform, and we have used $|\boldsymbol{n}|^2 = 1$ and an identity for matrices $\boldsymbol{A}\times(\boldsymbol{B}\times\boldsymbol{C}) = (\boldsymbol{A}\cdot\boldsymbol{C})\boldsymbol{B} - (\boldsymbol{A}\cdot\boldsymbol{B})\boldsymbol{C}$. After some straightforward matrix algebra, we arrive at the following equation for the Néel field:

$$\boldsymbol{n}\times\ddot{\boldsymbol{n}} + \omega_K\omega_a n_z\boldsymbol{e}_z\times\boldsymbol{n} - \gamma^2(\boldsymbol{n}\cdot\boldsymbol{H})\boldsymbol{H}\times\boldsymbol{n} + 2\gamma(\boldsymbol{n}\cdot\boldsymbol{H})\dot{\boldsymbol{n}} + \gamma(\boldsymbol{n}\cdot\dot{\boldsymbol{H}})\boldsymbol{n} = \gamma\dot{\boldsymbol{H}}. \tag{A.32}$$

To obtain the AFMR state, where all the spins are fluctuating uniformly, we assume the dynamics of the Néel vector and the total magnetization around the easy axis as

$$\boldsymbol{n}(t) = \boldsymbol{e}_z + \delta\boldsymbol{n}(t) \quad \text{and} \quad \boldsymbol{m}(t) = \delta\boldsymbol{m}(t), \tag{A.33}$$

denoting that $\delta\boldsymbol{n}(t)$ and $\delta\boldsymbol{m}(t)$ are the small fluctuation components with $|\delta\boldsymbol{n}|, |\delta\boldsymbol{m}| \ll 1$. Substituting this form into eq. (A.32), and then linearizing and Fourier transforming $\delta\boldsymbol{n}(t) = \int \delta\tilde{\boldsymbol{n}}(\omega)e^{-i\omega t}d\omega/(2\pi)$, eq. (A.32) reduces to [203, 204]

$$2i\omega_H\omega\delta\tilde{\boldsymbol{n}}/\omega_a + \left[\left(\omega^2 + \omega_H^2\right)/\omega_a - \omega_K\right]\boldsymbol{e}_z\times\delta\tilde{\boldsymbol{n}} = \boldsymbol{\mathcal{D}}\delta(\omega_0 - \omega), \tag{A.34}$$

where $\omega_H = \gamma g\mu_B B$, $\omega_a = \gamma a$, $\omega_K = \gamma K$, and ω_0 is the frequency of the RF field $[\boldsymbol{h}(t) = \boldsymbol{h}_{\rm RF}e^{-i\omega_0 t}]$. In eq. (A.34), $\boldsymbol{\mathcal{D}} = -i\gamma\omega_0(h^x_{\rm RF}\boldsymbol{e}_x + h^y_{\rm RF}\boldsymbol{e}_y)$ is understood as the "driving force" vector causing the AFMR. Equation (A.34) is rewritten in the matrix form

$$\begin{bmatrix} 2i\omega\omega_H & -\left(\omega^2 - \omega_a\omega_K + \omega_H^2\right)\\ \omega^2 - \omega_a\omega_K + \omega_H^2 & 2i\omega\omega_H\end{bmatrix}\begin{bmatrix}\delta\tilde{n}_x(\omega)\\ \delta\tilde{n}_y(\omega)\end{bmatrix} = \omega_a\delta(\omega_0-\omega)\begin{bmatrix}\mathcal{D}_x\\ \mathcal{D}_y\end{bmatrix}. \tag{A.35}$$

Multiplying the inverse matrix from the left hand side, we obtain

$$\begin{bmatrix}\delta\tilde{n}_x(\omega)\\ \delta\tilde{n}_y(\omega)\end{bmatrix} = \begin{bmatrix}\chi_1(\omega) & \chi_2(\omega)\\ -\chi_2(\omega) & \chi_1(\omega)\end{bmatrix}\begin{bmatrix}\mathcal{D}_x\\ \mathcal{D}_y\end{bmatrix}, \tag{A.36}$$

where the susceptibility is defined as

$$\begin{bmatrix} \chi_1(\omega) & \chi_2(\omega) \\ -\chi_2(\omega) & \chi_1(\omega) \end{bmatrix} = \frac{\omega_a \delta(\omega_0 - \omega)}{(\omega^2 - \omega_+^2)(\omega^2 - \omega_-^2)} \begin{bmatrix} 2i\omega\omega_H & \omega^2 - \omega_a\omega_K + \omega_H^2 \\ -(\omega^2 - \omega_a\omega_K + \omega_H^2) & 2i\omega\omega_H \end{bmatrix}. \quad \text{(A.37)}$$

Here,

$$\omega_\pm = \omega_H \pm \sqrt{\omega_a \omega_K} \quad \text{(A.38)}$$

are the resonance frequencies. Note that these frequencies do not depend on the parameters of the driving force $\boldsymbol{\mathcal{D}}$.

Along with eq. (A.34), the following equation is obtained from $2\gamma(\boldsymbol{n}\cdot\boldsymbol{H})\dot{\boldsymbol{n}} + \gamma(\boldsymbol{n}\cdot\dot{\boldsymbol{H}})\boldsymbol{n}$ in eq. (A.32), which describes the "longitudinal" AFMR state:

$$2\omega_H \delta\dot{n}_z \boldsymbol{e}_z = i\gamma\omega_0 e^{-i\omega_0 t}(h^x_{\mathrm{RF}}\delta n_x + h^y_{\mathrm{RF}}\delta n_y)\boldsymbol{e}_z. \quad \text{(A.39)}$$

Fourier transforming this equation and substituting the solution for δn_x and δn_y [eq. (A.36)] into it, we have

$$\delta\tilde{n}_z(\omega) \propto h^x_{\mathrm{RF}}\delta\tilde{n}_x(\omega - \omega_0) + h^y_{\mathrm{RF}}\delta\tilde{n}_y(\omega - \omega_0) \propto \frac{\delta(2\omega_0 - \omega)}{[(\omega - \omega_0)^2 - \omega_+^2][(\omega - \omega_0)^2 - \omega_-^2]}, \quad \text{(A.40)}$$

which indicates that the resonance frequencies of the longitudinal AFMR are $\omega = 2\omega_0 = 2\omega_\pm$. Eq. (A.40) reveals that the longitudinal mode is quadratic in the RF field, i.e., a second-order response to the RF field, while the transverse mode [eq. (A.36)] is a linear response to the RF field.

B Axion dark matter and the millielectronvolt range

Since their initial proposal as a solution for the Strong $\mathcal{CP}$ problem more than 40 years ago [1–3, 207], (QCD) axions have seen phases of growing interest due to a number of breakthroughs. The first was the realisation that axions are excellent dark matter candidates [7–9, 208], and that there are several ways to search for them experimentally [32, 209–211]. Recently, there has been a huge growth of new ideas for axion searches (see ref. [18] for a review), which includes the present proposal ("Paper I") using topological insulators [41].

The QCD axion was originally proposed as the pseudo-Goldstone boson of a spontaneously broken global U(1) symmetry, which couples to chiral fermions charged under the strong nuclear force, $\mathrm{SU}(3)_c$ gauge symmetry (i.e. quarks). Such a global symmetry is known as a Peccei-Quinn (PQ) symmetry, $\mathrm{U}(1)_{\mathrm{PQ}}$. More generally, QCD axions can be regarded as pseudo-Goldstone bosons coupled to the QCD anomaly term, schematically $G\tilde{G}$, where G is the gluon field strength tensor, and $\tilde{G}$ its dual.

The PQ symmetry breaking scale, v_{PQ}, is not predicted by the theory, although it is expected to be below the reduced Planck scale, $M_{\mathrm{Pl}} = 2.4 \times 10^{18}\,\mathrm{GeV}$ [212]. The symmetry breaking scale sets the axion mass, which arises due to the axion's coupling to the QCD topological charge via $\mathrm{SU}(3)_c$ instantons, and which reaches its zero-temperature value at temperatures lower than the QCD crossover temperature of around 157 MeV [213, 214]. The axion mass at such temperatures is given by [215]

$$m_a = \frac{\sqrt{\chi_0}}{f_a} = 5.69(5)\,\mathrm{meV}\left(\frac{10^9\,\mathrm{GeV}}{f_a}\right), \quad \text{(B.1)}$$

JCAP08(2021)066

where χ_0 is the zero-temperature QCD topological susceptibility, $f_a = v_{\rm PQ}/\mathcal{N}$, and $\mathcal{N}$ is the SU(3)$_c$ anomaly of U(1)$_{\rm PQ}$. The value of χ_0 can be calculated from chiral perturbation theory [2, 215, 216] while, at higher temperatures, it can be calculated using lattice quantum field theory (see e.g. ref. [217]), or using instanton methods [218, 219].

The QCD axion couples to the EM Chern-Simons term via two means. Firstly, by its model-independent mixing with pions, and secondly via the (model-dependent) electromagnetic anomaly ($\mathcal{E}$) of fermions charged under U(1)$_{\rm PQ}$. The coupling is [e.g. 216]

$$\Delta\mathcal{L} = g_{a\gamma}\, a\, \boldsymbol{E}\cdot\boldsymbol{B}\,, \tag{B.2}$$

where $a \equiv f_a\,\theta$ is the canonically normalised axion field and $g_{a\gamma}$ is the axion-photon coupling, which is given by

$$g_{a\gamma} = \frac{\alpha}{2\pi f_a}\, C_{a\gamma} = \frac{\alpha}{\pi f_a}\left[\frac{\mathcal{E}}{\mathcal{N}} - 1.92(4)\right]\,, \tag{B.3}$$

where $\mathcal{N}$ is the SU(3)$_c$ anomaly of the PQ symmetry, and is equal to unity in the KSVZ model, while for the DFSZ model $\mathcal{N} = 6$. The value of $\mathcal{E}/\mathcal{N}$ depends on the PQ charges and gauge group representations of fermions. We define the QCD model band according to the "preferred" models of ref. [29], which corresponds to $5/3 < \mathcal{E}/\mathcal{N} < 44/3$. Experiments constrain $|g_{a\gamma}|$, and so this band and encompasses the original KSVZ ($\mathcal{E}/\mathcal{N} = 0$) and DFSZ ($\mathcal{E}/\mathcal{N} = 8/3$) models. For a generic "axion-like particle", the coupling $g_{a\gamma}$ is taken as a free parameter independent of m_a.

The QCD axion mass is bounded from above and below by astrophysical constraints. The existence of BHs with masses of order ten solar masses with high spins, stable over astrophysical timescales, would be impossible if the QCD axion existed and $m_a \lesssim 10^{-12}\,$eV [14, 15, 220]. In such a case, the axion Compton wavelength is resonant with the size of the BH ergoregion, causing axions to be abundantly created from vacuum fluctuations, and rapidly draining the spin of the BH. On the other end of the mass scale, the QCD axion with $m_a \gtrsim 0.02\,$eV is excluded by observations of neutrinos coinciding with the galactic supernova SN1987A [11, 12]. The QCD axion couples to nuclei in the supernova, and axions are emitted by nuclear bremsstrahlung, cooling the supernova more rapidly and shortening the neutrino burst if the axion-nucleon coupling (proportional to m_a) is too large. Since there is no statistically rigorous bound associated with SN1987A, we also mention that a looser upper limit on m_a can be derived from constraints on the relativistic energy density in the early Universe (parameterised as a hot DM component). Hot QCD axions are produced by their interaction with pions. The amount of hot axions produced is in conflict with the cosmic microwave background anisotropies as measured by the *Planck* satellite [10, 182] if $m_a \gtrsim 0.3\,$eV (see e.g. refs. [19, 181]).

In the mass range of interest for TOORAD, the axion-photon coupling is mostly constrained by axion helioscopes [171] and cooling of Horizontal Branch (HB) stars through the ratio of HB and Red Giant Branch stars [221, 222], which both lead to limits of the order $g_{a\gamma} \lesssim 10^{-10}\,{\rm GeV}^{-1}$. This is far above the coupling for typical QCD axion models.

Assuming that the QCD axion indeed composes the observed DM with cosmic density parameter $\Omega_d h^2 = 0.12$ [182], it is possible to analyse the value of m_a further (for a review, see ref. [16]). If the maximum temperature of the Universe exceeds the PQ phase transition temperature, $T_{\rm PQ} \sim v_{\rm PQ}$, or if the Hubble scale during inflation $H_I > 2\pi v_{\rm PQ}$, then the PQ symmetry is unbroken at the end of inflation. When it subsequently breaks, the Kibble mechanism leads to a network of topological strings that persists as the Universe expands and, when the axion mass becomes cosmologically relevant $m_a \sim H$ (where H is the Hubble

JCAP08(2021)066

parameter) domain walls form [223–225]. Such defects emit DM axions, and eventually decay when $H \ll m_a$. In this case, if $\mathcal{N} = 1$ (which imnolies the domain wall network is unstable, then the DM abundance is in principle calculable and depends only on m_a. However the dynamics of the strings and domain walls are complex and the axion abundance can only accurately be determined by numerical simulations. This computation cannot be performed at the physical scale separation (between the string thickness and the Hubble length, which in turn sets the string tension), and so the results must be extrapolated. In the case $\mathcal{N} > 1$, the DM abundance depends on an additonal biasing parameter required such that the domain wall network decays [226].

When $\mathcal{N} = 1$, recent simulations [183] have placed a lower bound on the QCD axion mass $m_a \gtrsim 0.5\,\mathrm{meV}$ by considering axions emitted by the string network prior to the axion mass becoming relevant, a well controlled extrapolation to the physical scale separation, and a computation of non-linear effects after the network decays.[13] This work also estimates the bound $m_a \gtrsim 3.5\,\mathrm{meV}$ when $\mathcal{N} > 1$, in agreement with the general expectation that the axion mass should be larger in this scenario [226, 229, 230]. One issue for axion direct detection in the post inflation scenario is the existence of axion "miniclusters" [231–233]. Recent simulations of structure formation in this scenario suggest that a large fraction of the DM (50% or more at the solar radius in the Milky Way) is bound in dense, low mass objects [234–237]. These objects have a low collision cross section with the Earth, and reduce the effective value of the local DM density for a direct detection experiment.

In the alternative scenario for axion production, the PQ symmetry is broken in the very early Universe during the hypothetical period of inflation [238–240], and axions are subsequently produced when the initial vacuum state of the axion decays, in a process called "realignment". This scenario has more free parameters than just m_a, and it is not possible to predict the axion mass based on the observed DM abundance. This scenario is incompatible with a large energy scale of inflation, and would be ruled out if primordial gravitational waves were observed [241]. If the initial vacuum value of θ is assumed to be of order 1 the axion mass in the pre-inflationary scenario is bounded to $m_a \gtrsim 0.7\,\mu\mathrm{eV}$ [242]. However, anthropic pressure due to the need for DM to form galaxies can allow for much lower or higher values of the mass in this scenario [243, 244]. Limits on the mass in this case are only imposed with additional assumptions on the energy scale of inflation, which limit the allowed level of tuning on the free parameter.

C Comparison to earlier results

The forecasts shown in figure 23 differ in many respects from those in Paper I, and we explain briefly why, see figure 25, which shows the same projection alongside those of Paper I. For the detector, Paper I assumed a coupling factor equivalent to efficiency $\eta = 0.01$, and the same dark count rate as in the present work. The difference in the scan depth arises because the power output in Paper I was computed in analogy to a resonant cavity, and this formula is incorrect for a medium with a polariton resonance. Allowing for a few translations, however, the results can be compared. All in all, however, we stress that the power formula in Paper I was far too simplistic, and so should not be used.

Our present corrected calculations have shown that the power does not scale with the material volume as assumed in Paper I: rather it depends separately on the surface area and the material thickness. Losses lead to a maximum useful thickness, an effect which was not

[13] Other extrapolations to the physical scale separation lead to lower bounds on the mass [227, 228].

JCAP08(2021)066

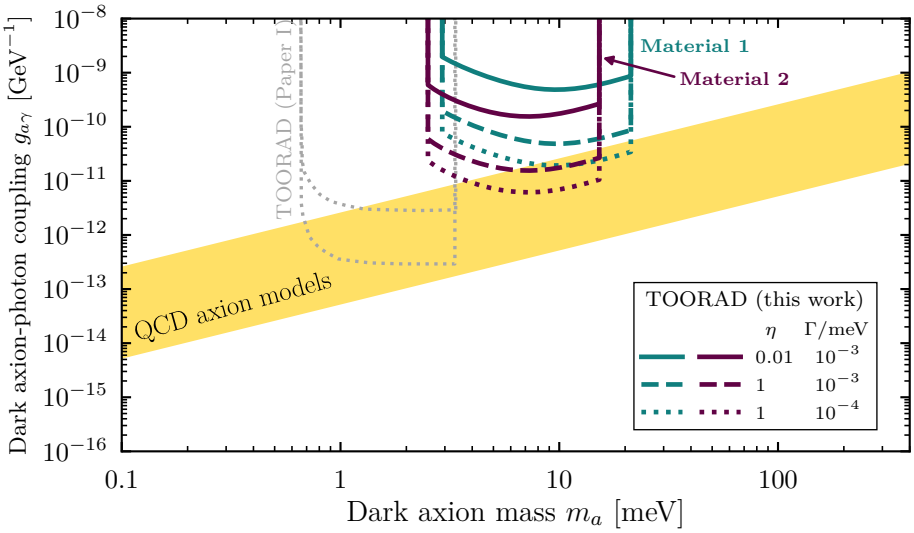

Figure 25. Comparison between the forecasts made in Paper I (gray) and those in the present work (coloured lines).

accounted for in Paper I. For the models presently considered, this leads to a total useful material volume around 40 cm^3. Thus for comparison, we show the Paper I estimates for "Stage I", which used a total volume of material 1 cm^3, and 'Stage II", which used a total volume of material 100 cm^3, equivalent to $d \approx 1$ mm in the present case. The "Stage III" volume considered in Paper I is inaccessible due to the finite skin depth induced by realistic $\mathcal{O}(\mu\text{eV})$ losses.

Paper I included losses only by a rough estimate for the bulk quality factor, which was taken as $Q = 10^5$, roughly $\Gamma = 10^{-5}$ meV (this assumed power law decreases in Γ_m at low T as discussed in the present work, but neglected the impurity and conductance contributions). On the other hand, Paper I assumed that the power was reduced by a polariton mode mixing factor, f_+, which is absent in the present treatment (mode mixing mostly affects the width of the resonance). Together, these amount to an assumed $\beta^2 \approx 10^4$ for some baseline parameters. Comparing to figure 19, using the correct computations from the present paper, such a large β could only be achieved with losses $\Gamma = 10^{-5}$ meV. These many considerations explain the different depth of the constraints in terms of $g_{a\gamma}$ in the present work compared to Paper I.

The difference in the scanned mass range in the present work compared to Paper I is more useful and necessary to explain. It arises from the adopted values of m_Θ and f_Θ. In the present work we take our preferred material as $Mn_2Bi_2Te_5$, while Paper I uses $(Bi_{1-x}Fe_x)_2Se_3$. Even so, there are differences to the $(Bi_{1-x}Fe_x)_2Se_3$ parameter estimates in Paper I compared to the present work. In Paper I we erroneously assumed that m_Θ was equal to the AFMR frequency of the transverse magnon polarisations (with a reduction due to the doping required in $(Bi_{1-x}Fe_x)_2Se_3$) leading to $m_\Theta = 0.6$ meV, and thus a lower minimum value of m_a in the Paper I treatment. Paper I also incorrectly included the Kittel shift to m_Θ. As discussed, the longitudinal magnon is not simply related to the transverse modes and Paper I should have used the value of m_Θ computed by ref. [42], as we do in the present work. However, as we have noted, ref. [42] used a square lattice approximation to compute m_Θ. We do not

JCAP08(2021)066

know the error induced by this assumption on the lower limit of the scannable mass range also in the present work.

Furthermore, Paper I assumed f_Θ for $(Bi_{1-x}Fe_x)_2Se_3$ directly from ref. [42]. In the present work we corrected this value using more up to date estimates of the bulk band gap of $(Bi_{1-x}Fe_x)_2Se_3$ including the effects of magnetic doping, leading to the "Material 1" parameter estimates with lower f_Θ. The lower value of f_Θ in the present work allows for a wider range of masses to be scanned for the same range of B-field strengths.

References

[1] R.D. Peccei and H.R. Quinn, *CP Conservation in the Presence of Instantons*, *Phys. Rev. Lett.* **38** (1977) 1440 [INSPIRE].

[2] S. Weinberg, *A New Light Boson?*, *Phys. Rev. Lett.* **40** (1978) 223 [INSPIRE].

[3] F. Wilczek, *Problem of Strong P and T Invariance in the Presence of Instantons*, *Phys. Rev. Lett.* **40** (1978) 279 [INSPIRE].

[4] C. Vafa and E. Witten, *Parity Conservation in QCD*, *Phys. Rev. Lett.* **53** (1984) 535 [INSPIRE].

[5] J.M. Pendlebury et al., *Revised experimental upper limit on the electric dipole moment of the neutron*, *Phys. Rev. D* **92** (2015) 092003 [arXiv:1509.04411] [INSPIRE].

[6] A. Hook, *TASI Lectures on the Strong CP Problem and Axions*, *PoS* **TASI2018** (2019) 004 [arXiv:1812.02669] [INSPIRE].

[7] L.F. Abbott and P. Sikivie, *A Cosmological Bound on the Invisible Axion*, *Phys. Lett. B* **120** (1983) 133 [INSPIRE].

[8] M. Dine and W. Fischler, *The Not So Harmless Axion*, *Phys. Lett. B* **120** (1983) 137 [INSPIRE].

[9] J. Preskill, M.B. Wise and F. Wilczek, *Cosmology of the Invisible Axion*, *Phys. Lett. B* **120** (1983) 127 [INSPIRE].

[10] PLANCK collaboration, *Planck 2015 results. XIII. Cosmological parameters*, *Astron. Astrophys.* **594** (2016) A13 [arXiv:1502.01589] [INSPIRE].

[11] G.G. Raffelt, *Astrophysical axion bounds*, *Lect. Notes Phys.* **741** (2008) 51 [hep-ph/0611350] [INSPIRE].

[12] J.H. Chang, R. Essig and S.D. McDermott, *Supernova 1987A Constraints on Sub-GeV Dark Sectors, Millicharged Particles, the QCD Axion, and an Axion-like Particle*, *JHEP* **09** (2018) 051 [arXiv:1803.00993] [INSPIRE].

[13] P. Carenza, T. Fischer, M. Giannotti, G. Guo, G. Martínez-Pinedo and A. Mirizzi, *Improved axion emissivity from a supernova via nucleon-nucleon bremsstrahlung*, *JCAP* **10** (2019) 016 [*Erratum ibid.* **05** (2020) E01] [arXiv:1906.11844] [INSPIRE].

[14] A. Arvanitaki, M. Baryakhtar and X. Huang, *Discovering the QCD Axion with Black Holes and Gravitational Waves*, *Phys. Rev. D* **91** (2015) 084011 [arXiv:1411.2263] [INSPIRE].

[15] M.J. Stott and D.J.E. Marsh, *Black hole spin constraints on the mass spectrum and number of axionlike fields*, *Phys. Rev. D* **98** (2018) 083006 [arXiv:1805.02016] [INSPIRE].

[16] D.J.E. Marsh, *Axion Cosmology*, *Phys. Rept.* **643** (2016) 1 [arXiv:1510.07633] [INSPIRE].

[17] M. Giannotti, I.G. Irastorza, J. Redondo, A. Ringwald and K. Saikawa, *Stellar Recipes for Axion Hunters*, *JCAP* **10** (2017) 010 [arXiv:1708.02111] [INSPIRE].

JCAP08(2021)066

[18] I.G. Irastorza and J. Redondo, *New experimental approaches in the search for axion-like particles*, *Prog. Part. Nucl. Phys.* **102** (2018) 89 [arXiv:1801.08127] [INSPIRE].

[19] L. Di Luzio, M. Giannotti, E. Nardi and L. Visinelli, *The landscape of QCD axion models*, *Phys. Rept.* **870** (2020) 1 [arXiv:2003.01100] [INSPIRE].

[20] PARTICLE DATA GROUP collaboration, *Review of Particle Physics*, *Phys. Rev. D* **98** (2018) 030001 [INSPIRE].

[21] J.W. Foster, N.L. Rodd and B.R. Safdi, *Revealing the Dark Matter Halo with Axion Direct Detection*, *Phys. Rev. D* **97** (2018) 123006 [arXiv:1711.10489] [INSPIRE].

[22] G.P. Centers et al., *Stochastic fluctuations of bosonic dark matter*, arXiv:1905.13650 [INSPIRE].

[23] C.A.J. O'Hare and A.M. Green, *Axion astronomy with microwave cavity experiments*, *Phys. Rev. D* **95** (2017) 063017 [arXiv:1701.03118] [INSPIRE].

[24] J.E. Kim, *Weak Interaction Singlet and Strong CP Invariance*, *Phys. Rev. Lett.* **43** (1979) 103 [INSPIRE].

[25] M.A. Shifman, A.I. Vainshtein and V.I. Zakharov, *Can Confinement Ensure Natural CP Invariance of Strong Interactions?*, *Nucl. Phys. B* **166** (1980) 493 [INSPIRE].

[26] A. Zhitnitsky, *On Possible Suppression of the Axion Hadron Interactions* (in Russian), *Sov. J. Nucl. Phys.* **31** (1980) 260.

[27] M. Dine, W. Fischler and M. Srednicki, *A Simple Solution to the Strong CP Problem with a Harmless Axion*, *Phys. Lett. B* **104** (1981) 199 [INSPIRE].

[28] L. Di Luzio, F. Mescia and E. Nardi, *Redefining the Axion Window*, *Phys. Rev. Lett.* **118** (2017) 031801 [arXiv:1610.07593] [INSPIRE].

[29] L. Di Luzio, F. Mescia and E. Nardi, *Window for preferred axion models*, *Phys. Rev. D* **96** (2017) 075003 [arXiv:1705.05370] [INSPIRE].

[30] D. Horns, J. Jaeckel, A. Lindner, A. Lobanov, J. Redondo and A. Ringwald, *Searching for WISPy Cold Dark Matter with a Dish Antenna*, *JCAP* **04** (2013) 016 [arXiv:1212.2970] [INSPIRE].

[31] ADMX collaboration, *Extended Search for the Invisible Axion with the Axion Dark Matter Experiment*, *Phys. Rev. Lett.* **124** (2020) 101303 [arXiv:1910.08638] [INSPIRE].

[32] P. Sikivie, *Experimental Tests of the Invisible Axion*, *Phys. Rev. Lett.* **51** (1983) 1415 [*Erratum ibid.* **52** (1984) 695] [INSPIRE].

[33] MADMAX WORKING GROUP collaboration, *Dielectric Haloscopes: A New Way to Detect Axion Dark Matter*, *Phys. Rev. Lett.* **118** (2017) 091801 [arXiv:1611.05865] [INSPIRE].

[34] D. Budker, P.W. Graham, M. Ledbetter, S. Rajendran and A. Sushkov, *Proposal for a Cosmic Axion Spin Precession Experiment (CASPEr)*, *Phys. Rev. X* **4** (2014) 021030 [arXiv:1306.6089] [INSPIRE].

[35] A. Álvarez Melcón et al., *Scalable haloscopes for axion dark matter detection in the 30μeV range with RADES*, *JHEP* **07** (2020) 084 [arXiv:2002.07639] [INSPIRE].

[36] Y.K. Semertzidis et al., *Axion Dark Matter Research with IBS/CAPP*, arXiv:1910.11591 [INSPIRE].

[37] HAYSTAC collaboration, *A quantum-enhanced search for dark matter axions*, *Nature* **590** (2021) 238 [arXiv:2008.01853] [INSPIRE].

[38] J.L. Ouellet et al., *First Results from ABRACADABRA-10 cm: A Search for Sub-μeV Axion Dark Matter*, *Phys. Rev. Lett.* **122** (2019) 121802 [arXiv:1810.12257] [INSPIRE].

JCAP08(2021)066

[39] Y. Michimura et al., *DANCE: Dark matter Axion search with riNg Cavity Experiment*, *J. Phys. Conf. Ser.* **1468** (2020) 012032 [arXiv:1911.05196] [INSPIRE].

[40] QUAX collaboration, *Axion search with a quantum-limited ferromagnetic haloscope*, *Phys. Rev. Lett.* **124** (2020) 171801 [arXiv:2001.08940] [INSPIRE].

[41] D.J.E. Marsh, K.-C. Fong, E.W. Lentz, L. Šmejkal and M.N. Ali, *Proposal to Detect Dark Matter using Axionic Topological Antiferromagnets*, *Phys. Rev. Lett.* **123** (2019) 121601 [arXiv:1807.08810] [INSPIRE].

[42] R. Li, J. Wang, X. Qi and S.-C. Zhang, *Dynamical Axion Field in Topological Magnetic Insulators*, *Nature Phys.* **6** (2010) 284 [arXiv:0908.1537] [INSPIRE].

[43] J. Zhang, D. Wang, M. Shi, T. Zhu, H. Zhang and J. Wang, *Large Dynamical Axion Field in Topological Antiferromagnetic Insulator $Mn_2Bi_2Te_5$*, *Chin. Phys. Lett.* **37** (2020) 077304 [arXiv:1906.07891] [INSPIRE].

[44] F. Wilczek, *Two Applications of Axion Electrodynamics*, *Phys. Rev. Lett.* **58** (1987) 1799 [INSPIRE].

[45] G.-H. Lee et al., *Graphene-based Josephson junction microwave bolometer*, *Nature* **586** (2020) 42 [arXiv:1909.05413].

[46] A. Little et al., *Antiferromagnetic Resonance and Terahertz Continuum in α -$RuCl_3$*, *Phys. Rev. Lett.* **119** (2017) 227201 [arXiv:1704.07357].

[47] A.J. Millar, G.G. Raffelt, J. Redondo and F.D. Steffen, *Dielectric Haloscopes to Search for Axion Dark Matter: Theoretical Foundations*, *JCAP* **01** (2017) 061 [arXiv:1612.07057] [INSPIRE].

[48] A.M. Essin, J.E. Moore and D. Vanderbilt, *Magnetoelectric polarizability and axion electrodynamics in crystalline insulators*, *Phys. Rev. Lett.* **102** (2009) 146805 [arXiv:0810.2998] [INSPIRE].

[49] D. Tong, *Gauge Theory*, Lecture Notes, University of Cambridge, (2018).

[50] A. Sekine and K. Nomura, *Axion Electrodynamics in Topological Materials*, *J. Appl. Phys.* **129** (2021) 141101 [arXiv:2011.13601] [INSPIRE].

[51] A. Sekine and K. Nomura, *Axionic Antiferromagnetic Insulator Phase in a Correlated and Spin-Orbit Coupled System*, *J. Phys. Soc. Jap.* **83** (2014) 104709 [arXiv:1401.4523] [INSPIRE].

[52] S.J. Pickart, M.F. Collins and C.G. Windsor, *Spin-wave dispersion in kmnf3*, *J. Appl. Phys.* **37** (1966) 1054.

[53] M.Z. Hasan and C.L. Kane, *Topological Insulators*, *Rev. Mod. Phys.* **82** (2010) 3045 [arXiv:1002.3895] [INSPIRE].

[54] X.L. Qi and S.C. Zhang, *Topological insulators and superconductors*, *Rev. Mod. Phys.* **83** (2011) 1057 [arXiv:1008.2026] [INSPIRE].

[55] X. Wan, A. Vishwanath and S.Y. Savrasov, *Computational Design of Axion Insulators Based on 5d Spinels Compounds*, *Phys. Rev. Lett.* **108** (2012) 146601 [arXiv:1103.4634] [INSPIRE].

[56] N. Varnava and D. Vanderbilt, *Surfaces of Axion Insulators*, *Phys. Rev. B* **98** (2018) 245117 [arXiv:1809.02853] [INSPIRE].

[57] D.M. Nenno, C.A.C. Garcia, J. Gooth, C. Felser and P. Narang, *Axion physics in condensed-matter systems*, *Nature Rev. Phys.* **2** (2020) 682.

[58] F. Matera and M.F. Wagner, *Low-energy modes of spin-imbalanced Fermi gases in BCS phase*, *Eur. Phys. J. D* **71** (2017) 293 [arXiv:1705.11162] [INSPIRE].

JCAP08(2021)066

[59] N. Varnava, I. Souza and D. Vanderbilt, *Axion coupling in the hybrid Wannier representation*, *Phys. Rev. B* **101** (2020) 155130 [arXiv:1912.11887] [INSPIRE].

[60] A.M. Turner, Y. Zhang, R.S.K. Mong and A. Vishwanath, *Quantized response and topology of magnetic insulators with inversion symmetry*, *Phys. Rev. B* **85** (2012) 165120 [arXiv:1010.4335].

[61] C. Fang, M.J. Gilbert and B.A. Bernevig, *Bulk topological invariants in noninteracting point group symmetric insulators*, *Phys. Rev. B* **86** (2012) 115112 [arXiv:1207.5767].

[62] H. Watanabe, H.C. Po and A. Vishwanath, *Structure and topology of band structures in the 1651 magnetic space groups*, *Sci. Adv.* **4** (2018) eaat8685 [arXiv:1707.01903].

[63] L. Elcoro, B.J. Wieder, Z. Song, Y. Xu, B. Bradlyn and B.A. Bernevig, *Magnetic Topological Quantum Chemistry*, arXiv:2010.00598.

[64] S. Ryu, A.P. Schnyder, A. Furusaki and A.W.W. Ludwig, *Topological insulators and superconductors: Tenfold way and dimensional hierarchy*, *New J. Phys.* **12** (2010) 065010 [arXiv:0912.2157] [INSPIRE].

[65] D. Gresch et al., *Z2Pack: Numerical Implementation of Hybrid Wannier Centers for Identifying Topological Materials*, *Phys. Rev. B* **95** (2017) 075146 [arXiv:1610.08983] [INSPIRE].

[66] L. Šmejkal, J. Železný, J. Sinova and T. Jungwirth, *Electric Control of Dirac Quasiparticles by Spin-Orbit Torque in an Antiferromagnet*, *Phys. Rev. Lett.* **118** (2017) 106402, [1610.08107].

[67] P. Tang, Q. Zhou, G. Xu and S.-C. Zhang, *Dirac fermions in an antiferromagnetic semimetal*, *Nature Phys.* **12** (2016) 1100 [arXiv:1603.08060].

[68] I.E. Dzyaloshinskiĭ, *On the Magneto-Electrical Effect in Antiferromagnets*, *J. Exp. Theor. Phys.* **10** (1960) 628.

[69] K. Siratori, K. Kohn and E. Kita, *Magnetoelectric Effect in Magnetic Materials*, *Acta Phys. Polon. A* **81** (1992) 431.

[70] J.P. Rivera, *A short review of the magnetoelectric effect and related experimental techniques on single phase (multi-) ferroics*, *Eur. Phys. J. B* **71** (2009) 299.

[71] C. Bradley and A. Cracknell, *The Mathematical Theory of Symmetry in Solids*, Oxford University Press, (2010).

[72] V.J. Folen, G.T. Rado and E.W. Stalder, *Anisotropy of the Magnetoelectric Effect in Cr_2O_3*, *Phys. Rev. Lett.* **6** (1961) 607.

[73] L. Wu, M. Salehi, N. Koirala, J. Moon, S. Oh and N.P. Armitage, *Quantized Faraday and Kerr rotation and axion electrodynamics of the surface states of three-dimensional topological insulators*, *Science* **354** (2016) 1124 [arXiv:1603.04317] [INSPIRE].

[74] N.P. Armitage and L. Wu, *On the matter of topological insulators as magnetoelectrics*, *SciPost Phys.* **6** (2019) 046 [arXiv:1810.01233] [INSPIRE].

[75] R.S.K. Mong, A.M. Essin and J.E. Moore, *Antiferromagnetic topological insulators*, *Phys. Rev. B* **81** (2010) 245209 [arXiv:1004.1403].

[76] M.M. Otrokov et al., *Prediction and observation of an antiferromagnetic topological insulator*, *Nature* **576** (2019) 416 [arXiv:1809.07389] [INSPIRE].

[77] J. Li et al., *Intrinsic magnetic topological insulators in van der Waals layered $MnBi_2Te_4$ -family materials*, *Sci. Adv.* **5** (2019) eaaw5685 [arXiv:1808.08608].

[78] C. Liu et al., *Robust axion insulator and Chern insulator phases in a two-dimensional antiferromagnetic topological insulator*, *Nature Mater.* **19** (2020) 522.

JCAP08(2021)066

[79] C.L. Kane and E.J. Mele, *Z-2 Topological Order and the Quantum Spin Hall Effect*, *Phys. Rev. Lett.* **95** (2005) 146802 [cond-mat/0506581] [INSPIRE].

[80] J. Wang, B. Lian and S.-C. Zhang, *Dynamical axion field in a magnetic topological insulator superlattice*, *Phys. Rev. B* **93** (2016) 45115.

[81] C. Herring, *Magnetism: Exchange interactions among itinerant electrons*, *Magnetism* (1966) 407.

[82] R. Ramazashvili, *Kramers Degeneracy in a Magnetic Field and Zeeman Spin-Orbit Coupling in Antiferromagnetic Conductors*, *Phys. Rev. Lett.* **101** (2008) 137202.

[83] C. Fang, M.J. Gilbert and B.A. Bernevig, *Topological insulators with commensurate antiferromagnetism*, *Phys. Rev. B* **88** (2013) 085406 [arXiv:1304.6081] [INSPIRE].

[84] L. Šmejkal, Y. Mokrousov, B. Yan and A.H. MacDonald, *Topological antiferromagnetic spintronics*, *Nature Phys.* **14** (2018) 242 [arXiv:1706.00670] [INSPIRE].

[85] D.J.E. Marsh and J.C. Niemeyer, *Strong Constraints on Fuzzy Dark Matter from Ultrafaint Dwarf Galaxy Eridanus II*, *Phys. Rev. Lett.* **123** (2019) 051103 [arXiv:1810.08543] [INSPIRE].

[86] A. Malashevich, S. Coh, I. Souza and D. Vanderbilt, *Full magnetoelectric response of Cr 2 O 3 from first principles*, *Phys. Rev. B* **86** (2012) 94430.

[87] S. Coh, D. Vanderbilt, A. Malashevich and I. Souza, *Chern-Simons orbital magnetoelectric coupling in generic insulators*, *Phys. Rev. B* **83** (2011) 85108.

[88] A.I. Milstein and O.P. Sushkov, *Effective field theories and spin-wave excitations in helical magnets*, *Phys. Rev. B* **84** (2011) 195138.

[89] M. Dzero, K. Sun, V. Galitski and P. Coleman, *Topological Kondo Insulators*, *Phys. Rev. Lett.* **104** (2010) 106408 [arXiv:0912.3750] [INSPIRE].

[90] X. Wan, A.M. Turner, A. Vishwanath and S.Y. Savrasov, *Topological semimetal and Fermi-arc surface states in the electronic structure of pyrochlore iridates*, *Phys. Rev. B* **83** (2011) 205101 [arXiv:1007.0016] [INSPIRE].

[91] J. Wang, R. Li, S.-C. Zhang and X.-L. Qi, *Topological Magnetic Insulators with Corundum Structure*, *Phys. Rev. Lett.* **106** (2011) 126403.

[92] Y. Li, Y. Jiang, J. Zhang, Z. Liu, Z. Yang and J. Wang, *Intrinsic topological phases in Mn2Bi2Te5 tuned by the layer magnetization*, *Phys. Rev. B* **102** (2020) 121107 [arXiv:2001.06133] [INSPIRE].

[93] J. Kim and S.-H. Jhi, *Magnetic phase transition in fe-doped topological insulator* Bi_2Se_3, *Phys. Rev. B* **92** (2015) 104405.

[94] H. Zhang, C.-X. Liu, X.-L. Qi, X. Dai, Z. Fang and S.-C. Zhang, *Topological insulators in* Bi_2Se_3, Bi_2Te_3 *and* Sb_2Te_3 *with a single Dirac cone on the surface* *Nature Phys.* **5** (2009) 438 [arXiv:1405.2036].

[95] C.X. Liu, X.L. Qi, H. Zhang, X. Dai, Z. Fang and S.C. Zhang, *Model Hamiltonian for topological insulators*, *Phys. Rev. B* **82** (2010) 045122 [arXiv:1005.1682].

[96] F.D.M. Haldane, *Nonlinear field theory of large spin Heisenberg antiferromagnets. Semiclassically quantized solitons of the one-dimensional easy Axis Néel state*, *Phys. Rev. Lett.* **50** (1983) 1153 [INSPIRE].

[97] N. Nagaosa and M. Oshikawa, *Chiral anomaly and spin gap in one-dimensional interacting fermions*, *J. Phys. Soc. Jap.* **65** (1996) 2241.

[98] P. Hosur, S. Ryu and A. Vishwanath, *Chiral topological insulators, superconductors, and other competing orders in three dimensions*, *Phys. Rev. B* **81** (2010) 045120.

JCAP08(2021)066

[99] A. Sekine and K. Nomura, *Chiral Magnetic Effect and Anomalous Hall Effect in Antiferromagnetic Insulators with Spin-Orbit Coupling*, *Phys. Rev. Lett.* **116** (2016) 096401 [arXiv:1508.04590] [INSPIRE].

[100] Y. Xian and M. Merdan, *Longitudinal Excitations in Bipartite and Hexagonal Antiferromagnetic Spin Lattices*, *J. Phys. Conf. Ser.* **529** (2014) 012020 [arXiv:1312.4929] [INSPIRE].

[101] D. Bossini et al., *Laser-driven quantum magnonics and terahertz dynamics of the order parameter in antiferromagnets*, *Phys. Rev. B* **100** (2019) 024428.

[102] J.-M. Zhang et al., *Stability, electronic, and magnetic properties of the magnetically doped topological insulators Bi_2Se_3, Bi_2Te_3, and Sb_2Te_3*, *Phys. Rev. B* **88** (2013) 235131.

[103] Y. Sharma and P. Srivastava, *First Principles Study of Electronic and Optical Properties of Bi2Se3 in its Trigonal and Orthorhombic Phases*, *AIP Conf. Proc.* **1249** (2010) 183.

[104] T. Cao and S. Wang, *Topological insulator metamaterials with tunable negative refractive index in the optical region*, *Nanoscale Res. Lett.* **8** (2013) 526.

[105] J.-M. Zhang, W. Zhu, Y. Zhang, D. Xiao and Y. Yao, *Tailoring Magnetic Doping in the Topological Insulator Bi_2Se_3*, *Phys. Rev. Lett.* **109** (2012) 266405 [arXiv:1205.3936].

[106] A.I. Liechtenstein, M.I. Katsnelson, V.P. Antropov and V.A. Gubanov, *Local spin density functional approach to the theory of exchange interactions in ferromagnetic metals and alloys*, *Journal of Magnetism and Magnetic Materials* **67** (1987) 65.

[107] P. Fazekas, *Lecture Notes on Electron Correlation and Magnetism*, World Scientific, (1999), [DOI].

[108] S.M. Rezende, A. Azevedo and R.L. Rodríguez-Suárez, *Introduction to antiferromagnetic magnons*, *J. Appl. Phys.* **126** (2019) 151101.

[109] M. Gell-Mann, R.J. Oakes and B. Renner, *Behavior of current divergences under* SU(3) × SU(3), *Phys. Rev.* **175** (1968) 2195 [INSPIRE].

[110] A.N. Bogdanov, U.K. Rößler, M. Wolf and K.-H. Müller, *Magnetic structures and reorientation transitions in noncentrosymmetric uniaxial antiferromagnets*, *Phys. Rev. B* **66** (2002) 214410.

[111] Y.-J. Hao et al., *Gapless Surface Dirac Cone in Antiferromagnetic Topological Insulator* $MnBi_2Te_4$, *Phys. Rev. X* **9** (2019) 041038.

[112] Z. Ren, A.A. Taskin, S. Sasaki, K. Segawa and Y. Ando, *Observations of two-dimensional quantum oscillations and ambipolar transport in the topological insulator Bi_2Se_3 achieved by Cd doping*, *Phys. Rev. B* **84** (2011) 075316 [arXiv:1107.4178].

[113] J.-Q. Yan et al., *Crystal growth and magnetic structure of $MnBi_2Te_4$*, *Phys. Rev. Mater.* **3** (2019) 064202.

[114] X.-M. Ma et al., *Spectroscopic realization of large surface gap in a doped magnetic topological insulator*, arXiv:2004.09123.

[115] V.S. L'vov, *Wave Turbulence Under Parametric Excitation — Applications to Magnetics*, Springer (1994).

[116] A.B. Harris, D. Kumar, B.I. Halperin and P.C. Hohenberg, *Dynamics of an Antiferromagnet at Low Temperatures: Spin-Wave Damping and Hydrodynamics*, *Phys. Rev. B* **3** (1971) 961 [INSPIRE].

[117] S. Bayrakci, T. Keller, K. Habicht and B. Keimer, *Spin-Wave Lifetimes Throughout the Brillouin Zone*, *Science* **312** (2006) 1926 [cond-mat/0606814].

[118] S.P. Bayrakci et al., *Lifetimes of antiferromagnetic magnons in two and three dimensions: Experiment, theory, and numerics*, *Phys. Rev. Lett.* **111** (2013) 017204.

JCAP08(2021)066

[119] M.C. Hickey and J.S. Moodera, *Origin of intrinsic gilbert damping*, *Phys. Rev. Lett.* **102** (2009) 137601.

[120] R.A. Duine, A.S. Núñez, J. Sinova and A.H. MacDonald, *Functional keldysh theory of spin torques*, *Phys. Rev. B* **75** (2007) 214420.

[121] I. Garate and A. MacDonald, *Gilbert damping in conducting ferromagnets. II. Model tests of the torque-correlation formula*, *Phys. Rev. B* **79** (2009) 064404.

[122] C.P. Hofmann, *Spin wave scattering in the effective Lagrangian perspective*, *Phys. Rev. B* **60** (1999) 388 [cond-mat/9805277] [INSPIRE].

[123] S. Dodelson, *Modern cosmology*, Academic Press, (2003).

[124] M.E. Peskin and D.V. Schroeder, *An Introduction to Quantum Field Theory*, Westview Press, 1995.

[125] D.L. Mills and E. Burstein, *Polaritons: the electromagnetic modes of media*, *Rept. Prog. Phys.* **37** (1974) 817.

[126] J. Schütte-Engel, *Axion direct detection in particle and condensed matter physics*, Ph.D. Thesis, Hamburg University, Hamburg, Germany (2020), [INSPIRE].

[127] C.M. Caves, *Quantum limits on noise in linear amplifiers*, *Phys. Rev. D* **26** (1982) 1817 [INSPIRE].

[128] J.C. Mather, *Bolometers: ultimate sensitivity, optimization, and amplifier coupling*, *Appl. Opt.* **23** (1984) 584.

[129] J.R. Tucker and M.J. Feldman, *Quantum detection at millimeter wavelengths*, *Rev. Mod. Phys.* **57** (1985) 1055 [INSPIRE].

[130] A.A. Clerk, M.H. Devoret, S.M. Girvin, F. Marquardt and R.J. Schoelkopf, *Introduction to quantum noise, measurement, and amplification*, *Rev. Mod. Phys.* **82** (2010) 1155 [arXiv:0810.4729] [INSPIRE].

[131] D. McCammon, *Thermal Equilibrium Calorimeters — An Introduction*, in *Cryogenic Particle Detection*, C. Enss, ed., vol. 99, p. 1. Springer Berlin Heidelberg, (2005). [DOI].

[132] E.D. Walsh et al., *Graphene-Based Josephson-Junction Single-Photon Detector*, *Phys. Rev. Applied* **8** (2017) 024022 [arXiv:1703.09736].

[133] B. Yurke et al., *Observation of parametric amplification and deamplification in a Josephson parametric amplifier*, *Phys. Rev. A* **39** (1989) 2519.

[134] B.M. Brubaker et al., *First results from a microwave cavity axion search at 24 μeV*, *Phys. Rev. Lett.* **118** (2017) 061302 [arXiv:1610.02580] [INSPIRE].

[135] J. Aumentado, *Superconducting Parametric Amplifiers: The State of the Art in Josephson Parametric Amplifiers*, *IEEE Microwave* **21** (2020) 45.

[136] W.R. McGrath, P.L. Richards, D.W. Face, D.E. Prober and F.L. Lloyd, *Accurate experimental and theoretical comparisons between superconductor-insulator-superconductor mixers showing weak and strong quantum effects*, *J. Appl. Phys.* **63** (1998) 2479.

[137] W. Zhang et al., *Quantum noise in a terahertz hot electron bolometer mixer*, *Appl. Phys. Lett.* **96** (2010) 111113.

[138] S. Lara-Avila et al., *Towards quantum-limited coherent detection of terahertz waves in charge-neutral graphene*, *Nature Astron.* **3** (2019) 983 [arXiv:1904.03247].

[139] N. Wang, S. Cakmakyapan, Y.-J. Lin, H. Javadi and M. Jarrahi, *Room Temperature Terahertz Spectrometer with Quantum-Level Sensitivity*, arXiv:1806.05256 [INSPIRE].

JCAP08(2021)066

[140] J. Wei, D. Olaya, B. Karasik, S. Pereverzev, A. Sergeev and M. Gershenson, *Ultra-Sensitive Hot-Electron Nanobolometers for Terahertz Astrophysics*, *Nature Nanotech.* **3** (2008) 496 [arXiv:0710.5474] [INSPIRE].

[141] P. Day, H. LeDuc, B. Mazin, A. Vayonakis and J. Zmuidzinas, *A broadband superconducting detector suitable for use in large arrays*, *Nature* **425** (2003) 817.

[142] G.N. Gol'tsman et al., *Picosecond superconducting single-photon optical detector*, *Appl. Phys. Lett.* **79** (2001) 705.

[143] Y. Hochberg, I. Charaev, S.-W. Nam, V. Verma, M. Colangelo and K.K. Berggren, *Detecting Sub-GeV Dark Matter with Superconducting Nanowires*, *Phys. Rev. Lett.* **123** (2019) 151802 [arXiv:1903.05101] [INSPIRE].

[144] G.C. Irwin, K.D. and Hilton, *Transition-edge sensors*, in *Cryogenic Particle Detection*, pp. 63–150. Springer Berlin Heidelberg, (2005). [DOI].

[145] B.S. Karasik et al., *Energy-resolved detection of single infrared photons with $\lambda = 8\,\mu m$ using a superconducting microbolometer*, *Appl. Phys. Lett.* **101** (2012) 052601 [arXiv:1207.2164] [INSPIRE].

[146] E.D. Walsh et al., *Josephson-junction infrared single-photon detector*, arXiv:2011.02624.

[147] A. Peacock et al., *Single optical photon detection with a superconducting tunnel junction*, *Nature* **381** (1996) 135.

[148] P.M. Echternach, B.J. Pepper, T. Reck and C.M. Bradford, *Single photon detection of 1.5 THz radiation with the quantum capacitance detector*, *Nature Astron.* **2** (2018) 90.

[149] H. Vora, P. Kumaravadivel, B. Nielsen and X. Du, *Bolometric response in graphene based superconducting tunnel junctions*, *Appl. Phys. Lett.* **100** (2012) 153507 [arXiv:1110.5623].

[150] K.C. Fong and K. Schwab, *Ultrasensitive and wide-bandwidth thermal measurements of graphene at low temperatures*, *Phys. Rev. X* **2** (2012) 031006 [arXiv:1202.5737].

[151] C. McKitterick, D. Prober and B. Karasik, *Performance of graphene thermal photon detectors*, *J. Appl. Phys.* **113** (2013) 044512 [arXiv:1210.5495].

[152] S.H. Moseley, J.C. Mather and D. McCammon, *Thermal detectors as x-ray spectrometers*, *J. Appl. Phys.* **56** (1984) 1257.

[153] L. Vicarelli et al., *Graphene field-effect transistors as room-temperature terahertz detectors*, *Nature Mater.* **11** (2012) 865 [arXiv:1203.3232].

[154] D.A. Bandurin et al., *Resonant terahertz detection using graphene plasmons*, *Nature Commun.* **9** (2018) 1 [arXiv:1807.04703].

[155] R. Kokkoniemi et al., *Bolometer operating at the threshold for circuit quantum electrodynamics*, *Nature* **586** (2020) 47 [arXiv:2008.04628] [INSPIRE].

[156] A.V. Dixit et al., *Searching for Dark Matter with a Superconducting Qubit*, *Phys. Rev. Lett.* **126** (2021) 141302 [arXiv:2008.12231] [INSPIRE].

[157] S. Komiyama, O. Astafiev, V. Antonov, T. Kutsuwa and H. Hirai, *A single-photon detector in the far-infrared range*, *Nature* **403** (2000) 405.

[158] B. Johnson et al., *Quantum non-demolition detection of single microwave photons in a circuit*, *Nature Phys.* **6** (2010) 663 [arXiv:1003.2734].

[159] S. Kono, K. Koshino, Y. Tabuchi, A. Noguchi and Y. Nakamura, *Quantum non-demolition detection of an itinerant microwave photon*, *Nature Phys.* **14** (2018) 546 [arXiv:1711.05479].

[160] S.K. Lamoreaux, K.A. van Bibber, K.W. Lehnert and G. Carosi, *Analysis of single-photon and linear amplifier detectors for microwave cavity dark matter axion searches*, *Phys. Rev. D* **88** (2013) 035020 [arXiv:1306.3591] [INSPIRE].

JCAP08(2021)066

[161] S. Komiyama, *Single-Photon Detectors in the Terahertz Range*, *IEEE J. Select. Topics Quantum Electron.* **17** (2011) 54.

[162] D.M. Mittleman, *Perspective: Terahertz science and technology*, *J. Appl. Phys.* **122** (2017) 230901.

[163] R.A. Lewis, *A review of terahertz detectors*, *J. Phys. D* **52** (2019) 433001.

[164] S.I. Bityukov and N.V. Krasnikov, *New physics discovery potential in future experiments*, *Mod. Phys. Lett. A* **13** (1998) 3235 [physics/9811025] [INSPIRE].

[165] S.I. Bityukov and N.V. Krasnikov, *On the observability of a signal above background*, *Nucl. Instrum. Meth. A* **452** (2000) 518 [INSPIRE].

[166] P. Arias, J. Jaeckel, J. Redondo and A. Ringwald, *Optimizing Light-Shining-through-a-Wall Experiments for Axion and other WISP Searches*, *Phys. Rev. D* **82** (2010) 115018 [arXiv:1009.4875] [INSPIRE].

[167] S. Knirck et al., *A First Look on 3D Effects in Open Axion Haloscopes*, *JCAP* **08** (2019) 026 [arXiv:1906.02677] [INSPIRE].

[168] S. Beurthey et al., *MADMAX Status Report*, arXiv:2003.10894 [INSPIRE].

[169] C. O'Hare, *cajohare/axionlimits: Axionlimits*, (2020), [DOI].

[170] CAST collaboration, *An improved limit on the axion-photon coupling from the CAST experiment*, *JCAP* **04** (2007) 010 [hep-ex/0702006] [INSPIRE].

[171] CAST collaboration, *New CAST Limit on the Axion-Photon Interaction*, *Nature Phys.* **13** (2017) 584 [arXiv:1705.02290] [INSPIRE].

[172] IAXO collaboration, *Physics potential of the International Axion Observatory (IAXO)*, *JCAP* **06** (2019) 047 [arXiv:1904.09155] [INSPIRE].

[173] S. De Panfilis et al., *Limits on the abundance and coupling of cosmic axions at 4.5< m_a <5.0 μeV*, *Phys. Rev. Lett.* **59** (1987) 839 [INSPIRE].

[174] ADMX collaboration, *A SQUID-based microwave cavity search for dark-matter axions*, *Phys. Rev. Lett.* **104** (2010) 041301 [arXiv:0910.5914] [INSPIRE].

[175] B.T. McAllister, G. Flower, E.N. Ivanov, M. Goryachev, J. Bourhill and M.E. Tobar, *The ORGAN Experiment: An axion haloscope above 15 GHz*, *Phys. Dark Univ.* **18** (2017) 67 [arXiv:1706.00209] [INSPIRE].

[176] HAYSTAC collaboration, *Results from phase 1 of the HAYSTAC microwave cavity axion experiment*, *Phys. Rev. D* **97** (2018) 092001 [arXiv:1803.03690] [INSPIRE].

[177] ADMX collaboration, *A Search for Invisible Axion Dark Matter with the Axion Dark Matter Experiment*, *Phys. Rev. Lett.* **120** (2018) 151301 [arXiv:1804.05750] [INSPIRE].

[178] D. Alesini et al., *Galactic axions search with a superconducting resonant cavity*, *Phys. Rev. D* **99** (2019) 101101 [arXiv:1903.06547] [INSPIRE].

[179] M. Lawson, A.J. Millar, M. Pancaldi, E. Vitagliano and F. Wilczek, *Tunable axion plasma haloscopes*, *Phys. Rev. Lett.* **123** (2019) 141802 [arXiv:1904.11872] [INSPIRE].

[180] S. Lee, S. Ahn, J. Choi, B.R. Ko and Y.K. Semertzidis, *Axion Dark Matter Search around 6.7 μeV*, *Phys. Rev. Lett.* **124** (2020) 101802 [arXiv:2001.05102] [INSPIRE].

[181] W. Giarè, E. Di Valentino, A. Melchiorri and O. Mena, *New cosmological bounds on hot relics: axions and neutrinos*, *Mon. Not. Roy. Astron. Soc.* **505** (2021) 2703 [arXiv:2011.14704] [INSPIRE].

[182] PLANCK collaboration, *Planck 2018 results. VI. Cosmological parameters*, *Astron. Astrophys.* **641** (2020) A6 [*Erratum ibid.* **652** (2021) C4] [arXiv:1807.06209] [INSPIRE].

JCAP08(2021)066

[183] M. Gorghetto, E. Hardy and G. Villadoro, *More Axions from Strings*, *SciPost Phys.* **10** (2021) 050 [arXiv:2007.04990] [INSPIRE].

[184] F. Keffer and C. Kittel, *Theory of antiferromagnetic resonance*, *Phys. Rev.* **85** (1952) 329.

[185] F. Keffer, H. Kaplan and Y. Yafet, *Spin waves in ferromagnetic and antiferromagnetic materials*, *Am. J. Phys.* **21** (1953) 250.

[186] A.I. Kakhidze and I.V. Kolokolov, *Antiferromagnetic axions detector*, *Sov. Phys. JETP* **72** (1991) 598 [INSPIRE].

[187] A. Garcon et al., *Constraints on bosonic dark matter from ultralow-field nuclear magnetic resonance*, *Sci. Adv.* **5** (2019) eaax4539 [arXiv:1902.04644] [INSPIRE].

[188] N. Crescini et al., *Operation of a ferromagnetic axion haloscope at $m_a = 58\,\mu eV$*, *Eur. Phys. J. C* **78** (2018) 703 [*Erratum ibid.* **78** (2018) 813] [arXiv:1806.00310] [INSPIRE].

[189] MADMAX collaboration, *A new experimental approach to probe QCD axion dark matter in the mass range above 40 μeV*, *Eur. Phys. J. C* **79** (2019) 186 [arXiv:1901.07401] [INSPIRE].

[190] M. Baryakhtar, J. Huang and R. Lasenby, *Axion and hidden photon dark matter detection with multilayer optical haloscopes*, *Phys. Rev. D* **98** (2018) 035006 [arXiv:1803.11455] [INSPIRE].

[191] M. Goryachev, B.T. Mcallister and M.E. Tobar, *Axion detection with negatively coupled cavity arrays*, *Phys. Lett. A* **382** (2018) 2199 [arXiv:1703.07207] [INSPIRE].

[192] J. Jeong, S. Ahn, S. Youn, J.E. Kim and Y.K. Semertzidis, *New design of multiple-cavity detector for high mass axion dark matter search*, *PoS* **ICHEP2018** (2019) 833 [INSPIRE].

[193] A.A. Melcón et al., *Axion Searches with Microwave Filters: the RADES project*, *JCAP* **05** (2018) 040 [arXiv:1803.01243] [INSPIRE].

[194] D.E. Morris, *Electromagnetic detector for relic axions*, Technical Report, Lawrence Berkeley Lab., CA, U.S.A. (1984), [DOI].

[195] A.P. Quiskamp, B.T. McAllister, G. Rybka and M.E. Tobar, *Dielectric-Boosted Sensitivity to Cylindrical Azimuthally Varying Transverse-Magnetic Resonant Modes in an Axion Haloscope*, *Phys. Rev. Applied* **14** (2020) 044051 [arXiv:2006.05641] [INSPIRE].

[196] G. Carosi, R. Cervantes, S. Kimes, P. Mohapatra, R. Ottens and G. Rybka, *Orpheus: Extending the ADMX QCD Dark-Matter Axion Search to Higher Masses*, *Springer Proc. Phys.* **245** (2020) 169 [INSPIRE].

[197] http://www.iexp.uni-hamburg.de/groups/astroparticle/brass/brassweb.htm.

[198] A. Mitridate, T. Trickle, Z. Zhang and K.M. Zurek, *Detectability of Axion Dark Matter with Phonon Polaritons and Magnons*, *Phys. Rev. D* **102** (2020) 095005 [arXiv:2005.10256] [INSPIRE].

[199] C.P. Burgess, *Goldstone and pseudoGoldstone bosons in nuclear, particle and condensed matter physics*, *Phys. Rept.* **330** (2000) 193 [hep-th/9808176] [INSPIRE].

[200] D. Wagner, *Introduction to the Theory of Magnetism*, Pergamon, (1972).

[201] O. Bär, M. Imboden and U.J. Wiese, *Pions versus magnons: from QCD to antiferromagnets and quantum Hall ferromagnets*, *Nucl. Phys. B* **686** (2004) 347 [cond-mat/0310353] [INSPIRE].

[202] M. Imboden, *Pions versus Magnons: From QCD to Antiferromagnets and Quantum Hall Ferromagnets*, MSc Thesis, Universität Bern, (2003).

[203] A. Sekine and T. Chiba, *Electric-Field-Induced Spin Resonance in Antiferromagnetic Insulators: Inverse Process of the Dynamical Chiral Magnetic Effect*, *Phys. Rev. B* **93** (2016) 220403 [arXiv:1603.00614] [INSPIRE].

JCAP08(2021)066

[204] A. Sekine and T. Chiba, *Electric-field-induced antiferromagnetic resonance in antiferromagnetic insulators with spin-orbit coupling*, *AIP Adv.* **7** (2017) 055902.

[205] E.M. Lifshitz and L.P. Pitaevskii, *Statistical Physics, Course of Theoretical Physics*. Pergamon, Oxford, U.K. (1980).

[206] K.M.D. Hals, Y. Tserkovnyak and A. Brataas, *Phenomenology of current-induced dynamics in antiferromagnets*, *Phys. Rev. Lett.* **106** (2011) 107206.

[207] R.D. Peccei and H.R. Quinn, *Constraints Imposed by CP Conservation in the Presence of Instantons*, *Phys. Rev. D* **16** (1977) 1791 [INSPIRE].

[208] M.S. Turner, *Cosmic and Local Mass Density of Invisible Axions*, *Phys. Rev. D* **33** (1986) 889 [INSPIRE].

[209] P. Sikivie, *Detection Rates for 'Invisible' Axion Searches*, *Phys. Rev. D* **32** (1985) 2988 [*Erratum ibid.* **36** (1987) 974] [INSPIRE].

[210] K. van Bibber, P.M. McIntyre, D.E. Morris and G.G. Raffelt, *A Practical Laboratory Detector for Solar Axions*, *Phys. Rev. D* **39** (1989) 2089 [INSPIRE].

[211] J. Jaeckel and A. Ringwald, *The Low-Energy Frontier of Particle Physics*, *Ann. Rev. Nucl. Part. Sci.* **60** (2010) 405 [arXiv:1002.0329] [INSPIRE].

[212] N. Arkani-Hamed, L. Motl, A. Nicolis and C. Vafa, *The String landscape, black holes and gravity as the weakest force*, *JHEP* **06** (2007) 060 [hep-th/0601001] [INSPIRE].

[213] HotQCD collaboration, *Chiral crossover in QCD at zero and non-zero chemical potentials*, *Phys. Lett. B* **795** (2019) 15 [arXiv:1812.08235] [INSPIRE].

[214] S. Borsányi et al., *QCD Crossover at Finite Chemical Potential from Lattice Simulations*, *Phys. Rev. Lett.* **125** (2020) 052001 [arXiv:2002.02821] [INSPIRE].

[215] M. Gorghetto and G. Villadoro, *Topological Susceptibility and QCD Axion Mass: QED and NNLO corrections*, *JHEP* **03** (2019) 033 [arXiv:1812.01008] [INSPIRE].

[216] G. Grilli di Cortona, E. Hardy, J. Pardo Vega and G. Villadoro, *The QCD axion, precisely*, *JHEP* **01** (2016) 034 [arXiv:1511.02867] [INSPIRE].

[217] S. Borsányi et al., *Calculation of the axion mass based on high-temperature lattice quantum chromodynamics*, *Nature* **539** (2016) 69 [arXiv:1606.07494] [INSPIRE].

[218] D.J. Gross, R.D. Pisarski and L.G. Yaffe, *QCD and Instantons at Finite Temperature*, *Rev. Mod. Phys.* **53** (1981) 43 [INSPIRE].

[219] O. Wantz and E.P.S. Shellard, *Axion Cosmology Revisited*, *Phys. Rev. D* **82** (2010) 123508 [arXiv:0910.1066] [INSPIRE].

[220] M.J. Stott, *Ultralight Bosonic Field Mass Bounds from Astrophysical Black Hole Spin*, arXiv:2009.07206 [INSPIRE].

[221] A. Ayala, I. Domínguez, M. Giannotti, A. Mirizzi and O. Straniero, *Revisiting the bound on axion-photon coupling from Globular Clusters*, *Phys. Rev. Lett.* **113** (2014) 191302 [arXiv:1406.6053] [INSPIRE].

[222] M. Giannotti, I. Irastorza, J. Redondo and A. Ringwald, *Cool WISPs for stellar cooling excesses*, *JCAP* **05** (2016) 057 [arXiv:1512.08108] [INSPIRE].

[223] T.W.B. Kibble, *Topology of Cosmic Domains and Strings*, *J. Phys. A* **9** (1976) 1387 [INSPIRE].

[224] T.W.B. Kibble, *Some Implications of a Cosmological Phase Transition*, *Phys. Rept.* **67** (1980) 183 [INSPIRE].

[225] A. Vilenkin, *Cosmic Strings*, *Phys. Rev. D* **24** (1981) 2082 [INSPIRE].

JCAP08(2021)066

[226] T. Hiramatsu, M. Kawasaki, K. Saikawa and T. Sekiguchi, *Axion cosmology with long-lived domain walls*, *JCAP* **01** (2013) 001 [arXiv:1207.3166] [INSPIRE].

[227] V.B.. Klaer and G.D. Moore, *The dark-matter axion mass*, *JCAP* **11** (2017) 049 [arXiv:1708.07521] [INSPIRE].

[228] M. Buschmann, J.W. Foster and B.R. Safdi, *Early-Universe Simulations of the Cosmological Axion*, *Phys. Rev. Lett.* **124** (2020) 161103 [arXiv:1906.00967] [INSPIRE].

[229] A. Caputo and M. Reig, *Cosmic implications of a low-scale solution to the axion domain wall problem*, *Phys. Rev. D* **100** (2019) 063530 [arXiv:1905.13116] [INSPIRE].

[230] A. Ringwald and K. Saikawa, *Axion dark matter in the post-inflationary Peccei-Quinn symmetry breaking scenario*, *Phys. Rev. D* **93** (2016) 085031 [*Addendum ibid.* **94** (2016) 049908] [arXiv:1512.06436] [INSPIRE].

[231] C.J. Hogan and M.J. Rees, *Axion miniclusters*, *Phys. Lett. B* **205** (1988) 228 [INSPIRE].

[232] E.W. Kolb and I.I. Tkachev, *Axion miniclusters and Bose stars*, *Phys. Rev. Lett.* **71** (1993) 3051 [hep-ph/9303313] [INSPIRE].

[233] E.W. Kolb and I.I. Tkachev, *Large amplitude isothermal fluctuations and high density dark matter clumps*, *Phys. Rev. D* **50** (1994) 769 [astro-ph/9403011] [INSPIRE].

[234] V.I. Dokuchaev, Y.N. Eroshenko and I.I. Tkachev, *Destruction of axion miniclusters in the Galaxy*, *J. Exp. Theor. Phys.* **125** (2017) 434 [arXiv:1710.09586] [INSPIRE].

[235] A. Vaquero, J. Redondo and J. Stadler, *Early seeds of axion miniclusters*, *JCAP* **04** (2019) 012 [arXiv:1809.09241] [INSPIRE].

[236] B. Eggemeier, J. Redondo, K. Dolag, J.C. Niemeyer and A. Vaquero, *First Simulations of Axion Minicluster Halos*, *Phys. Rev. Lett.* **125** (2020) 041301 [arXiv:1911.09417] [INSPIRE].

[237] B.J. Kavanagh, T.D.P. Edwards, L. Visinelli and C. Weniger, *Stellar Disruption of Axion Miniclusters in the Milky Way*, arXiv:2011.05377 [INSPIRE].

[238] A.H. Guth, *The Inflationary Universe: A Possible Solution to the Horizon and Flatness Problems*, *Phys. Rev. D* **23** (1981) 347 [INSPIRE].

[239] A.D. Linde, *A New Inflationary Universe Scenario: A Possible Solution of the Horizon, Flatness, Homogeneity, Isotropy and Primordial Monopole Problems*, *Phys. Lett. B* **108** (1982) 389 [INSPIRE].

[240] A. Albrecht and P.J. Steinhardt, *Cosmology for Grand Unified Theories with Radiatively Induced Symmetry Breaking*, *Phys. Rev. Lett.* **48** (1982) 1220 [INSPIRE].

[241] M.P. Hertzberg, M. Tegmark and F. Wilczek, *Axion Cosmology and the Energy Scale of Inflation*, *Phys. Rev. D* **78** (2008) 083507 [arXiv:0807.1726] [INSPIRE].

[242] S. Hoof, F. Kahlhoefer, P. Scott, C. Weniger and M. White, *Axion global fits with Peccei-Quinn symmetry breaking before inflation using GAMBIT*, *JHEP* **03** (2019) 191 [*Erratum ibid.* **11** (2019) 099] [arXiv:1810.07192] [INSPIRE].

[243] F. Wilczek, *A model of anthropic reasoning, addressing the dark to ordinary matter coincidence*, hep-ph/0408167 [INSPIRE].

[244] M. Tegmark, A. Aguirre, M. Rees and F. Wilczek, *Dimensionless constants, cosmology and other dark matters*, *Phys. Rev. D* **73** (2006) 023505 [astro-ph/0511774] [INSPIRE].

JCAP08(2021)066